Electronic Supplementary Information for:

High temperature magnetic blocking and magneto-structural correlations in a series of dysprosium(III) metallocenium single-molecule magnets

Kenneth R. McClain,[a‡] Colin A. Gould,[b‡] Khetpakorn Chakarawet,[b] Simon J. Teat,[c] Thomas Groshens,[a] Jeffrey R. Long,[bde*] and Benjamin G. Harvey[a*]

[a]US Navy, Naval Air Warfare Center, Weapons Division , Research Department, Chemistry Division, China Lake, California, 93555, United States

[b]Department of Chemistry, University of California, Berkeley, Berkeley, California 94720, United States

[c]Advanced Light Source, Lawrence Berkeley National Laboratory, Berkeley, California, 94720, United States

[d]Materials Sciences Division, Lawrence Berkeley National Laboratory, Berkeley, California 94720, United States

[e]Department of Chemical and Biomolecular Engineering, University of California, Berkeley, Berkeley, California 94720, United States

Table of Contents

Synthesis of $[\mathrm{Y(Cp}^{i\mathrm{Pr4Et}})_2][\mathrm{B(C_6F_5)_4}]$ (Y3). Under argon, $\mathrm{YI_3}$ (0.19 g / 0.40 mmol) and $\mathrm{NaCp}^{i\mathrm{Pr4Et}}$ (0.29 g / 1.0 mmol) were combined in a 35 mL pressure flask containing a glass-coated magnetic stirring bar and toluene (15 mL) was added. The reaction flask was covered in Al foil, and heated gradually to 160 °C with vigorous stirring. After 72 h at 160 °C, the flask was allowed to cool to room temperature, the reaction mixture was filtered through Celite and the pad washed with additional toluene (3 X 5 mL). Solvent was removed from the filtrate under vacuum and the residue was gently heated (50 °C) under vacuum for 1 h. The residue was taken up in pentane (25 mL), stirred for 0.5 h, filtered through Celite and the pad washed with additional pentane (3 X 5 mL). Solvent was removed from the filtrate under vacuum and the residue was gently heated (50 °C) under vacuum for 0.5 h to give crude $\mathrm{Y(Cp}^{i\mathrm{Pr4Et}})_2\mathrm{I}$. This was dissolved with benzene (10 mL) in a 25 mL Schlenk flask equipped with a Teflon magnetic stirring bar. Under vigorous stirring at room temperature, a solution of $[\mathrm{H(SiEt_3)_2}][\mathrm{B(C_6F_5)_4}]$ (0.29 g / 0.32 mmol) in benzene (5 mL) was added dropwise to the $\mathrm{Y(Cp}^{i\mathrm{Pr4Et}})_2\mathrm{I}$ solution over 5 min. After stirring for 72 h at room temperature, solvent was removed from the reaction mixture under vacuum, the residue was slurried with pentane (20 mL) for 0.5 h and isolated as a powder on a medium-porosity fritted filter after washing with pentane (3 X 10 mL). This was dried under vacuum, dissolved in dichloromethane (4 mL), filtered with aid of Celite through a 0.2 µm porosity PTFE syringe filter and layered with pentane (16 mL) in a 20 mL vial. After 24 h at 25 °C and 24 h at -35 °C yellow needle crystals were obtained. These were isolated on a medium-porosity fritted filter, washed with pentane (5 mL), benzene (5 mL) and pentane (5 mL). The crystallization was repeated and the crystals dried under vacuum to yield **Y3** as yellow needles (0.21 g / 41% based on $\mathrm{YI_3}$). ^{1}H NMR (TCE-d_2, 500 MHz, 358 K): δ = 1.14 (t, 6H, Cp-$\mathrm{CH_2C}H_3$), 1.41 (m, 36H, Cp-$\mathrm{CH(C}H_3)_2$), 1.50 (d , 12H, Cp-$\mathrm{CH(C}H_3)_2$), 2.90 (q, 4H, Cp-$\mathrm{C}H_2\mathrm{CH_3}$), 3.30 (sept, 4H, Cp-$\mathrm{C}H\mathrm{(CH_3)_2}$), 3.39 (sept, 4H, Cp-$\mathrm{C}H\mathrm{(CH_3)_2}$). ^{13}C{^{1}H} NMR (TCE-d_2, 125 MHz, 348 K): δ = 15.88 (Cp-$\mathrm{CH_2}C\mathrm{H_3}$), 20.63 (Cp-$C\mathrm{H_2CH_3}$), 22.56 (Cp-$\mathrm{CH(}C\mathrm{H_3)_2}$), 22.95 (Cp-$\mathrm{CH(}C\mathrm{H_3)_2}$), 23.33 (Cp-$\mathrm{CH(}C\mathrm{H_3)_2}$), 24.41 (Cp-$\mathrm{CH(}C\mathrm{H_3)_2}$) 26.59 (Cp-$C\mathrm{H(CH_3)_2}$), 27.25 (Cp-$C\mathrm{H(CH_3)_2}$), 132.89 (-C(*i*Pr)-*C*(Et)-C(*i*Pr)-), 137.24 (-C(*i*Pr)-*C*(*i*Pr)-C(*i*Pr)-), 138.20 (-C(Et)-*C*(*i*Pr)-C(*i*Pr)-). $\mathrm{C_{62}H_{66}BF_{20}Y}$ (1290.89): calcd (%) C 57.69, H 5.15, Y 6.89; found (%) C 57.45, H 5.06, Y 7.01.

Synthesis of $[\mathrm{Y(Cp}^{i\mathrm{Pr4}})_2][\mathrm{B(C_6F_5)_4}]$ (Y1). Following the general procedure used for synthesis of **Y3**, **Y1** was synthesized from $\mathrm{YI_3}$ (0.22 g / 0.47 mmol), $\mathrm{NaCp}^{i\mathrm{Pr4}}$ (0.30 g / 1.17 mmol) and $[\mathrm{H(SiEt_3)_2}][\mathrm{B(C_6F_5)_4}]$ (0.34 g / 0.37 mmol). The product was recrystallized twice using the same method outlined for **Y3** to yield colorless prisms of **Y1** (0.30 g / 52% based on $\mathrm{YI_3}$). ^{1}H NMR ($\mathrm{CD_2Cl_2}$, 500 MHz, 298 K): δ = 1.01 (d, 12H, Cp-$\mathrm{CH(C}H_3)_2$), 1.32 (d , 12H, Cp-$\mathrm{CH(C}H_3)_2$), 1.36 (d, 12H, Cp-$\mathrm{CH(C}H_3)_2$), 1.52 (d, 12H, Cp-$\mathrm{CH(C}H_3)_2$), 3.04 (sept, 4H, Cp-$\mathrm{C}H\mathrm{(CH_3)_2}$), 3.25 (sept, 4H, Cp-$\mathrm{C}H\mathrm{(CH_3)_2}$), 6.57 (s, 2H, Cp-*H*). ^{13}C{^{1}H} NMR ($\mathrm{CD_2Cl_2}$, 125 MHz, 298 K): δ = 22.49, 22.90, 23.13, 26.90, 27.15, 28.38, 110.57, 135.90, 137.84, 140.87, 147.79, 149.68. $\mathrm{C_{58}H_{58}BF_{20}Y}$ (1234.79): calcd (%) C 56.42, H 4.73, Y 7.20; found (%) C 55.95, H 4.72, Y 7.21.

Synthesis of $[\mathrm{Y(Cp}^{i\mathrm{Pr4Me}})_2][\mathrm{B(C_6F_5)_4}]$ (Y2). Following the general procedure used for synthesis of **Y3**, **Y2** was synthesized from $\mathrm{YI_3}$ (0.17 g / 0.36 mmol), $\mathrm{NaCp}^{i\mathrm{Pr4Me}}$ (0.25 g / 0.92 mmol) and $[\mathrm{H(SiEt_3)_2}][\mathrm{B(C_6F_5)_4}]$ (0.27 g / 0.30 mmol). The product was recrystallized twice using the same method outlined for **Y3** to yield yellow prisms of **Y2** (0.24 g / 51% based on YI_3). ^1H NMR (TCE-d_2, 300 MHz, 348 K): δ = 1.26 (d, 12H, Cp-CH(C*H*$_3$)$_2$), 1.40 (d , 12H, Cp-CH(C*H*$_3$)$_2$), 1.41 (d, 12H, Cp-CH(C*H*$_3$)$_2$), 1.52 (d, 12H, Cp-CH(C*H*$_3$)$_2$), 3.30 (sept, 4H, Cp-C*H*(CH$_3$)$_2$), 3.37 (sept, 4H, Cp-C*H*(CH$_3$)$_2$). $^{13}C\{^1H\}$ NMR (TCE-d_2, 125 MHz, 348 K): δ = 14.00 (Cp-*C*H$_3$), 22.60 (Cp-CH(*C*H$_3$)$_2$), 22.67 (Cp-CH(*C*H$_3$)$_2$), 22.87 (Cp-CH(*C*H$_3$)$_2$), 23.01 (Cp-CH(*C*H$_3$)$_2$), 26.42 (Cp-*C*H(CH$_3$)$_2$), 27.39 (Cp-*C*H(CH$_3$)$_2$), 127.37 (-C(*i*Pr)-*C*(Me)-C(*i*Pr)-), 136.55 (-C(*i*Pr)-*C*(*i*Pr)-C(*i*Pr)-), 139.01 (-C(Me)-*C*(*i*Pr)-C(*i*Pr)-). $C_{60}H_{62}BF_{20}Y$ (1262.84): calcd (%) C 57.07, H 4.95, Y 7.04; found (%) C 56.80, H 4.81, Y 7.16.

Synthesis of [Y(Cp^{iPr5})$_2$][B(C$_6$F$_5$)$_4$] (Y4). Following the general procedure used for synthesis of **Y3**, **Y4** was synthesized from YI_3 (0.19 g / 0.40 mmol), NaCp^{iPr5} (0.30 g / 1.00 mmol) and $[H(SiEt_3)_2][B(C_6F_5)_4]$ (0.29 g / 0.32 mmol). The product was recrystallized three times using the same method outlined for **Y3** to yield yellow needles of **Y4** (0.16 g / 30% based on YI_3). ^1H NMR (CD_2Cl_2, 500 MHz, 263 K): δ = {1.07 outer CH_3 of both isomers} (d, 30H, Cp-CH(C*H*$_3$)$_2$), {1.66 inner CH_3 of isomer A, 1.69 inner CH_3 of isomer B} (d , 30H, Cp-CH(C*H*$_3$)$_2$), 3.35 (sept, 10H, Cp-C*H*(CH$_3$)$_2$). $^{13}C\{^1H\}$ NMR (CD_2Cl_2, 125 MHz, 263 K): δ = 23.62 (Cp-CH(*C*H$_3$)$_2$), 23.70 (Cp-CH(*C*H$_3$)$_2$), 24.95 (Cp-CH(*C*H$_3$)$_2$), 25.62 (Cp-CH(*C*H$_3$)$_2$), 27.42 (Cp-*C*H(CH$_3$)$_2$), 27.48 (Cp-*C*H(CH$_3$)$_2$), 140.17 (-C(*i*Pr)-*C*(*i*Pr)-C(*i*Pr)-). $C_{64}H_{70}BF_{20}Y$ (1318.95): calcd (%) C 58.28, H 5.35, Y 6.74; found (%) C 57.73, H 5.05, Y 6.35.

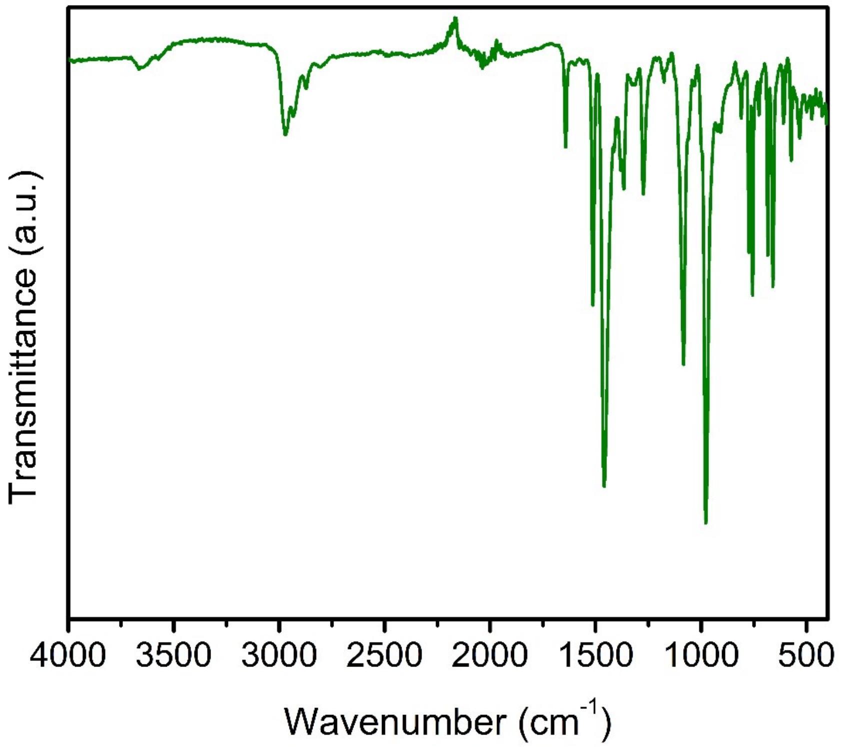

Figure S1. Infrared spectrum of **1**.

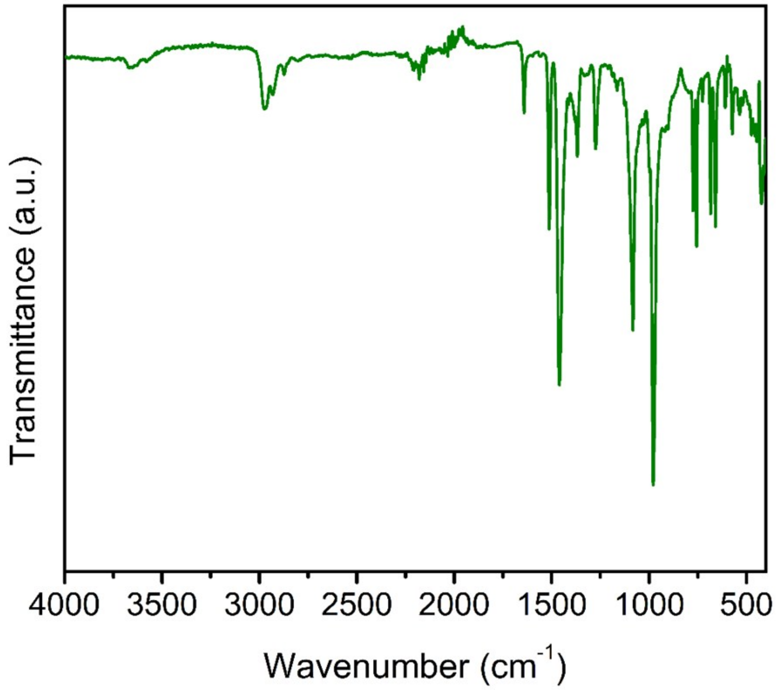

Figure S2. Infrared spectrum of **2**.

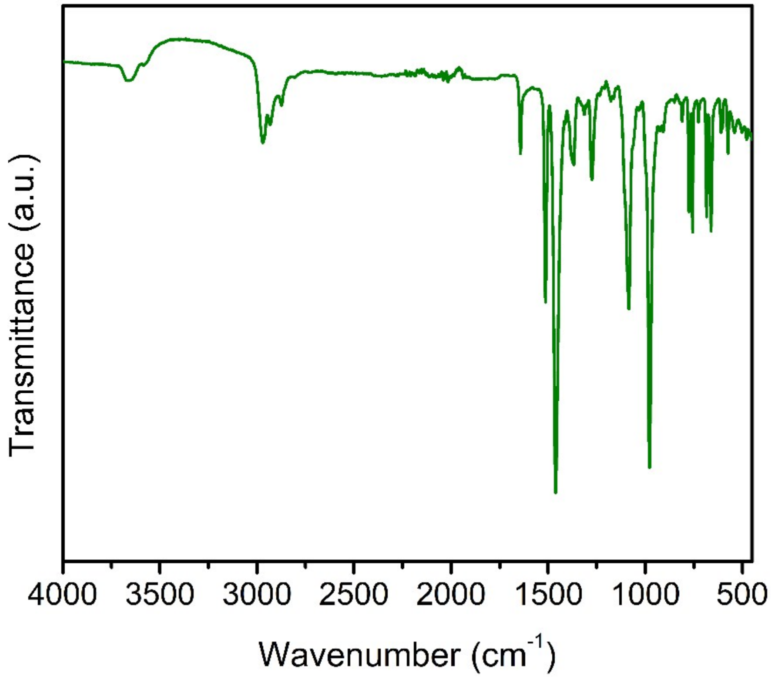

Figure S3. Infrared spectrum of **3**.

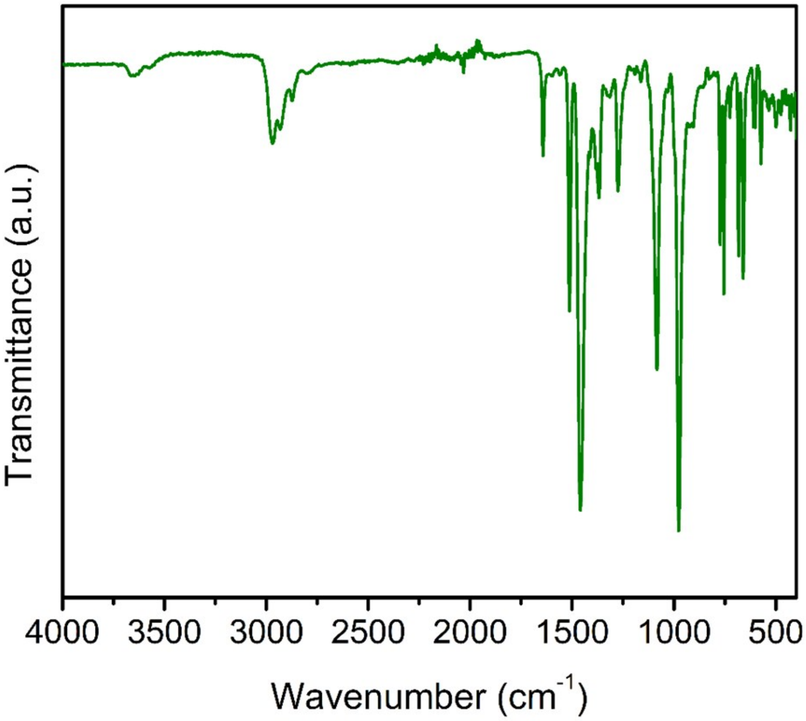

Figure S4. Infrared spectrum of **4**.

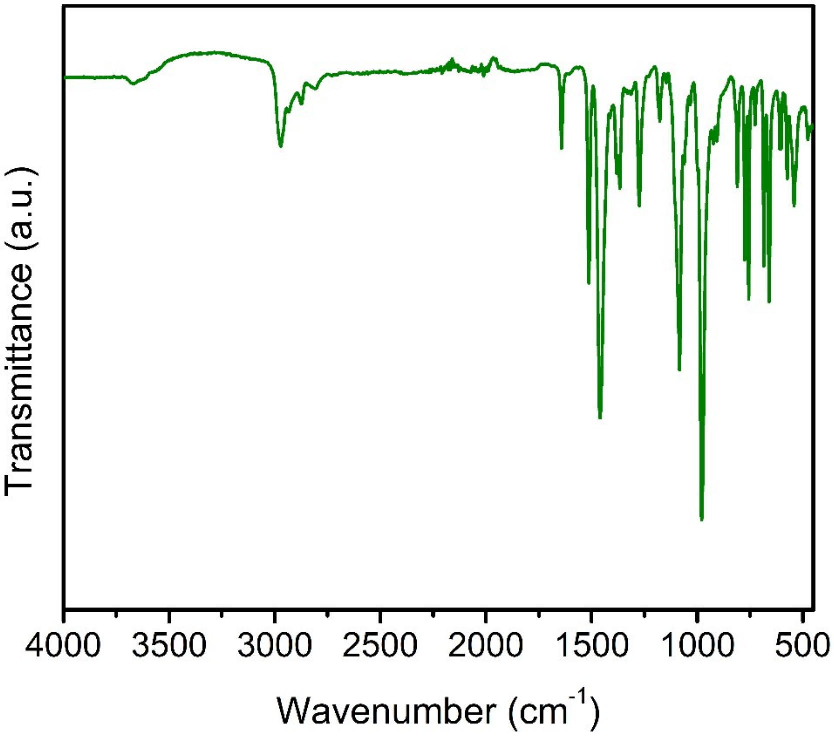

Figure S5. Infrared spectrum of **Y1**.

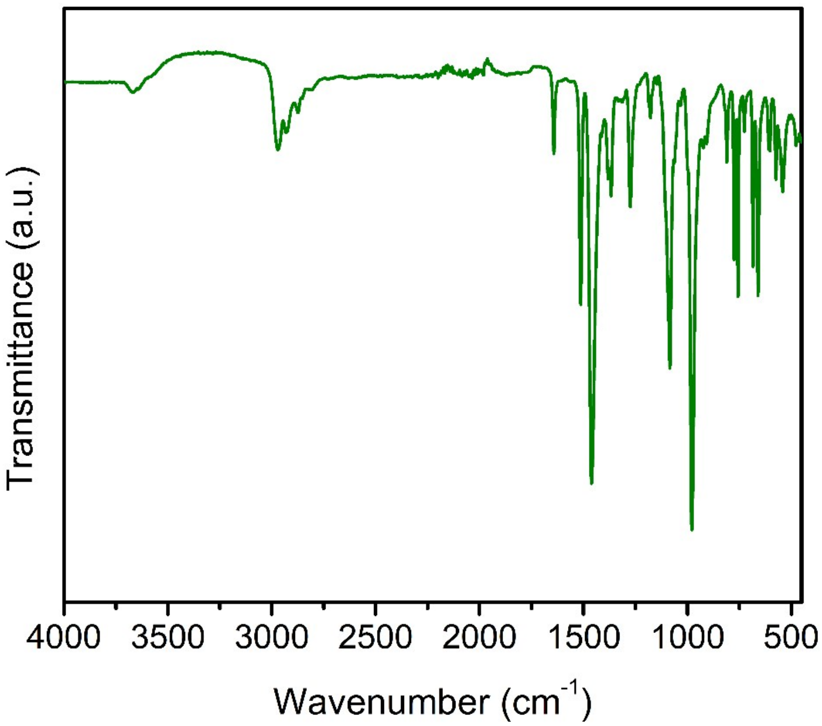

Figure S6. Infrared spectrum of **Y2**.

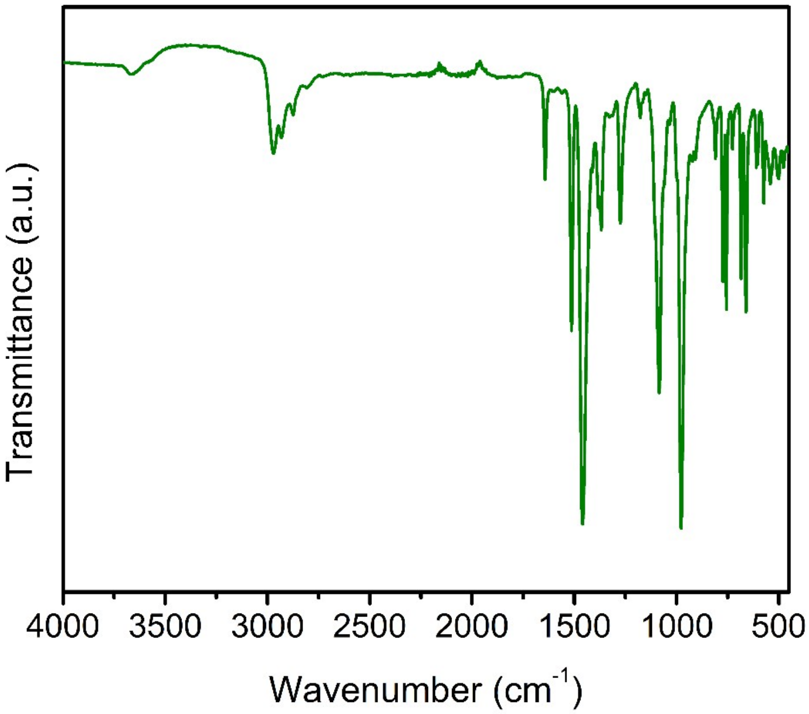

Figure S7. Infrared spectrum of **Y3**.

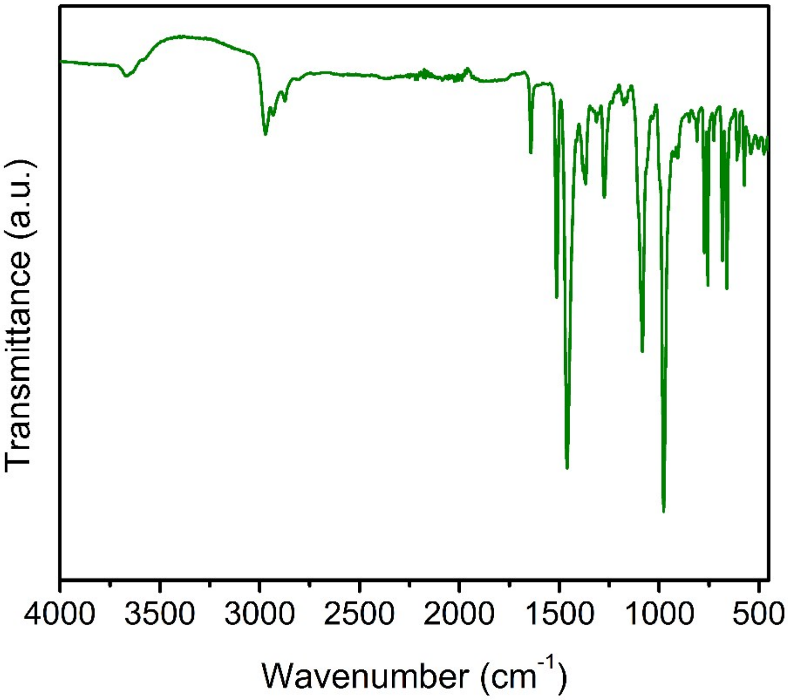

Figure S8. Infrared spectrum of **Y4**.

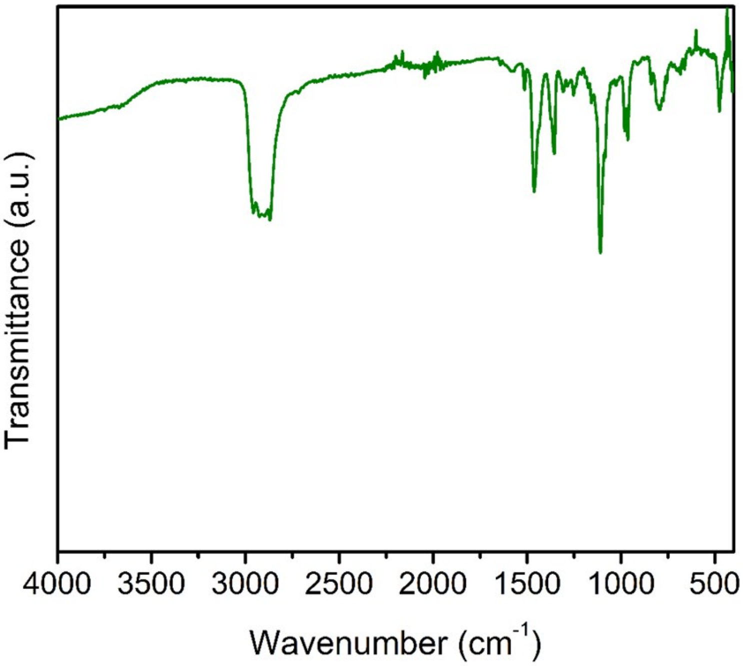

Figure S9. Infrared spectrum of NaCp$^{i\mathrm{Pr4Me}}$.

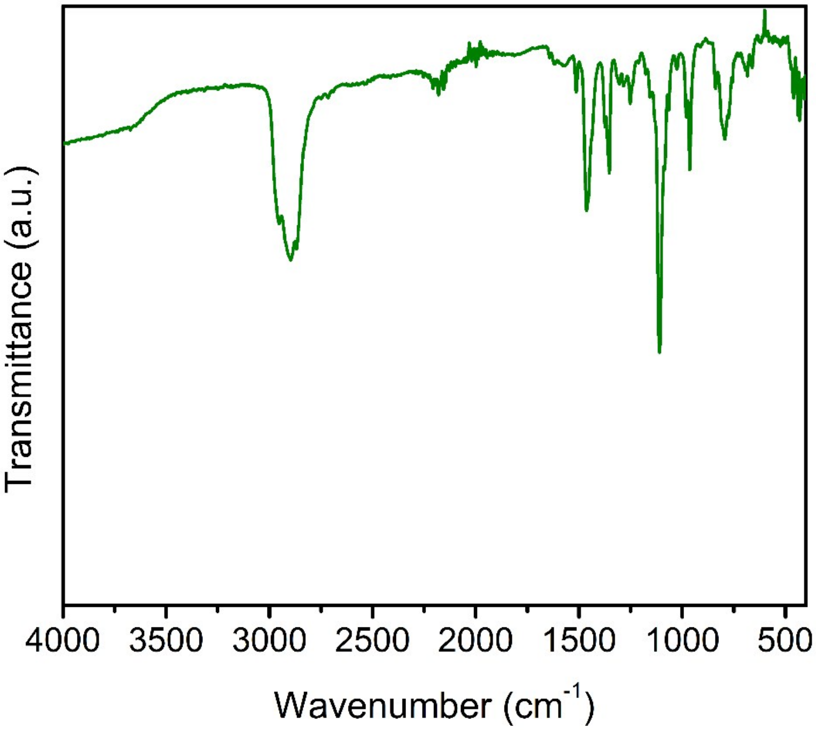

Figure S10. Infrared spectrum of NaCp$^{i\mathrm{Pr4Et}}$.

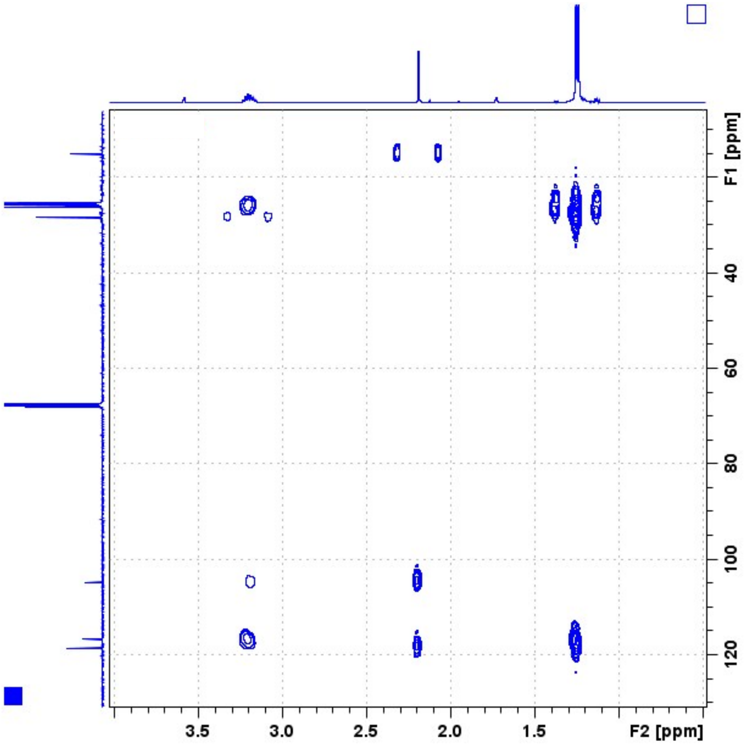

Figure S11. ^{13}C-^{1}H HMBC spectrum of NaCp$^{i\mathrm{Pr4Me}}$ in THF-d_8 at 65 °C.

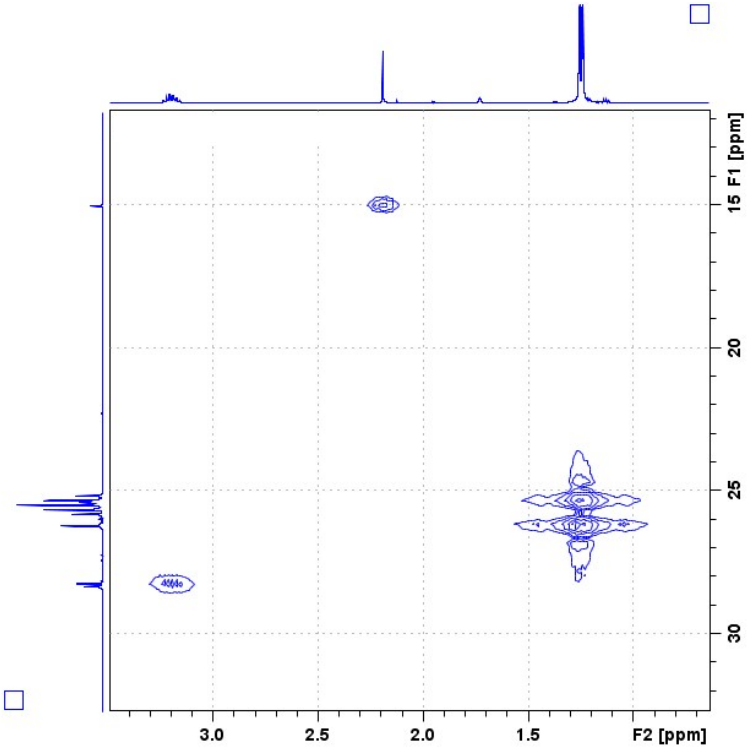

Figure S12. ^{13}C-^{1}H HMQC spectrum of NaCp$^{i\text{Pr}4\text{Me}}$ in THF-d$_8$ at 65 °C.

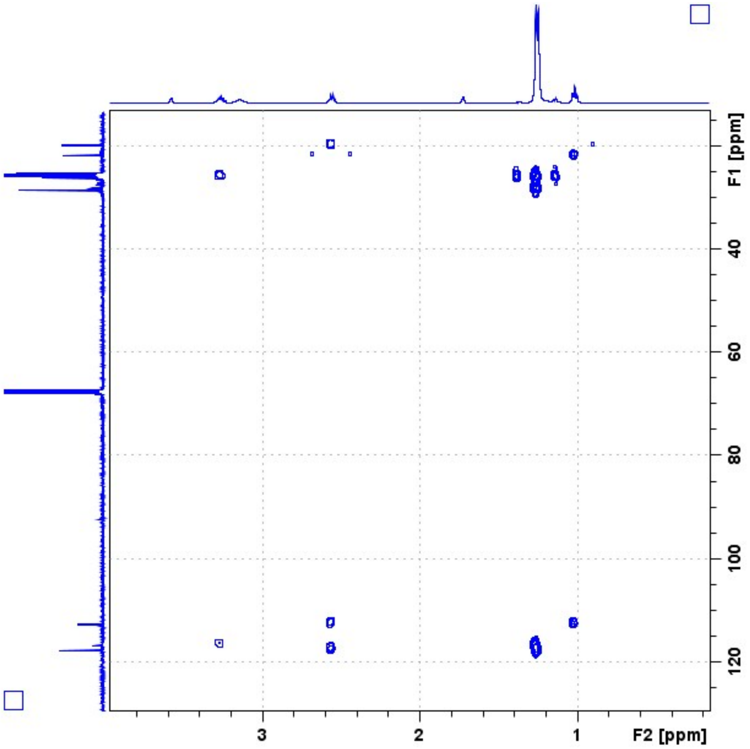

Figure S13. ^{13}C-^{1}H HMBC spectrum of NaCp$^{i\text{Pr}4\text{Et}}$ in THF-d$_8$ at 65 °C.

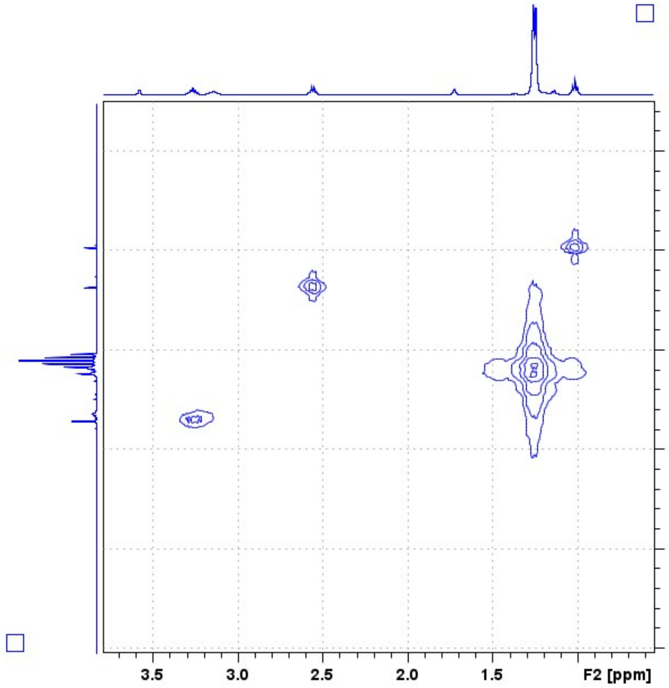

Figure S14. ^{13}C-^{1}H HMQC spectrum of NaCp$^{i\mathrm{Pr4Et}}$ in THF-d$_8$ at 65 °C.

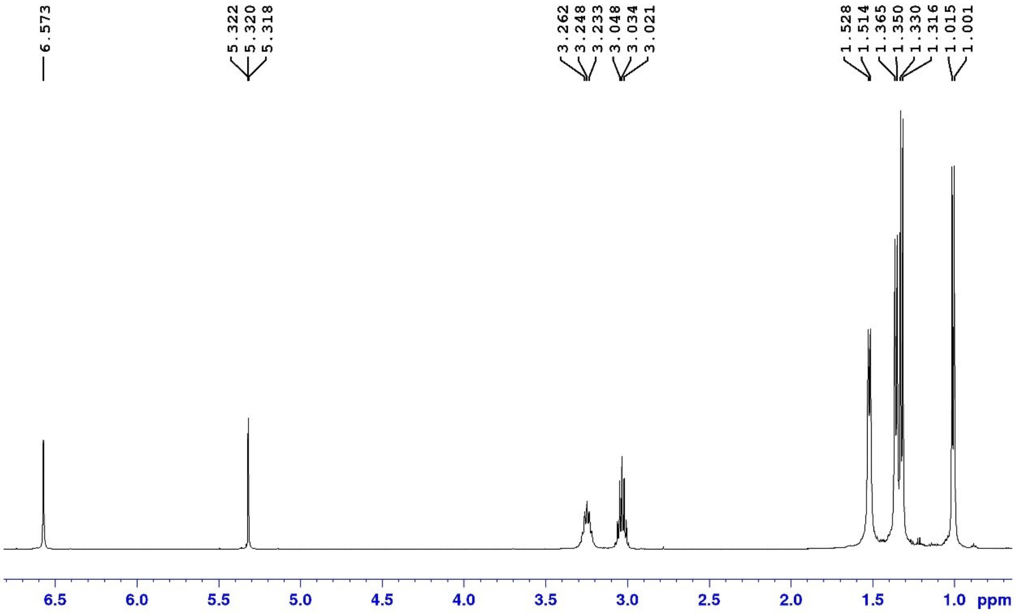

Figure S15. ^{1}H NMR spectrum of **Y1** in CD$_2$Cl$_2$ at 25 °C.

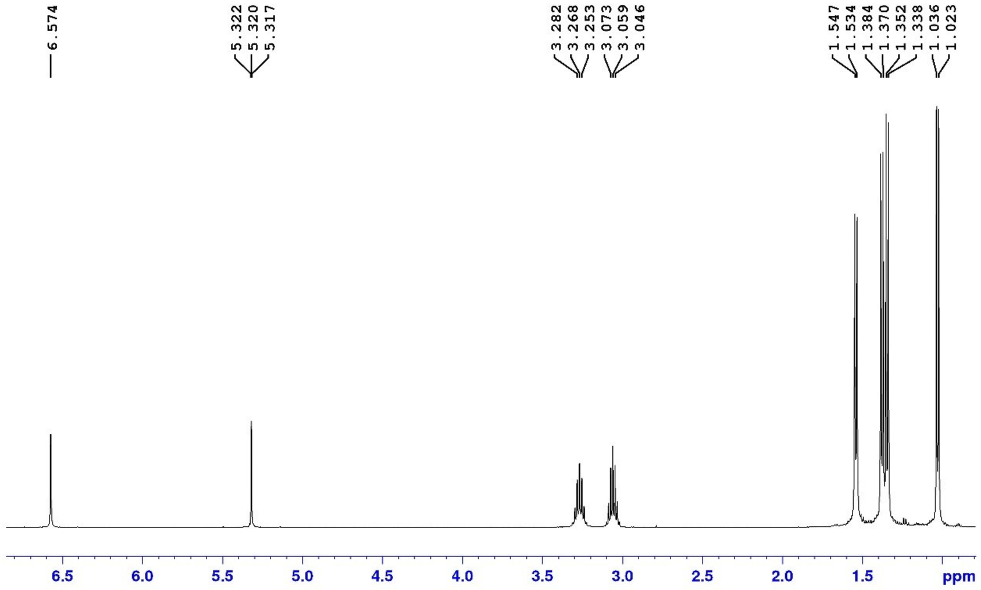

Figure S16. ^{1}H NMR spectrum of **Y1** in CD_2Cl_2 at 45 °C.

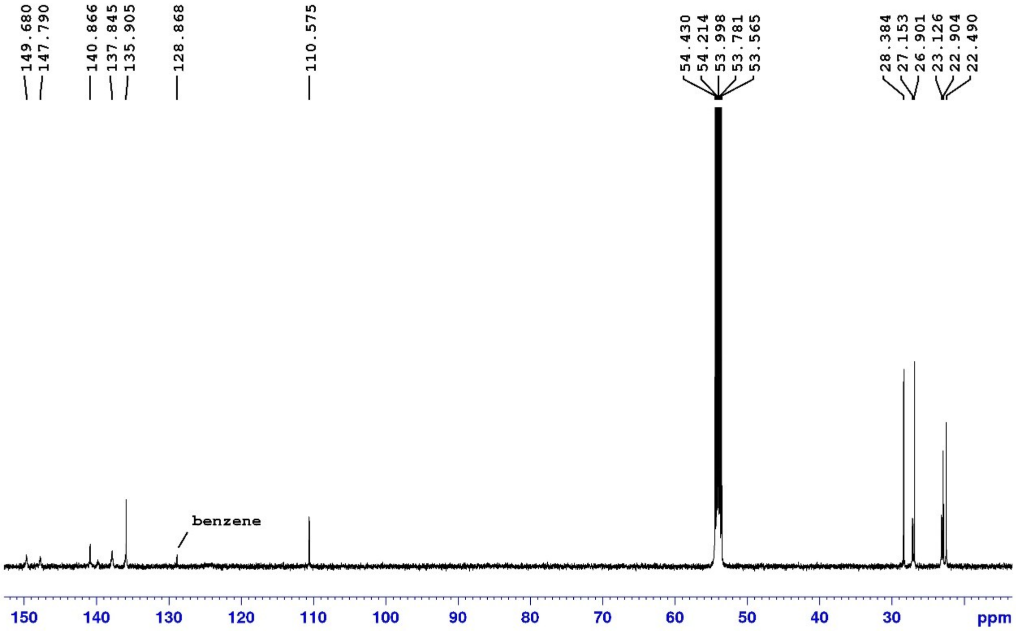

Figure S17. ^{13}C NMR spectrum of **Y1** in CD_2Cl_2 at 25 °C.

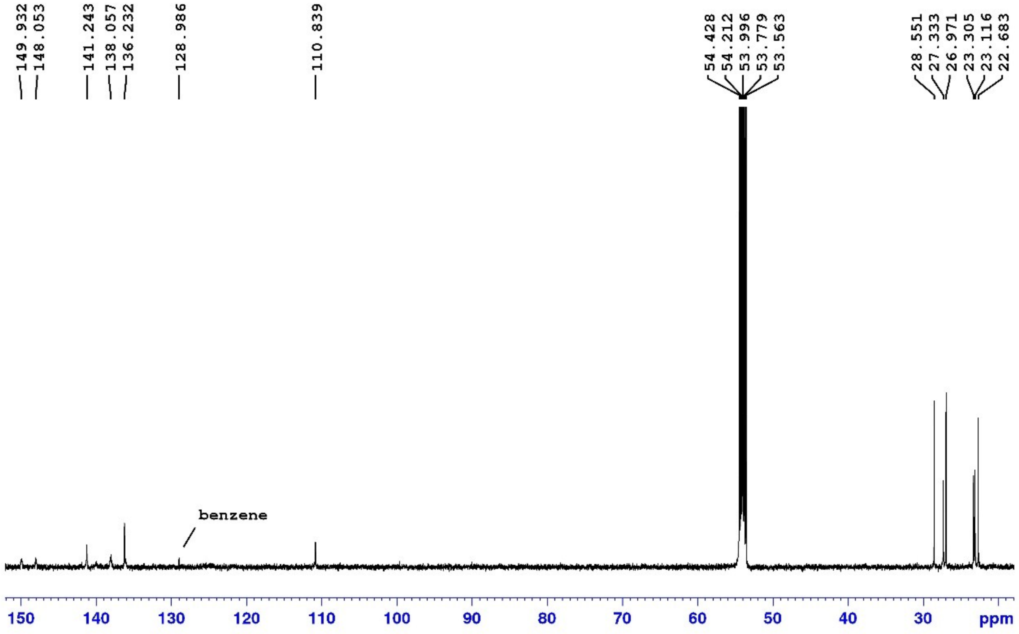

Figure S18. ^{13}C NMR spectrum of **Y1** in CD_2Cl_2 at 45 °C.

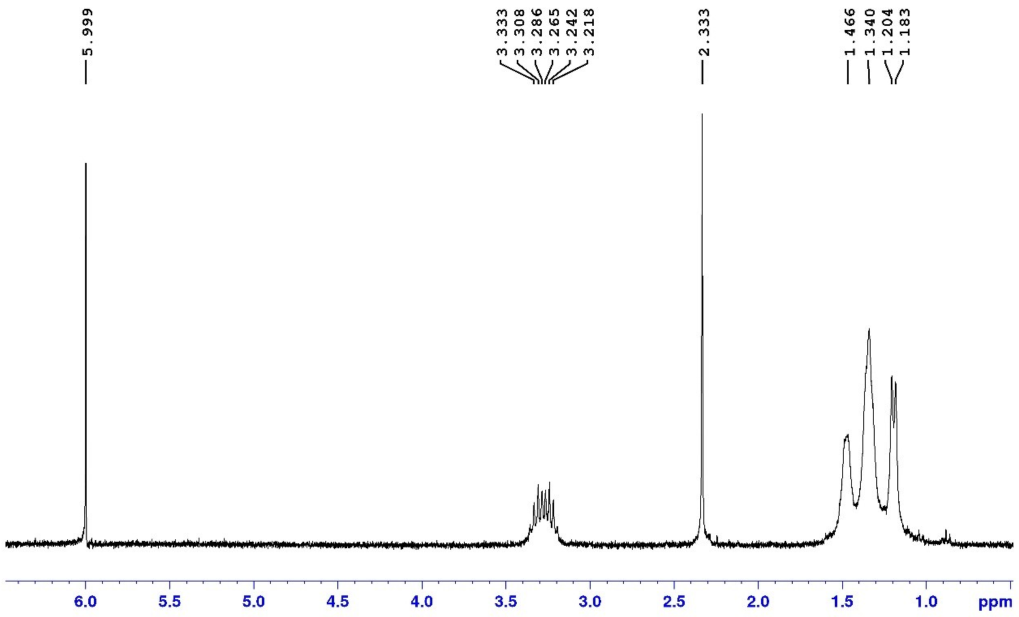

Figure S19. ^{1}H NMR spectrum of **Y2** in TCE-d_2 at 25 °C.

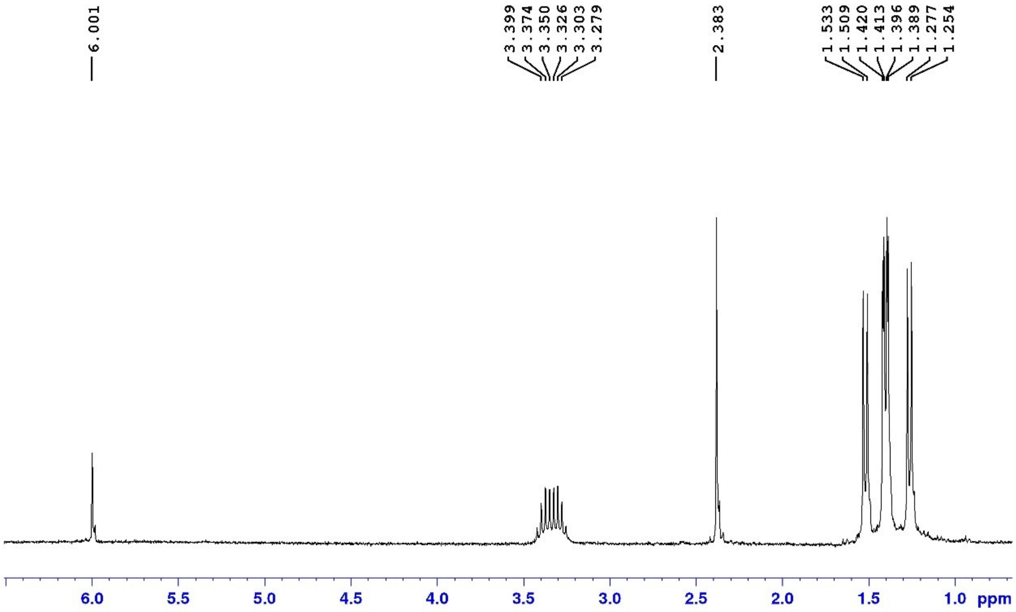

Figure S20. ^{1}H NMR spectrum of **Y2** in TCE-d_2 at 75 °C.

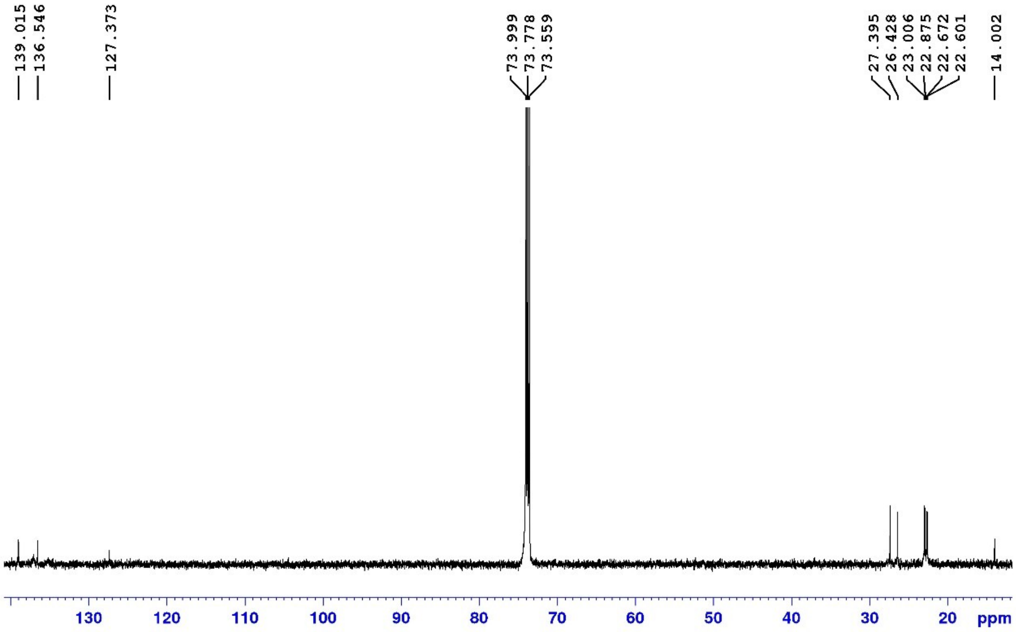

Figure S21. ^{13}C NMR spectrum of **Y2** in TCE-d_2 at 75 °C.

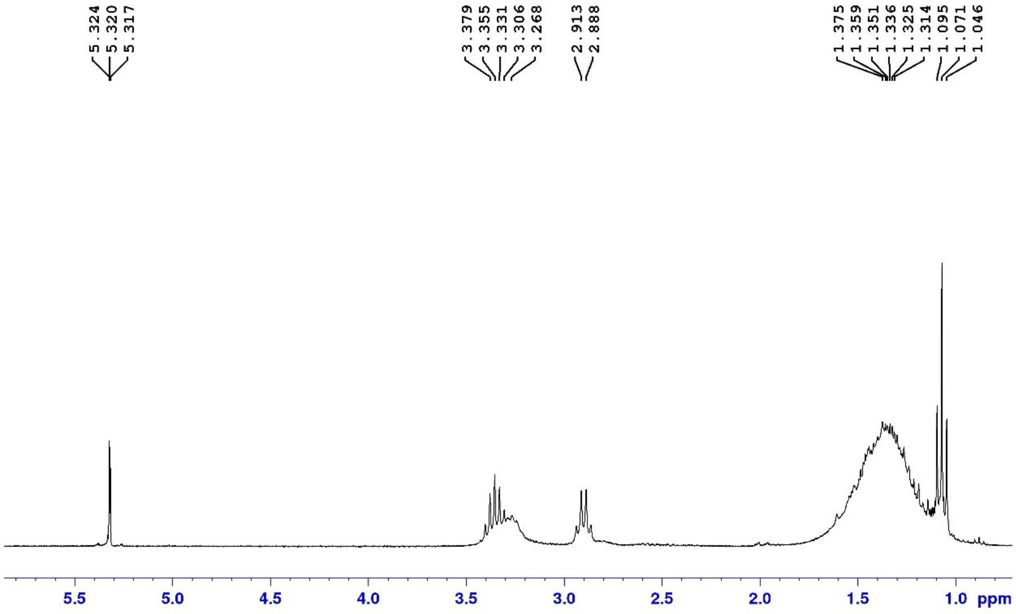

Figure S22. ^{1}H NMR spectrum of **Y3** in CD_2Cl_2 at 25 °C.

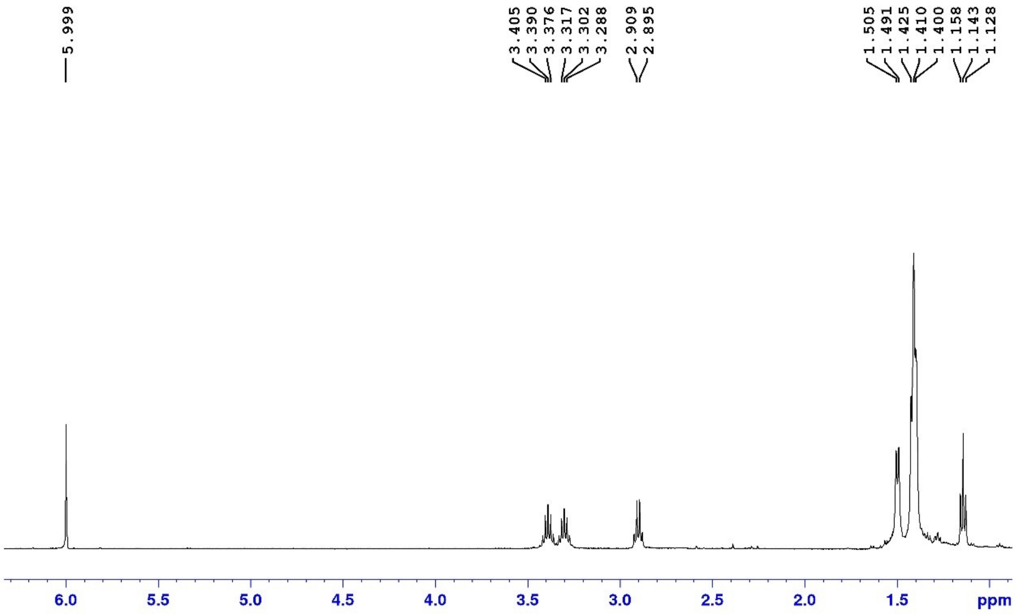

Figure S23. ^{1}H NMR spectrum of **Y3** in TCE-d_2 at 85 °C.

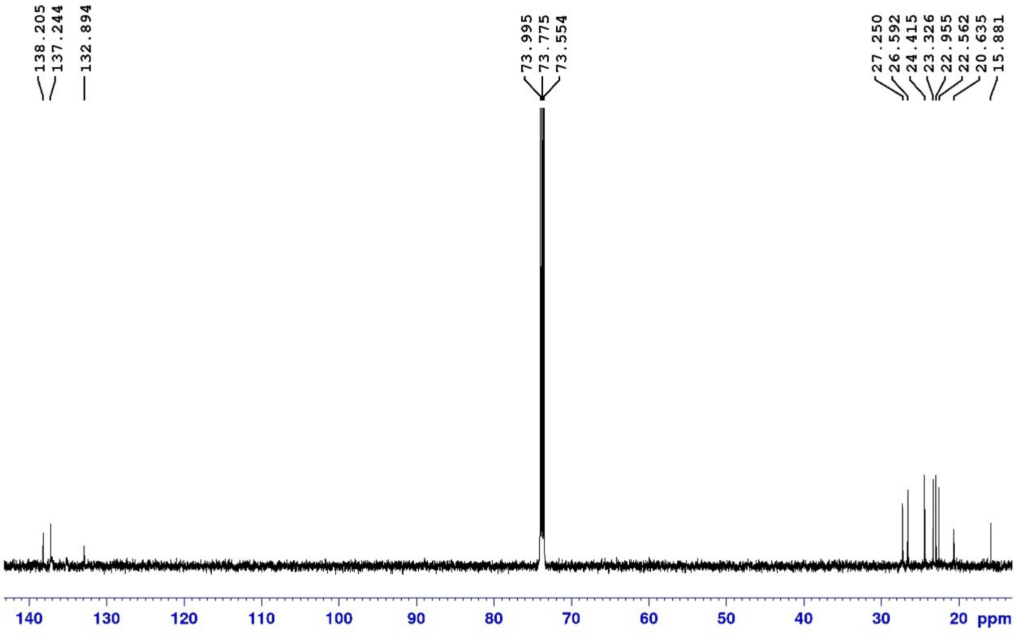

Figure S24. ^{13}C NMR spectrum of **Y3** in TCE-d$_2$ at 75 °C.

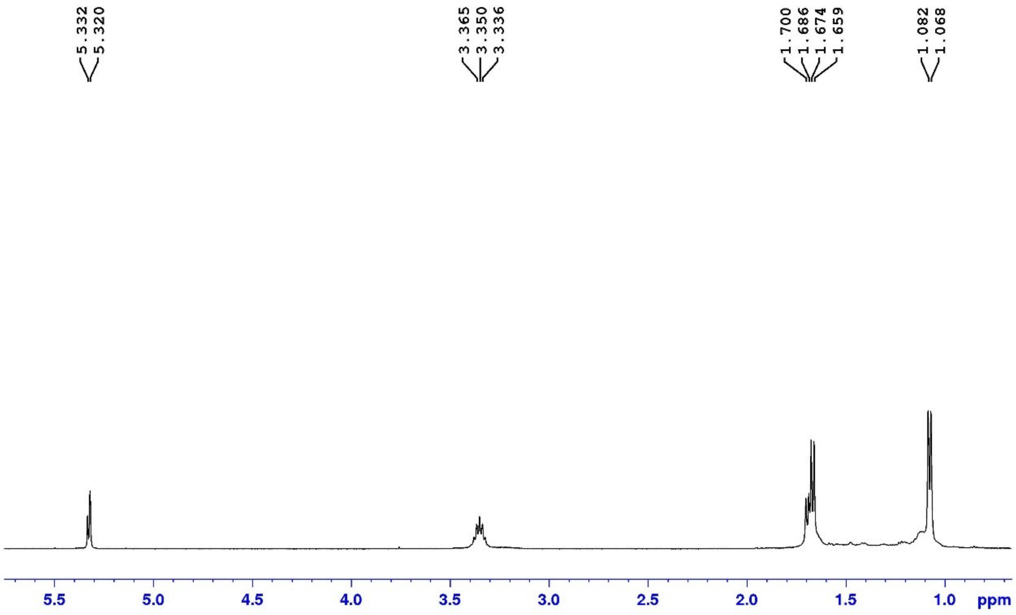

Figure S25. ^{1}H NMR spectrum of **Y4** in CD$_2$Cl$_2$ at -10 °C.

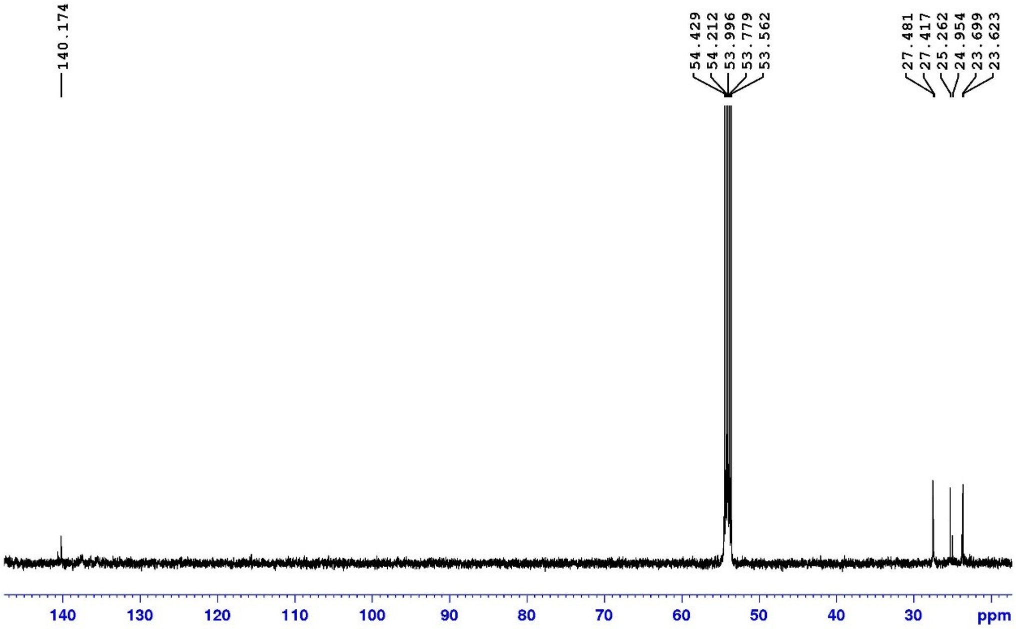

Figure S26. ^{13}C NMR spectrum of **Y4** in CD_2Cl_2 at -10 °C

X-ray Crystallography Data Collection and Refinement Details

Single crystal X-ray diffraction data of **1** and **Y1-Y4** were collected as follows. The sample was coated with Parabar oil and mounted on a MiTeGen polyimide loop in a nitrogen filled glovebox. The X-ray intensity data were measured using a Bruker SMART Apex II diffractometer at 100 K under a N2 stream of an Oxford Cryostems Cryostream with MoKα radiation (graphite monochrometer). Data was collected from four 180° ω scans with 0.5° steps at 90° rotation intervals about φ and a CCD detector distance of 5cm. The frames were integrated with the Bruker SAINT Software package using a narrow-frame algorithm.[1]

Single crystal X-ray diffraction data of **2**–**4** were collected at Beamline 12.2.1 at the Advanced Light Source, Lawrence Berkeley National Laboratory using synchrotron radiation ($\lambda = 0.7288$ Å). Single crystals were coated with Paratone-N oil, mounted on a MiTeGen loop, and frozen at 100 K under a N_2 stream of an Oxford Cryostems Cryostream 700 Plus on a Bruker AXS D8 diffractometer. Data were collected through a combination of 4° and 1° φ and ω scans with a Bruker PHOTON 100 CMOS detector. Data reduction was performed through SAINT and absorption correction through SADABS,[2] via Bruker AXS APEX III software.[3] Structure solutions were performed by SHELXT using the direct method and were refined by least-square refinement against F^2 by SHELXL following standard procedures through the integrated structure analysis program OLEX2.[4-6]

$[Dy(Cp^{iPr4H})_2][B(C_6F_5)_4]$ (1). The compound crystallized in the space group $P2_1$ with two molecules in the asymmetric unit. Initial space group determination suggested significant symmetry fulfillment of an orthorhombic $P2_12_12_1$ cell, which pointed to the sign of pseudo-merohedral twinning about a two-fold rotational axis along the *a* axis. The structure was best modeled in $P2_1$ with a two-fold rotational axis along *a* as a twin law. In addition, Flack parameter refinement indicated that the crystal was also twinned by inversion. Refinement with four-component twin yielded the twin ratio of 0.29:0.289:0.212:0.209. As a result of significant twinning of the crystal, structure refinement was accomplished only through extensive application of restraints, as discussed below. It should be noted that restrained GooF of 1.059 differs only slightly from GooF of 1.063, indicating that the restraints were appropriately applied. All non-H atoms were refined anisotropically; H atoms were placed on the geometrically calculated positions using the riding model.

Anisotropic refinement of the Cp rings was stabilized by the application of equal anisotropic displacement parameters within the groups of five C atoms of the Cp rings (C1 to C5, C18 to C22, and C52 to C56), the four tertiary C atoms of the isopropyl groups (C6, C9, C12, C15; C23, C26, C29, C32; C40, C43, C46, C49; and C57, C60, C63, C66), the eight terminal –CH_3 arms of the isopropyl groups (C7, C8, C10, C11, C13, C14, C16,C17; C24, C25, C27, C28, C30, C31, C33, C34; C41, C42, C44, C45, C47, C48, C50, C51; and C58, C59, C61, C62, C64, C65, C67, C68). These sets of equal anisotropic displacement parameters were chosen such that the anisotropic displacement parameters would scale with the degree of freedom of the Cp rings (i.e., terminal –CH_3 groups fluctuate more than planar C_5 ring, etc.). The two $[B(C_6F_5)_4]^-$ anions in the asymmetric unit were also subjected to equal anisotropic displacement parameters restraints: five F atoms on the same phenyl group were restrained to have the same anisotropic parameters. Five out of eight phenyl rings of the two $[B(C_6F_5)_4]^-$ anions were subjected to equal anisotropic displacement parameters restraints. The phenyl rings were constrained to assume the ideal planar six-membered ring geometry via AFIX 66 commands. The remaining phenyl rings and the two B atoms were stabilized by the enhanced rigid bond restraints. A rigid bond restraint was applied to one Cp ring (C35 to C51), for which equal anisotropic displacement parameters restraint was not necessary. Anomalous electron density was found near C42, which was found to interfere with modeling the isopropyl group. Therefore, C40–C41 and C40–C42 distances were restrained to a fixed value of 1.54 Å.

[Dy(Cp$^{i\mathrm{Pr4Me}}$)$_2$][B(C$_6$F$_5$)$_4$] (2). The compound crystallized in the $P2_1/c$ space group with two molecules in the asymmetric unit. The crystal was found to be twinned by pseudo-merohedry, and a two-fold rotational axis along the *a* axis was used as a twin law. Twin refinement results in a two-component twin with a ratio of 0.82:0.18. For each dysprosenium cation in the structure, one Cp ring was found to be disordered over two positions. The occupancies of the two components were refined while constraining the sum to unity and yielded ratios of 0.589:0.411 and 0.636:0.364 for the first and second dysprosenium ions, respectively. In refining the Cp disorder, the distance between C65A and C66A was restrained. Anisotropic displacement parameters of each disordered Cp ring were restrained to be the same in order to stabilize the refinement. These restraints were necessary as enhanced rigid bond restraints were found to be insufficient in modeling the disorder. Hydrogen atoms were placed on the geometrically calculated positions using the riding model. Anti-bumping restraint was applied to prevent short H···H contacts found in the disordered Cp moieties.

[Dy(Cp$^{i\mathrm{Pr4Et}}$)$_2$][B(C$_6$F$_5$)$_4$] (3). The compound crystallized in the $P2_1/n$ space group with one molecule in the asymmetric unit. All non-H atoms were refined anisotropically. For each Cp ring, one of the isopropyl groups adjacent to the ethyl substituent exhibited signs of disorder. For the first Cp ring, the isopropyl group was modeled such that one –CH$_3$ group (C38) was disordered over two positions. Refinement yielded an occupancy ratio of 0.63:0.37. For the second Cp ring, modeling the disorder did not yield reasonable model. Thus, the isopropyl group was modeled with only one configuration, even though the anisotropic displacement parameter of C10 is clearly elongated. These two isopropyl groups were subjected to rigid bond restraint in order to stabilize the structure refinement. Hydrogen atoms were placed on the geometrically calculated positions using the riding model.

[Dy(Cp$^{i\mathrm{Pr5}}$)$_2$][B(C$_6$F$_5$)$_4$] (4). The compound crystallized in the $P2_1/n$ space group with one molecule in the asymmetric unit. Anisotropic refinement of the Dy atom resulted in unusually large thermal displacement parameters, suggesting a disorder of the Dy atom. Reasonable thermal displacement parameters were achieved when the Dy atom was modeled over four positions. The occupancy sum of the four Dy positions was constrained to unity, and the occupancy refined to the ratio of 0.408:0.275:0.119:0.197.. It is interesting to note that the four Dy positions approximately lie in the same plane (RMS deviation = 0.0374), which might indicate that the Dy atom moves freely in between the two Cp rings, which have an angle of only 7.03(62)° between each other. The ten isopropyl groups on the two Cp rings were found to be disordered and were modeled over two positions. Refinement of the disordered isopropyl groups were stabilized through application of 1,2 (CH–CH$_3$) and 1,3 (CH$_3$···CH$_3$) distance restraints. The C$_{\mathrm{Cp}}$–C$_{\mathrm{Cp}}$–C(H) angles were restrained to be the same. All non-H atoms were refined anisotropically. Refinement of the disordered isopropyl groups were stabilized through application of 1,2 ($CH–CH_3$) and 1,3 ($CH_3 \cdots CH_3$) distance restraints. The $C_{Cp}–C_{Cp}–C(H)$ angles were restrained to be the same.

Table S1. Structure details for [DyCp$^{iPr4R}{}_2$][B(C_6F_5)$_4$] (R = H (**1**), Me (**2**), Et (**3**), iPr (**4**)).

[DyCp$^{iPr4R}{}_2$][B(C_6F_5)$_4$], R =	H (**1**)	Me (**2**)	Et (**3**)	iPr (**4**)
Wavelength (Å)	0.71073	0.7288	0.7288	0.7288
Crystal system	Monoclinic	Monoclinic	Monoclinic	Monoclinic
Space group	$P2_1$	$P2_1/c$	$P2_1/n$	$P2_1/n$
a (Å), α (°) b (Å), β (°) c (Å), γ (°)	16.5863(17), 90 14.4989(15), 90.0586(16) 22.708(2), 90	14.50(2), 90 16.63(3), 90.027(12) 46.59(8), 90	14.9801(4), 90 23.0586(7), 90.789(2) 16.7069(5), 90	15.2173(4), 90 22.8792(6), 90.605(1) 16.8807(5), 90
V (Å^3)	5461.0(9)	11236(33)	5770.4(3)	5876.9(3)
Z	4	8	4	4
ρ_{calc} (g/cm^3)	1.591	1.580	1.571	1.574
Crystal size (mm^3)	0.338 × 0.187 × 0.044	0.107 × 0.057 × 0.05	0.130 × 0.060 × 0.050	0.110 × 0.071 × 0.071
θ range for data collection (°)	1.228 to 25.349	0.896 to 26.042	1.544 to 23.880	0.913 to 21.594
Index ranges	$-19 \leq h \leq 19$ $-17 \leq k \leq 17$ $-27 \leq l \leq 27$	$-17 \leq h \leq 17$ $-20 \leq k \leq 20$ $-56 \leq l \leq 56$	$-16 \leq h \leq 16$ $25 \leq k \leq 25$ $-18 \leq l \leq 18$	$-15 \leq h \leq 15$ $-23 \leq k \leq 23$ $-17 \leq l \leq 17$
Reflections collected	61686	163480	71765	47155
Independent reflections (R_{int})	19909 (0.0382)	20570 (0.1408)	8291 (0.0868)	6341 (0.0986)
Completeness (%)	99.8	100.0	100.0	100.0
Data / restraints / parameters	19909 / 93 / 634	20570 / 28 / 1414	8291 / 8 / 767	6341 / 693 / 1085
Goodness-of-fit on F^2	1.069	1.035	1.056	1.060
R_1, wR_2 [$I > 2\sigma(I)$]	0.0721, 0.1810	0.0570, 0.1354	0.0682, 0.1589	0.0650, 0.1700
R_1, wR_2 (all data)	0.0756, 0.1851	0.0761, 0.1497	0.0854, 0.1711	0.0732, 0.1759

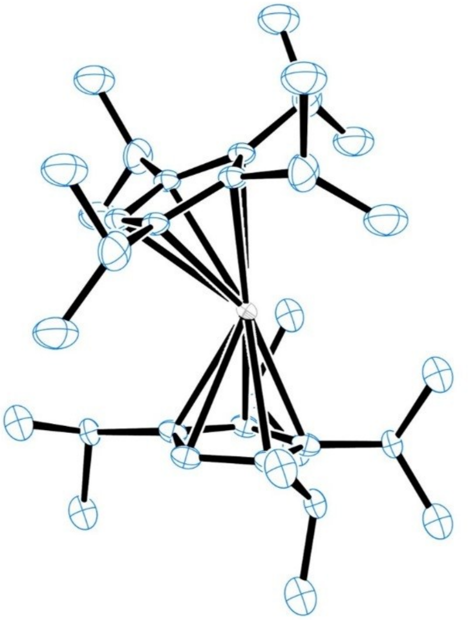

Figure S27. Solid-state structure of one of the [Dy(Cp$^{i\text{Pr4H}}$)$_2$]$^+$ cations in **1** with thermal ellipsoids at the 50% probability level. Hyrdogen atoms are omitted for clarity

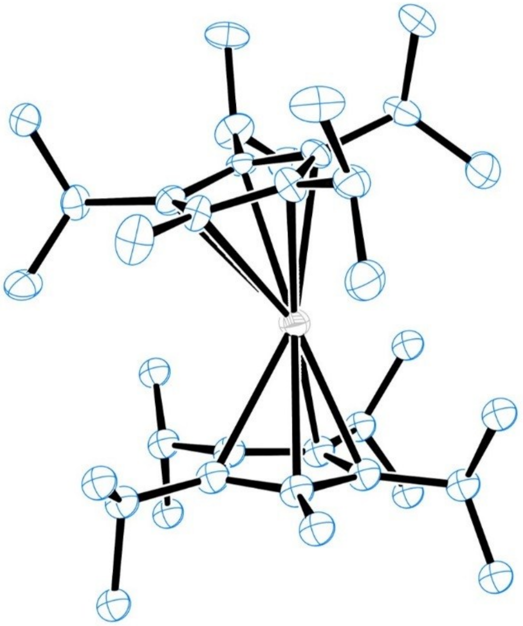

Figure S28. Solid-state structure of one of the [Dy(Cp$^{i\text{Pr4Me}}$)$_2$]$^+$ cations in **2** with thermal ellipsoids at the 50% probability level. Hyrdogen atoms and the second disordered component Cp ring are omitted for clarity.

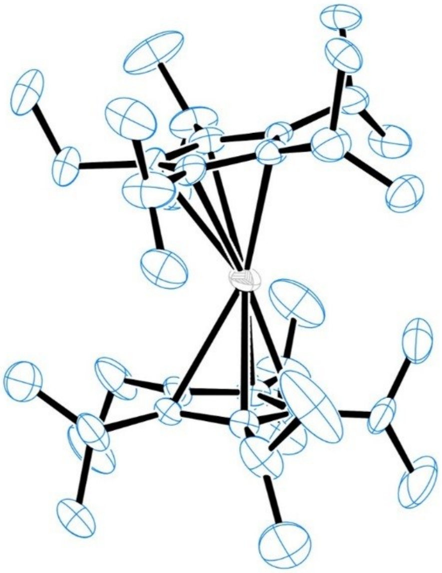

Figure S29. Solid-state structure of the [Dy(Cp$^{i\mathrm{Pr4Et}}$)$_2$]$^+$ cation in **3** with thermal ellipsoids at the 30% probability level. Hydrogen atoms are omitted for clarity.

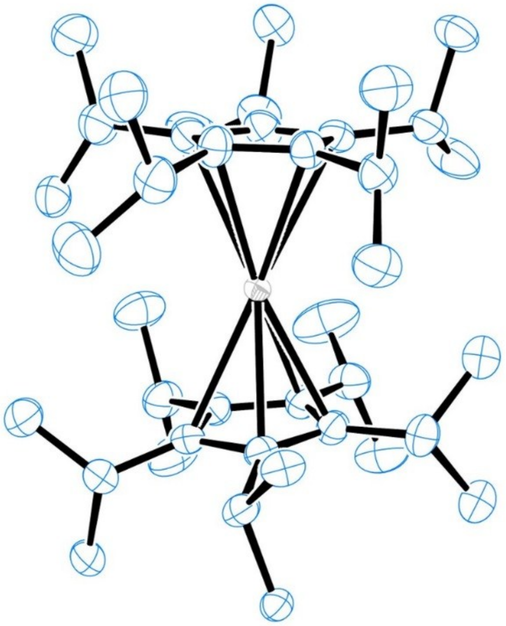

Figure S30. Solid-state structure of the [Dy(Cp$^{i\mathrm{Pr5}}$)$_2$]$^+$ cation in **4** with thermal ellipsoids at the 30% probability level. Hydrogen atoms and the disordered component are omitted for clarity.

Table S2. Selected bond distances (Å) and angles (°) for **1**–**4**.

R =	H (**1**)	Me (**2**)	Et (**3**)	iPr (**4**)
Dy1–C1	2.60(2)	2.623(8)	2.608(8)	2.508(9)
Dy1–C2	2.58(2)	2.672(7)	2.677(7)	2.551(10)
Dy1–C3	2.57(2)	2.648(7)	2.615(7)	2.726(10)
Dy1–C4	2.63(2)	2.567(7)	2.527(7)	2.772(10)
Dy1–C5	2.58(2)	2.544(8)	2.533(7)	2.651(9)
Dy1–C1′ [a]	2.59(2)	2.619(17)	2.597(8)	2.448(10)
Dy1–C2′ [a]	2.59(2)	2.617(19)	2.607(8)	2.479(10)
Dy1–C3′ [a]	2.58(3)	2.542(15)	2.608(7)	2.704(9)
Dy1–C4′ [a]	2.54(2)	2.521(15)	2.594(7)	2.775(10)
Dy1–C5′ [a]	2.54(2)	2.580(15)	2.597(7)	2.637(10)
Dy2–C35(37)[b]	2.62(3)	2.627(8)	–	–
Dy2–C36(38)[b]	2.64(3)	2.651(7)	–	–
Dy2–C37(39)[b]	2.53(3)	2.646(7)	–	–
Dy2–C38(40)[b]	2.56(3)	2.599(7)	–	–
Dy2–C39(41)[b]	2.59(3)	2.575(8)	–	–
Dy2–C52(55)[b]	2.56(3)	2.627(19)	–	–
Dy2–C53(56)[b]	2.66(2)	2.571(15)	–	–
Dy2–C54(57)[b]	2.63(2)	2.527(17)	–	–
Dy2–C55(58)[b]	2.54(3)	2.587(16)	–	–
Dy2–C56(59)[b]	2.59(3)	2.659(18)	–	–
Dy–C(avg)	2.587(5)[d]	2.600(3)[d]	2.596(2)[d]	2.625(3)[d]
Dy1–Cp(A)[c]	2.29(2)[e]	2.311(8)[e]	2.297(8)[e]	2.358(10)[e,f]
Dy1–Cp(B)[c]	2.27(3)[e]	2.273(19)[e,f]	2.306(8)[e]	2.321(10)[e,f]
Dy2–Cp(C)[c]	2.30(3)[e]	2.319(3)[e]	–	–
Dy2–Cp(D)[c]	2.29(3)[e]	2.288(3)[e,f]	–	–
Dy–Cp(avg)	2.29(1)[d]	2.298(5)[d]	2.302(6)[d]	2.340(7)[d]
Cp(A)–Dy1–Cp(B)	148.2(8)	157.35(40)[f]	161.09(20)	157.82(18)
Cp(C)–Dy2–Cp(D)	146.4(8)	155.93(30)[f]	–	–
Cp(A)–Dy2–Cp(B)	–	–	–	158.85(40)
Cp(A)–Dy3–Cp(B)	–	–	–	167.94(152)
Cp(A)–Dy4–Cp(B)	–	–	–	163.91(90)

[a] C1′ to C5′ denote the five C atoms of the second Cp ring in the structure. These correspond to C18–C22 for **1**, C19–C23 for **2**, C20–C24 for **3**, and C21–C25 for **4**.

[b] C35(37) to C39(41) and C52(55) to C56(59) are the five C atoms of the first and second Cp rings on Dy2 in the structure of **1**(**2**).

[c] Cp(A), Cp(B), Cp(C), and Cp(D) refer to the first (C1–C5), second (C1′ to C5′) Cp rings on Dy1 and first, second Cp rings on Dy2, respectively.

[d] The standard deviation of the average value was estimated from $\sigma = \sqrt{\sum \sigma_i^2 / N}$, where σ_i is the standard deviation of each bond distance *i* and *N* is the number of distances averaged.

[e] Dy–Cp distances were measured from the Dy atom to the centroid of the Cp ring. The standard deviations are estimated as the largest esd of Dy–C distances in the respective Cp ring.

[f] The minor disordered component was not taken into account, as it shows significant deviation from typical Dy–Cp distances, likely due to artefact in disorder

$[Y(Cp^{iPr4H})_2][B(C_6F_5)_4]$ (Y1). The compound crystallized in the space group $P2_1$ with two molecules in the asymmetric unit. Initial space group determination suggested significant symmetry fulfillment of an orthorhombic $P2_12_12_1$ cell, which pointed to the sign of pseudo-merohedral twinning about a two-fold rotational axis along the *a* axis. The structure was best modeled in $P2_1$ with a two-fold rotational axis along *a* as a twin law. In addition, Flack parameter refinement indicated that the crystal was also twinned by inversion. Refinement with four-component twin yielded the twin ratio of 0.263(19):0.265(11):0.237(11):0.235(11). As a result of significant twinning of the crystal, structure refinement was accomplished only through extensive application of restraints, as discussed below. It should be noted that restrained GooF of 1.128 differs only slightly from GooF of 1.123, indicating that the restraints were appropriately applied. All non-H atoms were refined anisotropically; H atoms were placed on the geometrically calculated positions using the riding model.

One Cp^{iPr4H} ring on Y1 (C1 to C14) and its disordered ^{i}Pr group (C13A and C14A) were stabilized by the enhanced rigid bond restraints. The second $[Y(Cp^{iPr4})_2]^+$ cation has the Y atom and one Cp^{iPr4H} ligand disordered over two positions. Anisotropic refinement of the disordered Cp^{iPr4H} ring was stabilized by application of equal anisotropic displacement parameters to the 5C ring (C52 to C56 and C52C to C56C), and the four isopropyl groups (C57 to C68 and C57C to C68C). The ordered Cp ring on Y2 was stabilized by the enhanced rigid bond restraints. The Cp rings were constrained to assume ideal planar geometry through AFIX 56 commands. Some disordered isopropyl groups required restraining the C–C bond distances to stabilize the refinement. Anti-bumping restraint was applied to prevent short H···H contacts found in the disordered Cp moieties.

The two $[B(C_6F_5)_4]^-$ anions in the asymmetric unit were disordered over two positions and all B and C atoms, and F atoms were subjected to equal anisotropic displacement parameters restraints. The phenyl rings were constrained to assume the ideal planar six-membered ring geometry via AFIX 66 commands. All C–F and B–C bond distances were restrained to the appropriate values.

$[Y(Cp^{iPr4Me})_2][B(C_6F_5)_4]$ (Y2). The compound crystallized in the $P2_1/c$ space group with two molecules in the asymmetric unit. The crystal was found to be twinned by pseudo-merohedry, and a two-fold rotational axis along the *a* axis was used as a twin law. Twin refinement results in a two-component twin with a ratio of 0.5378(15):0.4622(15). For each cation in the structure, one Cp ring was found to be disordered over two positions. The occupancies of the two components were refined while constraining the sum to unity and yielded ratios of 0.58:0.42 and 0.59:0.41 for the first and second metallocenium cations, respectively. The disordered Cp rings were constrained to assume the idealized pentagon geometry using AFIX 56 commands. Anisotropic refinement of the Y atom resulted in unusually large thermal displacement parameters, suggesting a disorder of the Y atom. Reasonable thermal displacement parameters were achieved when the Y atom was modeled over two positions. The occupancy sum of the two positions was constrained to unity, and the occupancy refined to the ratio of 0.74:0.26 and 0.75:0.25 for the two molecules, respectively. Anisotropic refinement was stabilized by the enhanced rigid bond restraints. Hydrogen atoms were placed on the geometrically calculated positions using the riding model. Anti-bumping restraint was applied to prevent short H···H contacts found in the disordered Cp moieties.

[Y(Cp$^{i\mathrm{Pr4Et}}$)$_2$][B(C$_6$F$_5$)$_4$] (Y3). The compound crystallized in the $P2_1/n$ space group with one molecule in the asymmetric unit. All non-H atoms were refined anisotropically. For each Cp ring, one of the isopropyl groups adjacent to the ethyl substituent exhibited signs of disorder. For the first Cp ring, the isopropyl group was modeled such that one –CH$_3$ group (C29) was disordered over two positions. Refinement yielded an occupancy ratio of 0.655:0.345. For the second Cp ring, modeling the disorder did not yield reasonable model. Thus, the isopropyl group was modeled with only one configuration, even though the anisotropic displacement parameter of C10 is clearly elongated. These two isopropyl groups were subjected to rigid bond restraint in order to stabilize the structure refinement. Hydrogen atoms were placed on the geometrically calculated positions using the riding model. Refining one pentafluorophenyl group of the [B(C$_6$F$_5$)$_4$]$^-$ anion requires the application of a rigid bond restraint. Anti-bumping restraint was applied to prevent short H···H contacts.

[Y(Cp$^{i\mathrm{Pr5}}$)$_2$][B(C$_6$F$_5$)$_4$] (Y4). The compound crystallized in the C2/*c* space group with half a molecule in the asymmetric unit. The [B(C$_6$F$_5$)$_4$]$^-$ anion was found to be disordered over two positions. Refinement of the disordered [B(C$_6$F$_5$)$_4$]$^-$ was stabilized by the enhanced rigid bond restraints. Hydrogen atoms were placed on the geometrically calculated positions using the riding model. Only the *meso* isomer was observed in the structure.

$[YCp^{iPr4R}{}_2][B(C_6F_5)_4]$, R =	H (**Y1**)	Me (**Y2**)	Et (**Y3**)	iPr (**Y4**)
Wavelength (Å)	0.71073	0.71073	0.71073	0.71073
Crystal system	Monoclinic	Monoclinic	Monoclinic	Monoclinic
Space group	$P2_1$	$P2_1/c$	$P2_1/n$	$C2/c$
a (Å), α (°)	16.538(2), 90	14.599(10), 90	15.0163(5), 90	27.336(2), 90
b (Å), β (°)	14.4952(18), 90.053(2)	16.737(11), 90.253(11)	23.1163(8), 90.9020(10)	11.5772(10), 106.0490(10)
c (Å), γ (°)	22.753(3), 90	47.12(3), 90	16.7813(6), 90	19.4333(17), 90
V (Å^3)	5454.3(12)	11514(13)	5824.4(3)	5910.4(9)
Z	4	8	4	4
ρ_{calc} (g/cm^3)	1.504	1.457	1.472	1.482
Crystal size (mm^3)	0.274 × 0.221 × 0.194		0.492 × 0.224 × 0.138	0.327 × 0.268 × 0.140
θ range for data collection (°)	1.405 to 27.103	1.395 to 23.629	1.500 to 21.036	1.550 to 25.349
Index ranges	$-21 \leq h \leq 21$	$-16 \leq h \leq 16$	$-15 \leq h \leq 15$	$-32 \leq h \leq 32$
	$-18 \leq k \leq 18$	$-18 \leq k \leq 18$	$-23 \leq k \leq 23$	$-13 \leq k \leq 13$
	$-29 \leq l \leq 29$	$-52 \leq l \leq 52$	$-16 \leq l \leq 16$	$-23 \leq l \leq 23$
Reflections collected	70917	84123	43460	33243
Independent reflections (R_{int})	24026 (0.0696)	17198 (0.0538)	6283 (0.0425)	5416 (0.0464)
Completeness (%)	99.8	99.7	100.0	100.0
Data / restraints / parameters	24026 / 600 / 970	17198 / 1156 / 1810	6283 / 67 / 770	5416 / 324 / 599
Goodness-of-fit on F^2	1.123	1.046	1.053	1.032
R_1, wR_2 [$I > 2\sigma(I)$]	0.0821, 0.2161	0.0769, 0.1922	0.0638, 0.1591	0.0470, 0.1119
R_1, wR_2 (all data)	0.1146, 0.2386	0.0909, 0.2027	0.0795, 0.1719	0.0685, 0.1255

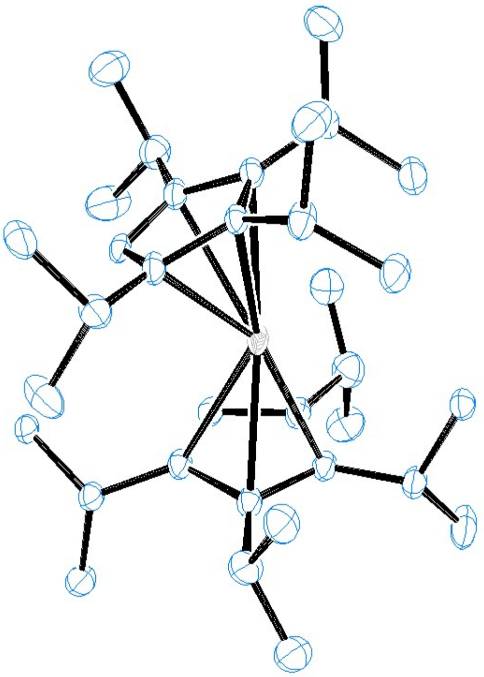

Figure S31. Solid-state structure of one of the $[Y(Cp^{iPr4H})_2]^+$ cations in **Y1** with thermal ellipsoids at the 50% probability level. Hyrdogen atoms and the disordered component are omitted for clarity

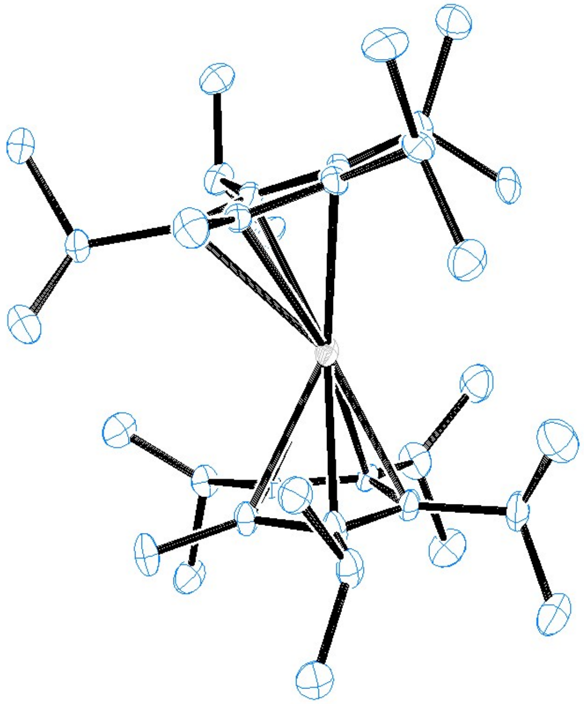

Figure S32. Solid-state structure of one of the $[Y(Cp^{iPr4Me})_2]^+$ cations in **Y2** with thermal ellipsoids at the 50% probability level. Hyrdogen atoms and the disordered component are omitted for clarity.

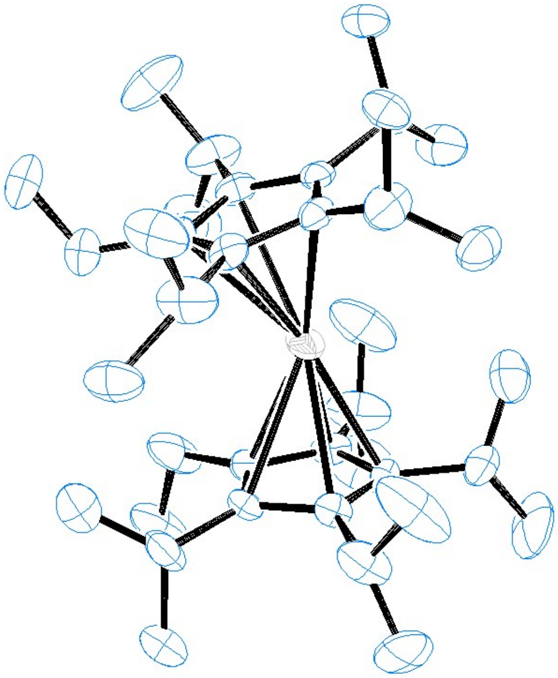

Figure S33. Solid-state structure of the $[Y(Cp^{iPr4Et})_2]^+$ cation in **Y3** with thermal ellipsoids at the 30% probability level.

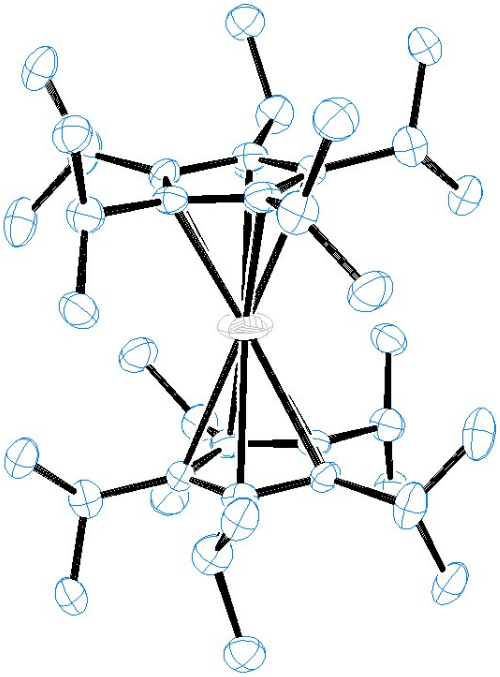

Figure S34. Solid-state structure of the $[Y(Cp^{iPr5})_2]^+$ cation in **Y4** with thermal ellipsoids at the 50% probability level. Hydrogen atoms are omitted for clarity.

Magnetic Measurements

General. Magnetic samples were prepared by adding crystalline powder (18.2 mg of **1**, 19.4 mg of **2**, 15.8 mg of **3**, and 17.7 mg of **4**) to a 5 mm i.d./7 mm o.d. quartz tube with a raised quartz platform. A layer of eicosane was added to the samples (21.1 mg for **1**, 21.7 mg for **2**, 15.9 mg for **3**, and 20.4 mg for **4**) to provide good thermal contact between the sample and the bath and to prevent crystallite torqueing. The tubes were fitted with Teflon sealable adapters, evacuated using a glovebox vacuum pump, and then flame sealed with an O_2/H_2 flame under vacuum. After flame-sealing, the eicosane was melted in a 40 °C water bath.

Magnetic susceptibility measurements were collected using a Quantum Design MPMS2 SQUID magnetometer. All data were corrected for diamagnetic contributions from the core diamagnetism and for the diamagnetism of the eicosane used to suspend the sample, estimated using Pascal's constants to give corrections of χ_{dia} = –0.000670 emu/mol, – 0.000694 emu/mol, – 0.000717 emu/mol, and –0.000741 emu/mol for **1**, **2**, **3**, and **4**, respectively.

Dc Magnetic Susceptibility Measurements. Dc magnetic susceptibility measurements were performed at temperatures ranging from 2 to 300 K under applied fields of 1, 5, and 10 kOe (0.1, 0.5, and 1 T) for **1**-**4**.

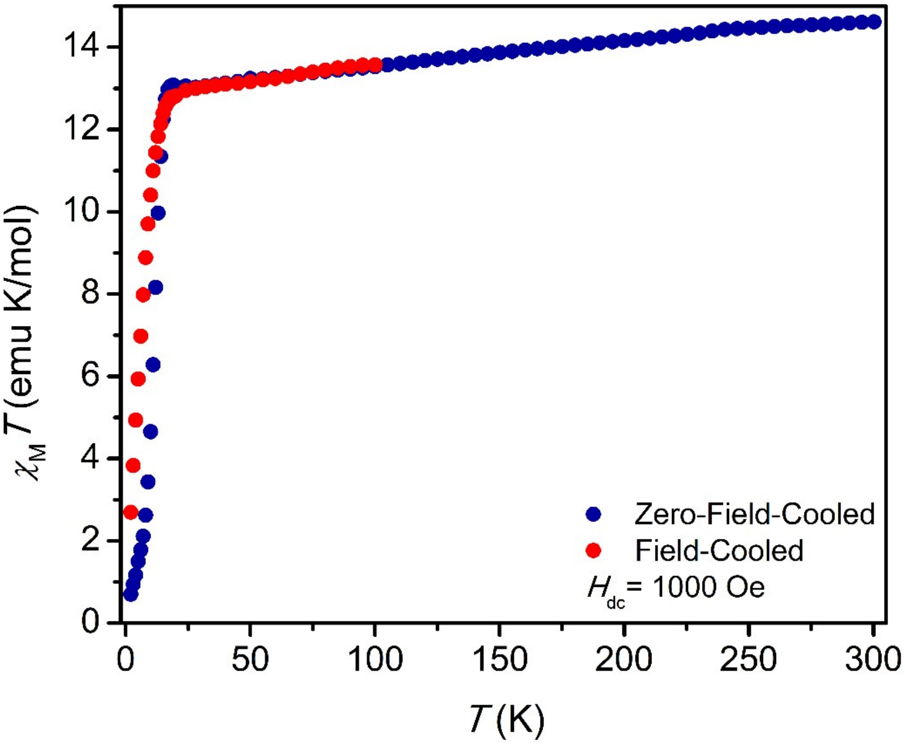

Figure S35. Field-cooled (red) and zero-field cooled (blue) measurements of **1** under an applied field of 1 kOe.

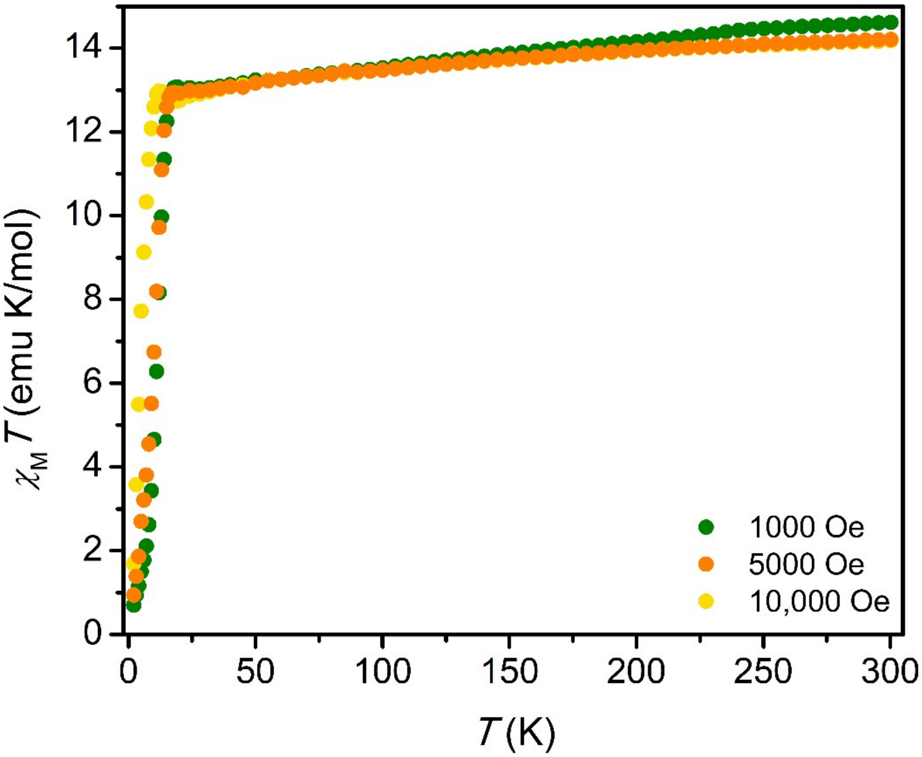

Figure S36. Zero-field cooled dc magnetic susceptibility measurements of **1** under applied fields of 1, 5, and 10 kOe.

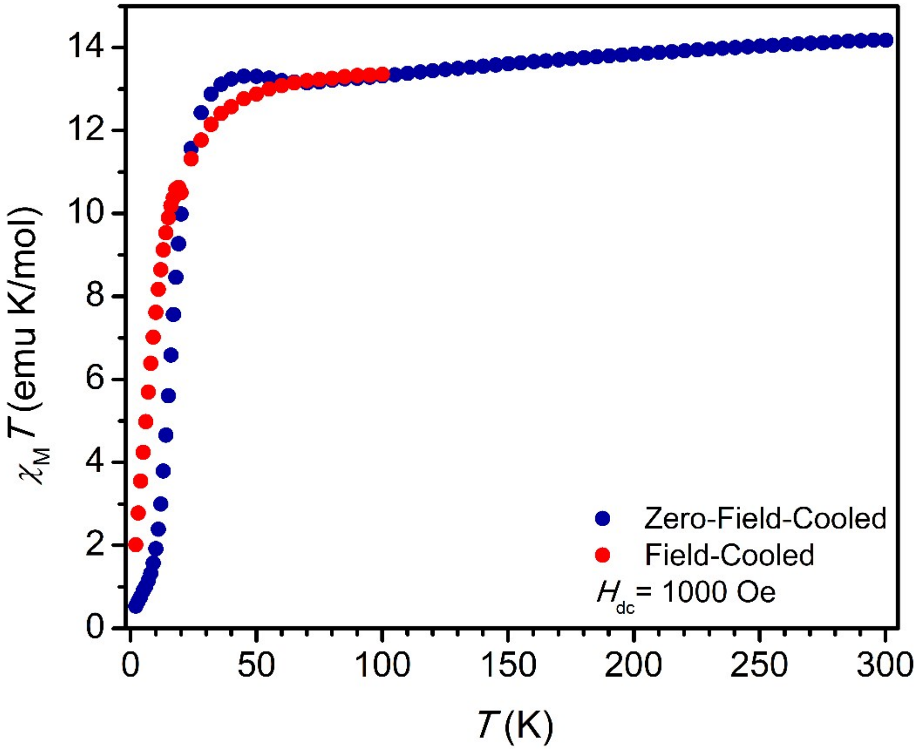

Figure S37. Field-cooled (red) and zero-field cooled (blue) measurements of **2** under an applied field of 1 kOe.

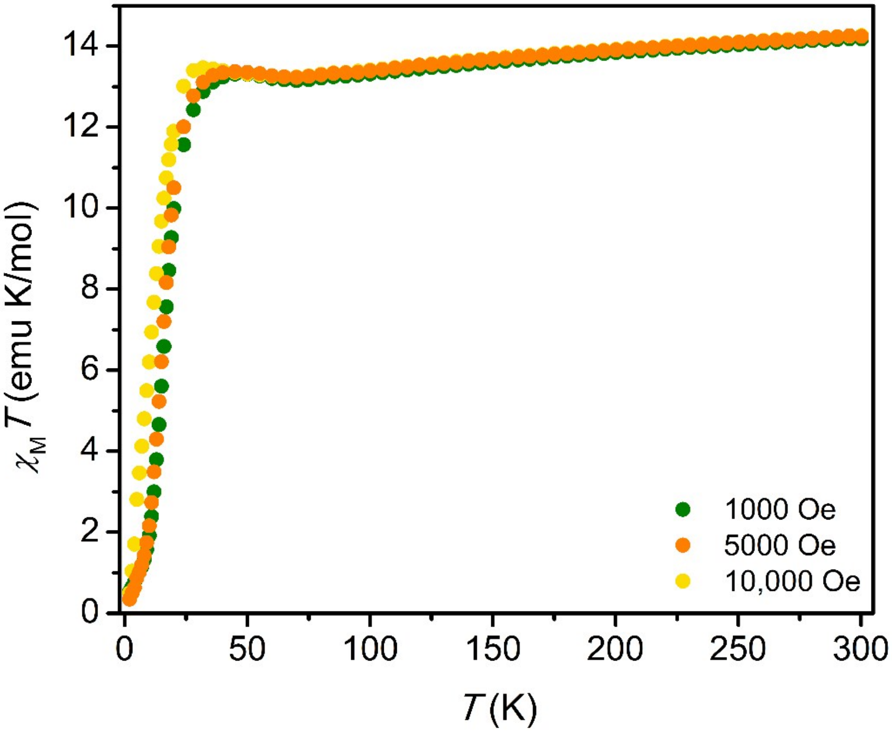

Figure S38. Zero-field cooled dc magnetic susceptibility measurements of **2** under applied fields of 1, 5, and 10 kOe.

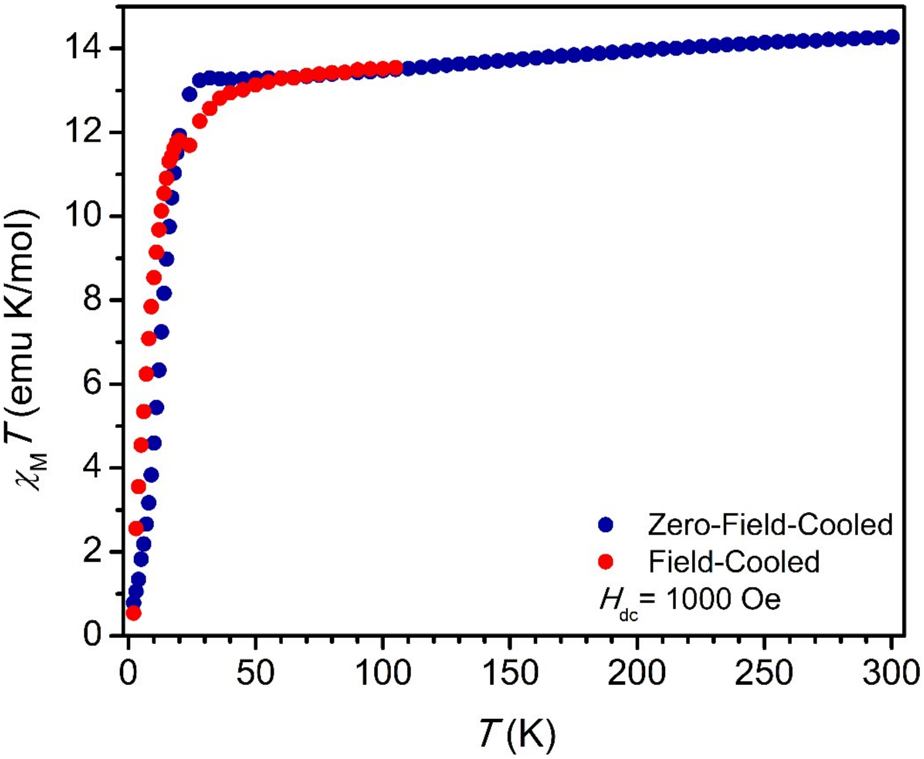

Figure S39. Field-cooled (red) and zero-field cooled (blue) measurements of **3** under an applied field of 1 kOe.

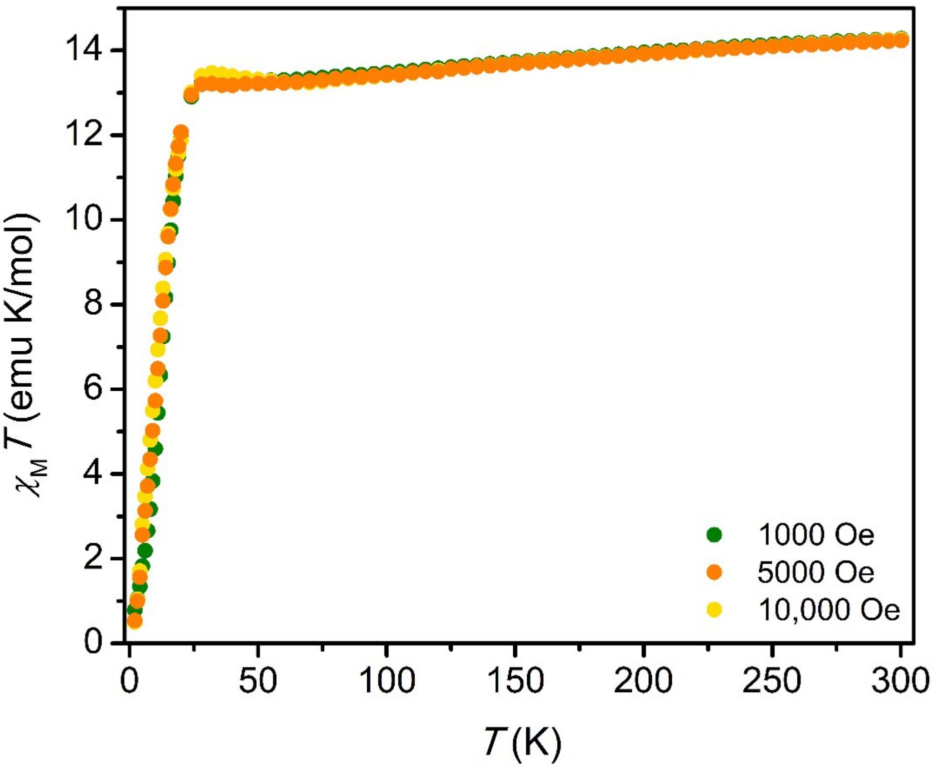

Figure S40. Zero-field cooled dc magnetic susceptibility measurements of **3** under applied fields of 1, 5, and 10 kOe.

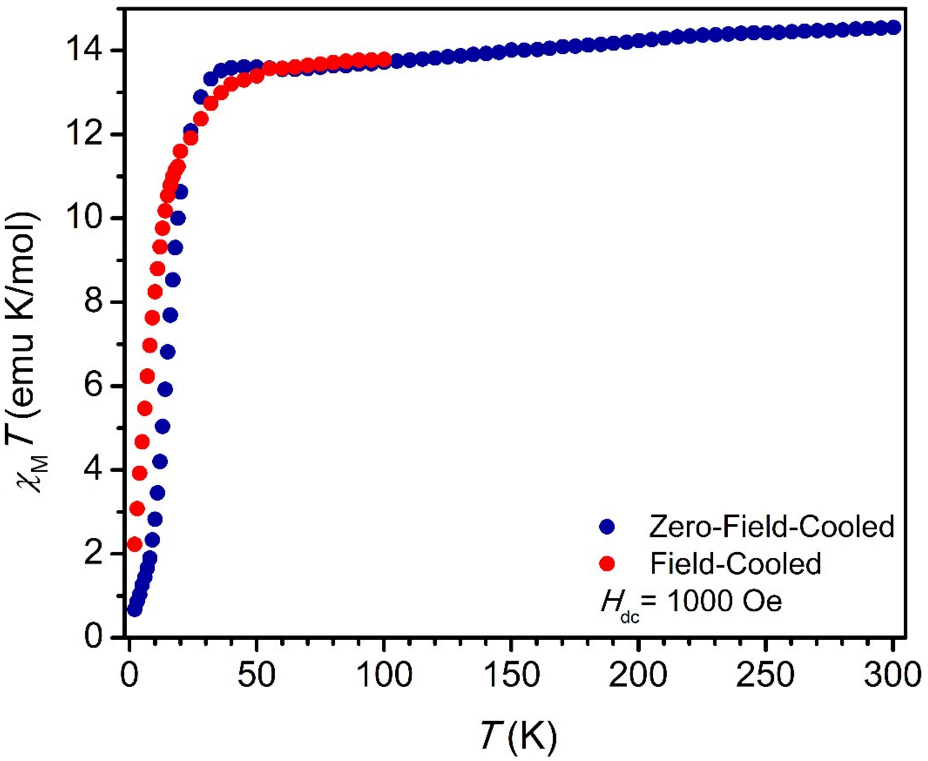

Figure S41. Field-cooled (red) and zero-field cooled (blue) measurements of **4** under an applied field of 1 kOe.

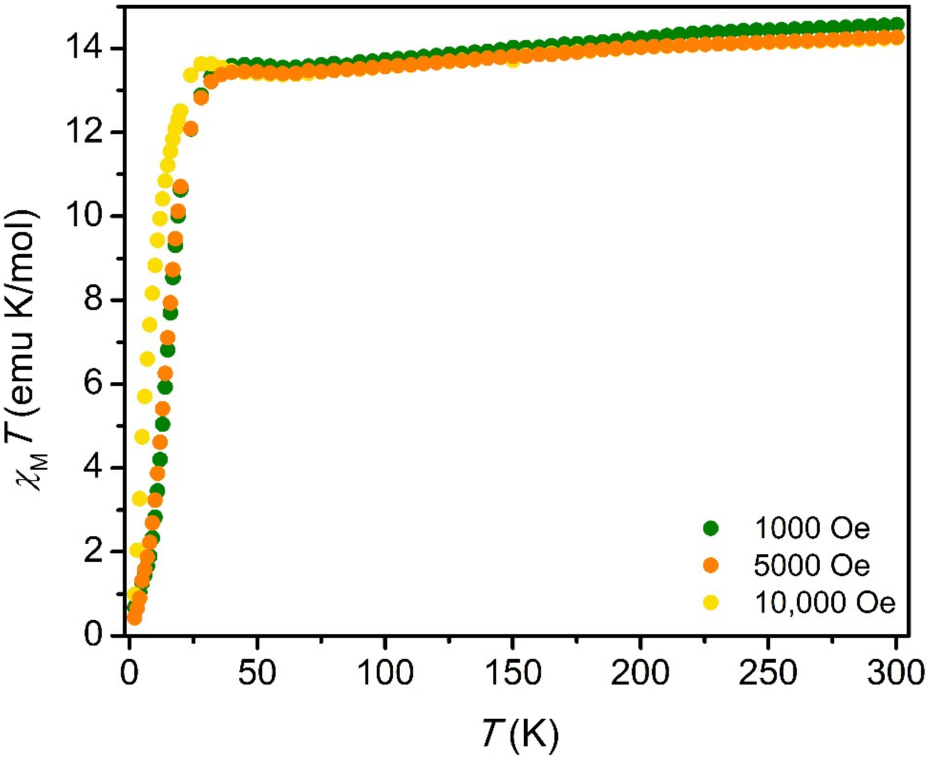

Figure S42. Zero-field cooled dc magnetic susceptibility measurements of **4** under applied fields of 1, 5, and 10 kOe.

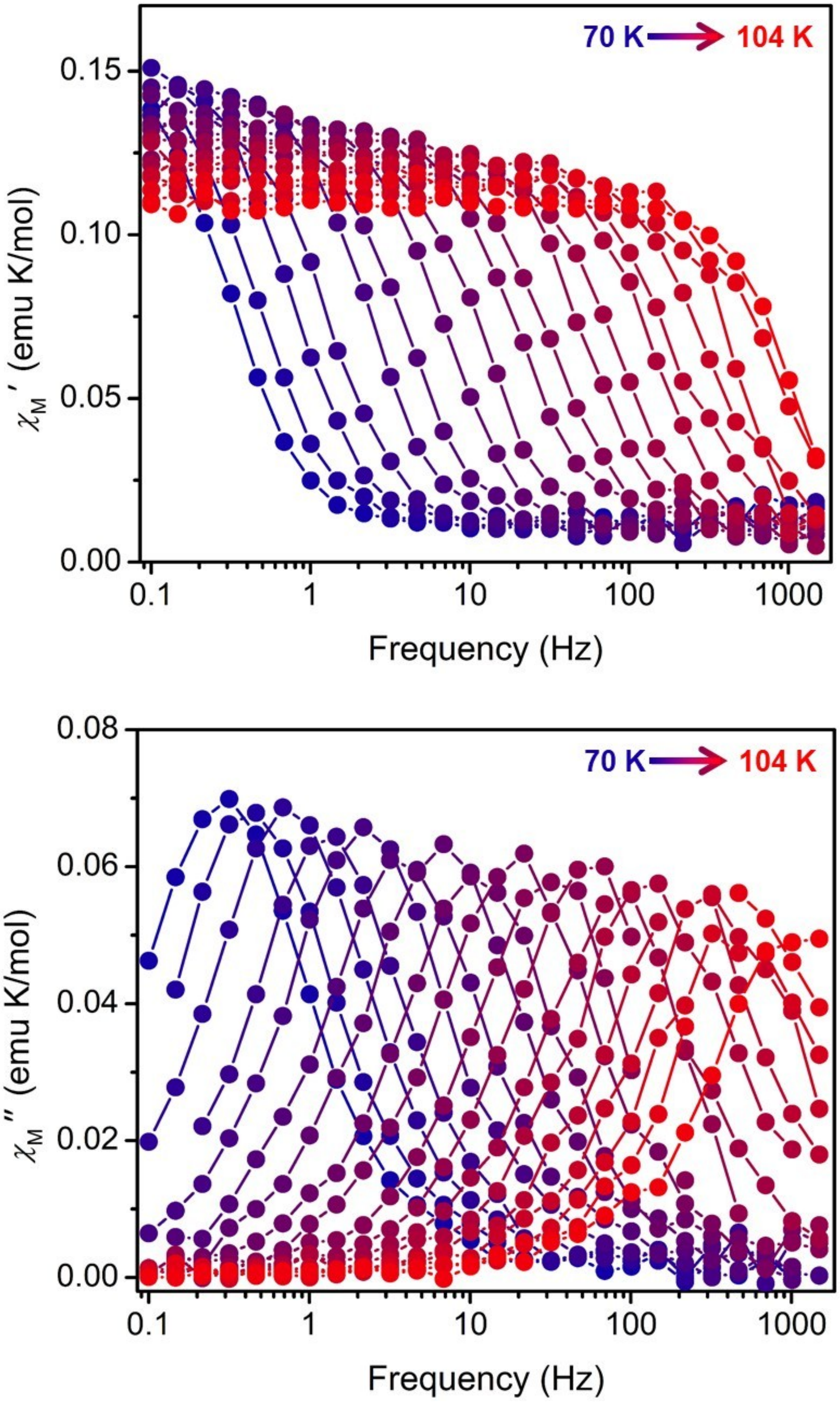

Figure S43. In-phase ($\chi_M{}'$, top) and out-of-phase ($\chi_M{}''$, bottom) components of the ac magnetic susceptibility for **1** under zero applied dc field at frequencies ranging from 0.1–1500 Hz and temperatures from 70–104 K (2 K steps). The colored lines are guides for the eye.

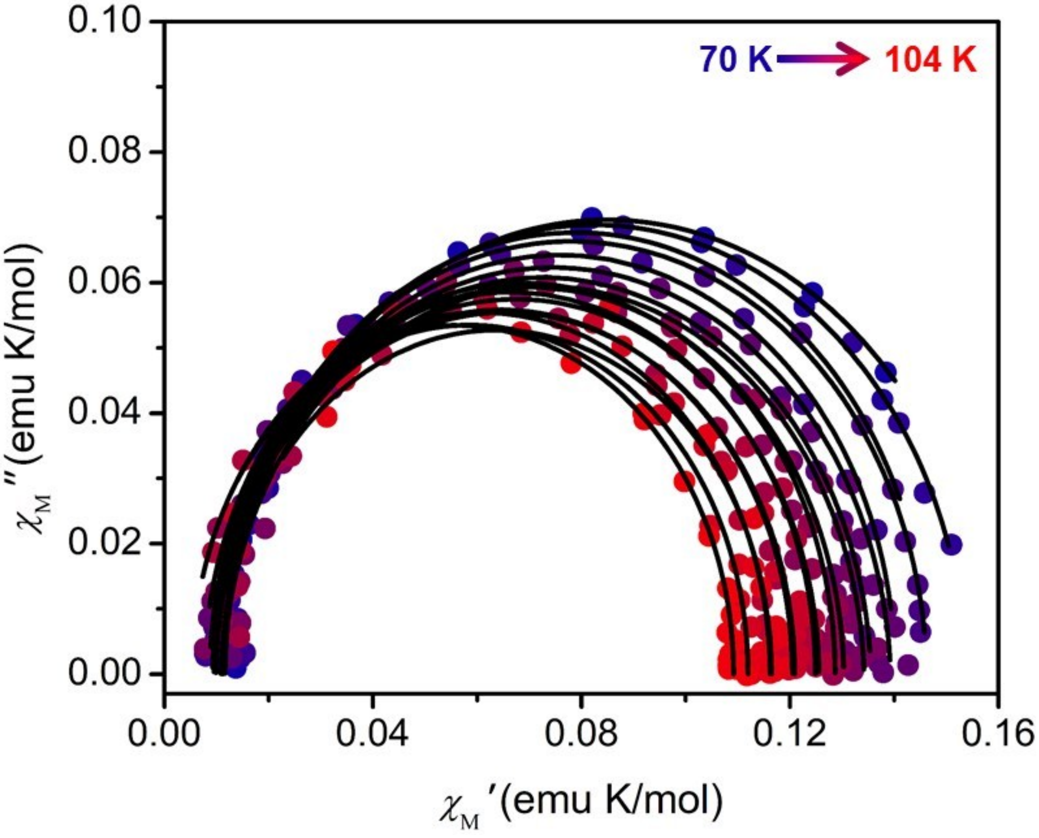

Figure S44. Cole-Cole plots for **1** from 70–104 K (2 K steps). The black lines represent fits to the data using a generalized Debye model, which were used to extract τ values at each temperature.

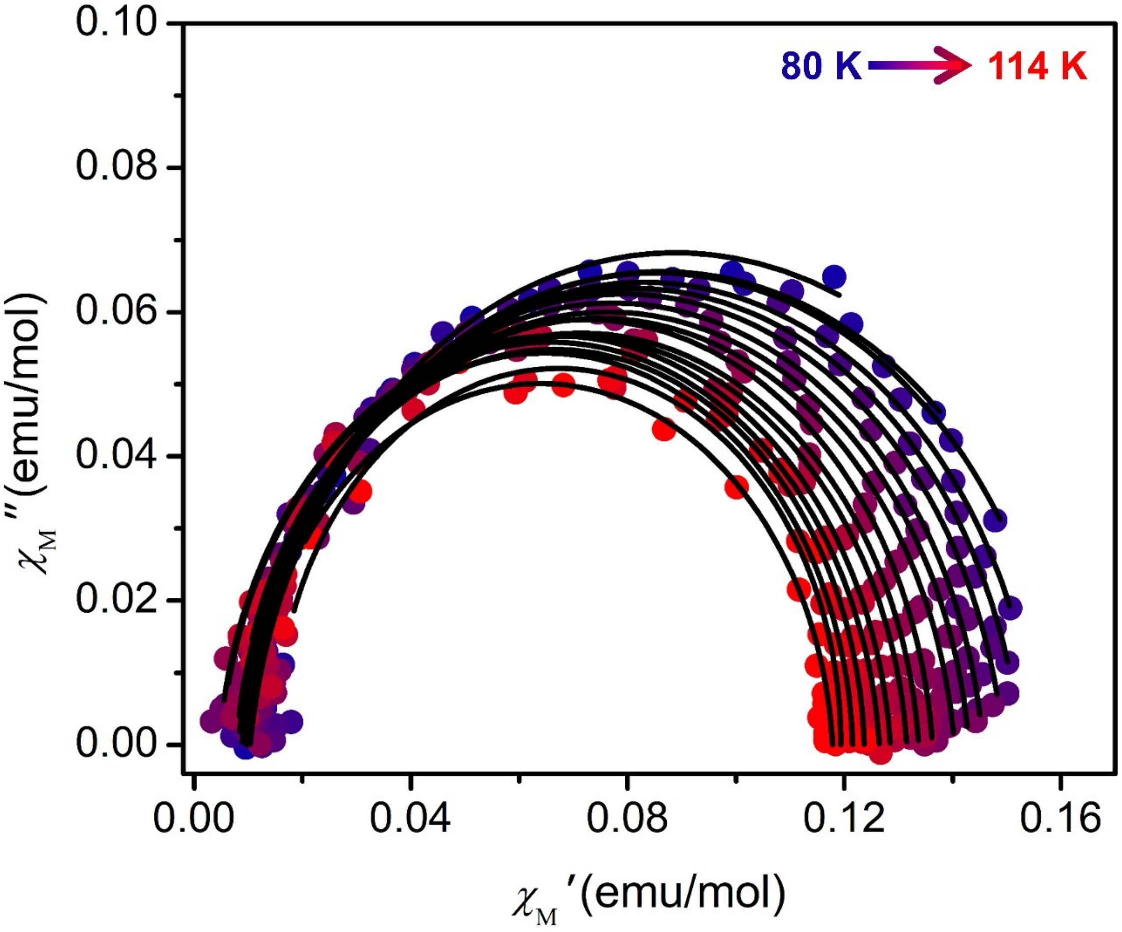

Figure S45. Cole-Cole plots for **2** from 80 to 114 K (2 K steps). The black lines represent fits to the data using a generalized Debye model, which were used to extract τ values at each temperature.

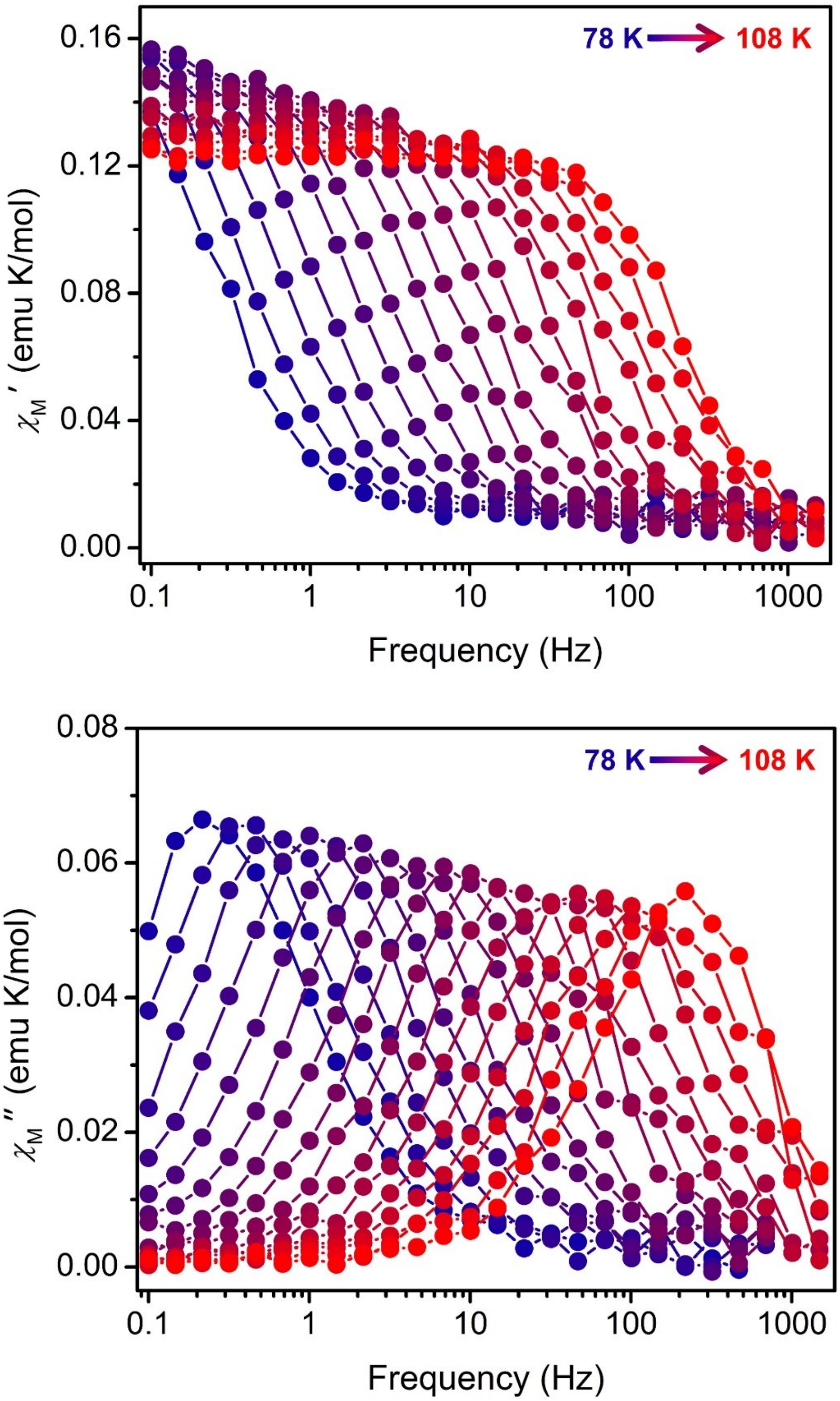

Figure S46. In-phase (χ_M', top) and out-of-phase (χ_M'', bottom) components of the ac magnetic susceptibility for **3** under zero applied dc field at frequencies ranging from 0.1–1500 Hz and temperatures from 78–108 K (2 K steps). The colored lines are guides for the eye.

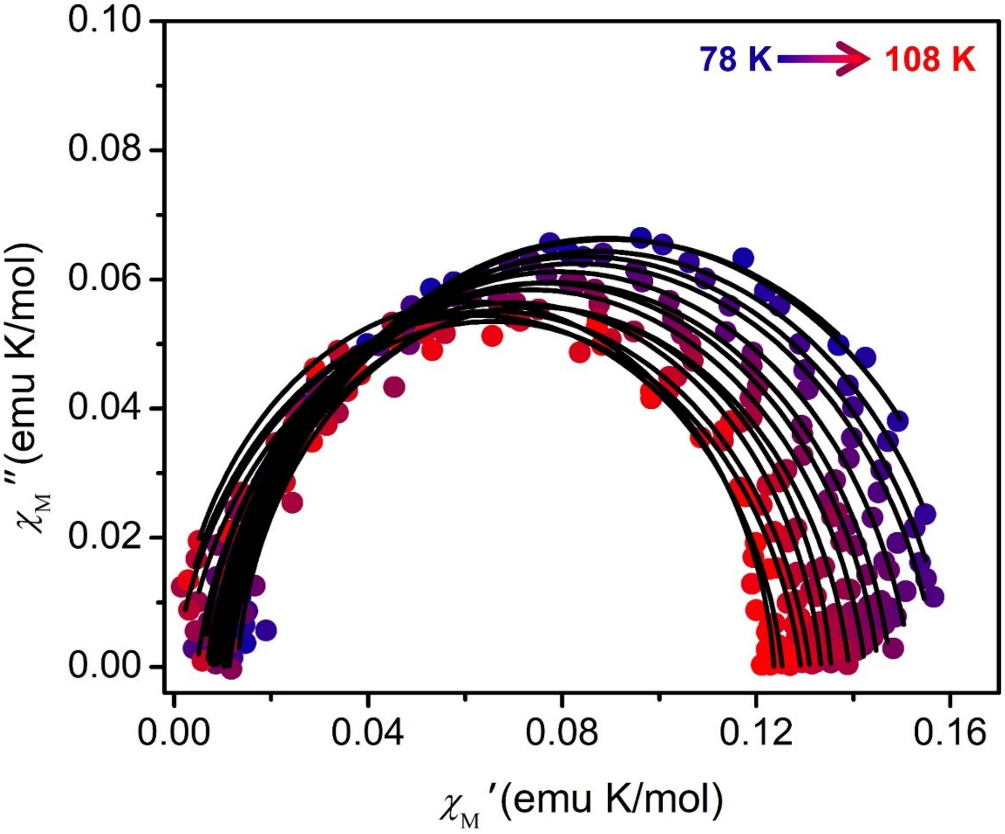

Figure S47. Cole-Cole plots for **3** from 78 to 108 K (2 K steps). The black lines represent fits to the data using a generalized Debye model, which were used to extract τ values for at each temperature.

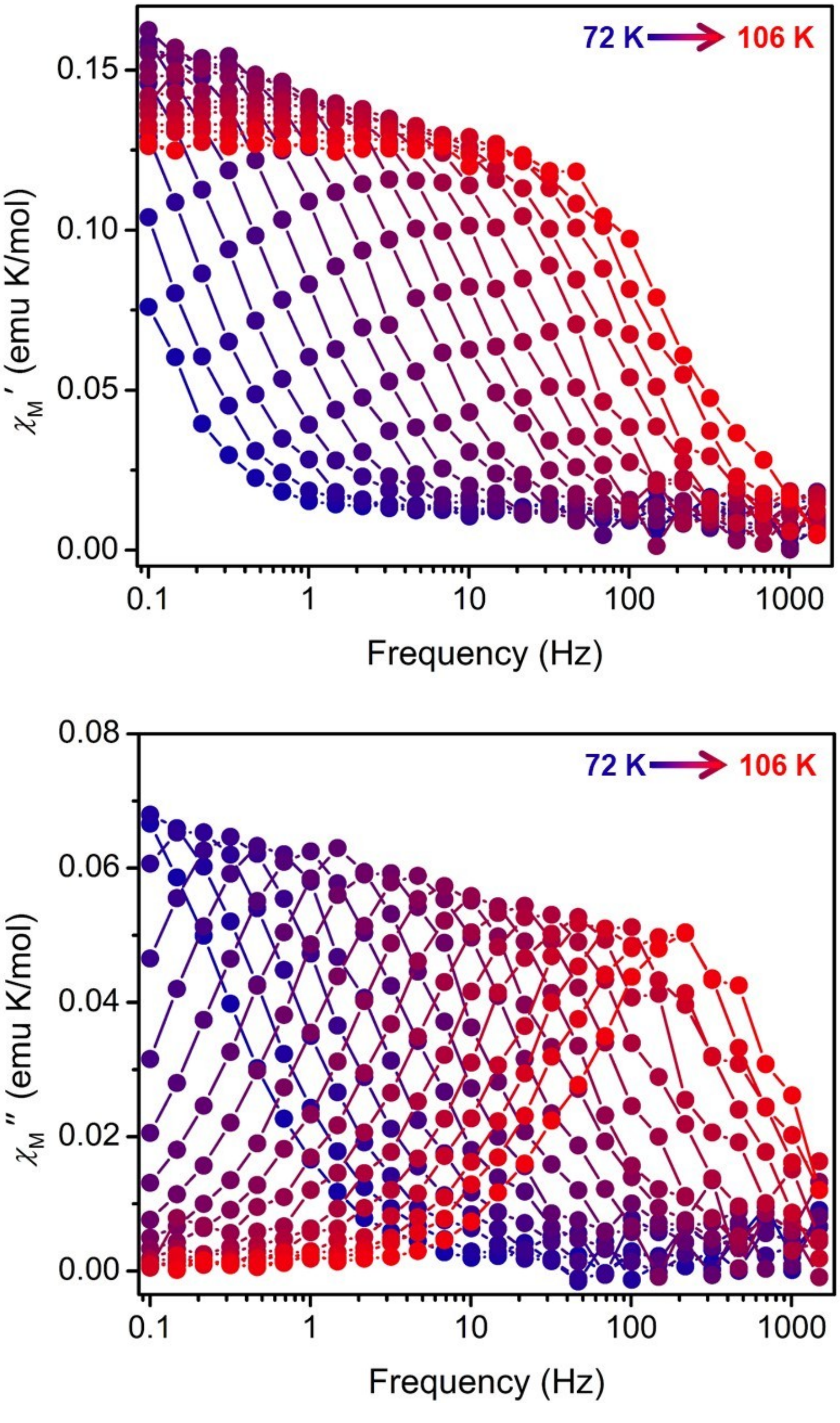

Figure S48. In-phase ($\chi_M{}'$, top) and out-of-phase ($\chi_M{}''$, bottom) components of the ac magnetic susceptibility for **4** under zero applied dc field at frequencies ranging from 0.1–1500 Hz and temperatures from 72–106 K (2 K steps). The colored lines are guides for the eye.

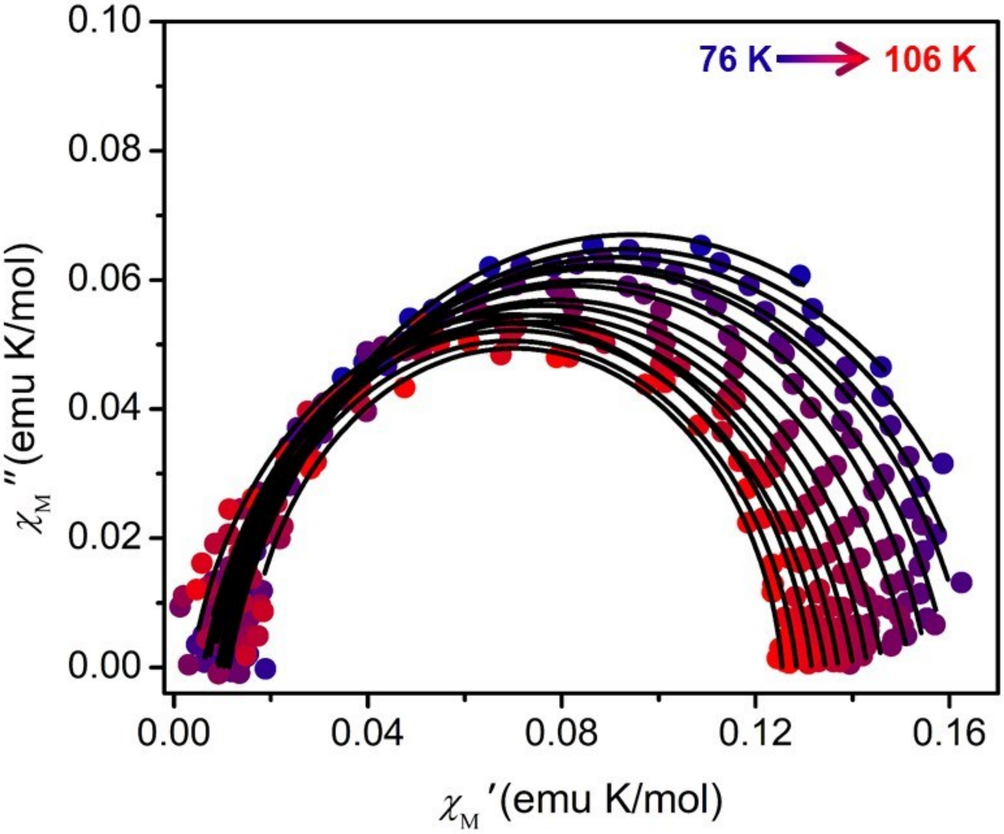

Figure S49. Cole-Cole plots for **4** from 76 to 106 K (2 K steps). The black lines represent fits to the data using a generalized Debye model, which were used to extract τ values at each temperature.

Dc Magnetic Relaxation Measurements. Dc magnetic relaxation measurements were collected by magnetizing a sample under an applied field of 5 T, allowing 5 minutes for equilibration, and then subsequently returning the field to 0 Oe (no overshoot, hi-res disabled) and measuring the magnetization at periodic time intervals. Dc magnetic relaxation data were fit to a stretched exponential function according to the equation:

$$M(t) = M_1 + (M_0 - M_1)^{(t/\tau)^n}$$

where $M(t)$ is the magnetization at time t, M_0 is the initial magnetization measured after the field has been removed, M_1 is the final value of the magnetization at $t = \infty$, τ is the magnetic relaxation time, and n is a free variable. Though M_1 should equal zero at zero field, we found non-zero values for all dc magnetic relaxation measurements, likely due to a small remnant field in the superconducting magnet. We therefore set M_1 equal to the value of the magnetization measured at the last time point of each experiment. At high temperatures, it was possible to measure the full decay of the magnetization within 1000 s. At lower temperatures where magnetic relaxation slowed, experiments were conducted for 5000 s. Even this length of time was not sufficient to observe the full decay of the magnetization for measurements of **2**-**4** at the lowest temperatures measured (2 to 20 K), however, and therefore setting M_1 equal to the last value of the magnetization measured for these experiments represented an overestimate. Better fits to the data for these experiments were obtained by treating M_1 as a free variable (M_1 values marked with an * in the tables below).

In order to test the validity of this strategy, fits to higher temperature experiments with M_1 as a free variable were obtained and compared to previous fits. This resulted in values of τ within 5% of those obtained for fits with M_1 equal to the last value of the magnetization measured in the experiment. Furthermore, the values obtained for τ with M_1 as a free variable were consistently lower than those obtained with M_1 equal to the last value of the magnetization, demonstrating that this alternative fitting strategy did not overestimate the value of τ at low temperatures.

Table S3. Parameters used to fit dc magnetic relaxation data for **1** and magnetic relaxation times extracted from these fits.

T (K)	M_0 (μ_b)	M_1 (μ_b)	n	τ (s)[a]
2	2.45604	0.02609	0.752	438.568
6	1.39036	0.00443	0.829	223.137
10	0.80538	0.00254	0.837	169.852
16	0.23694	0.00226	0.849	104.229
18	0.10969	0.00105	0.849	96.437
20	0.07967	0.00089	0.849	83.856
22	0.03968	0.00047	0.863	74.993
24	0.01524	0.00048	0.853	71.354
26	0.00680	0.00035	0.911	67.146
28	0.00404	0.00033	0.876	56.561
30	0.00215	0.00019	0.856	53.881

[a] Values for τ are likely only accurate to three significant figures. The full value extracted from the fit is reported for reproducibility.

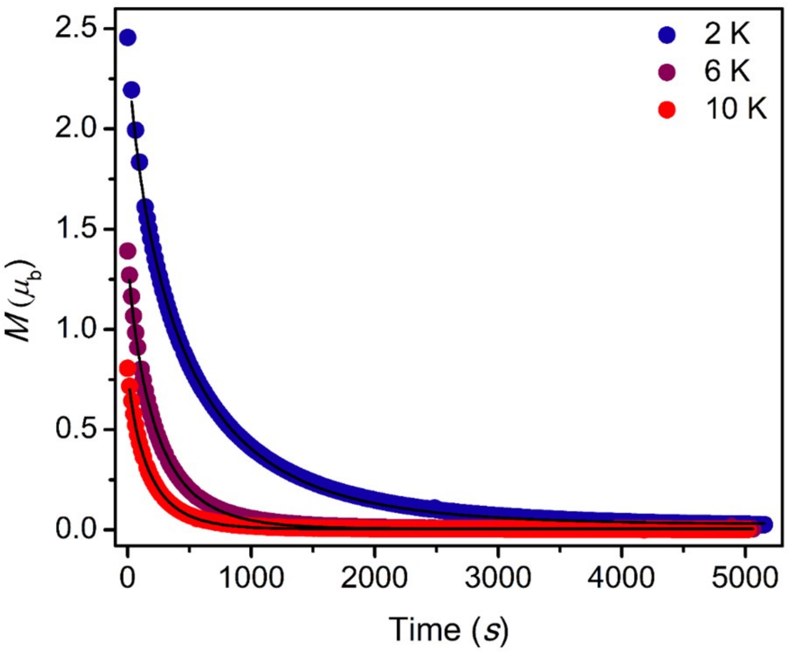

Figure S50. Dc magnetic relaxation data for **1** collected at 2, 6, and 10 K. Black lines represent the fits to the data using stretched exponential functions, which were used to extract τ.

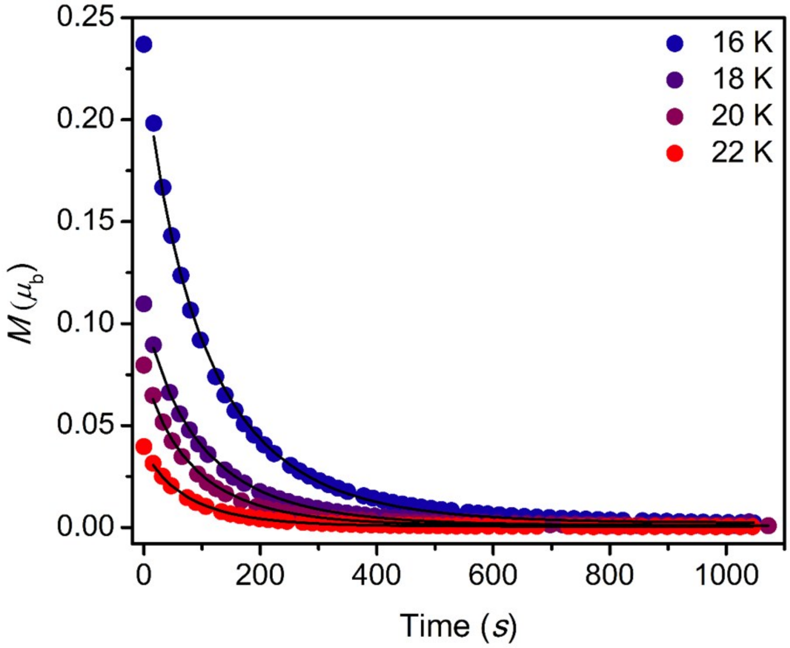

Figure S51. Dc magnetic relaxation data for **1** collected from 16 to 22 K in 2 K increments. Black lines represent the fits to the data using stretched exponential functions, which were used to extract τ.

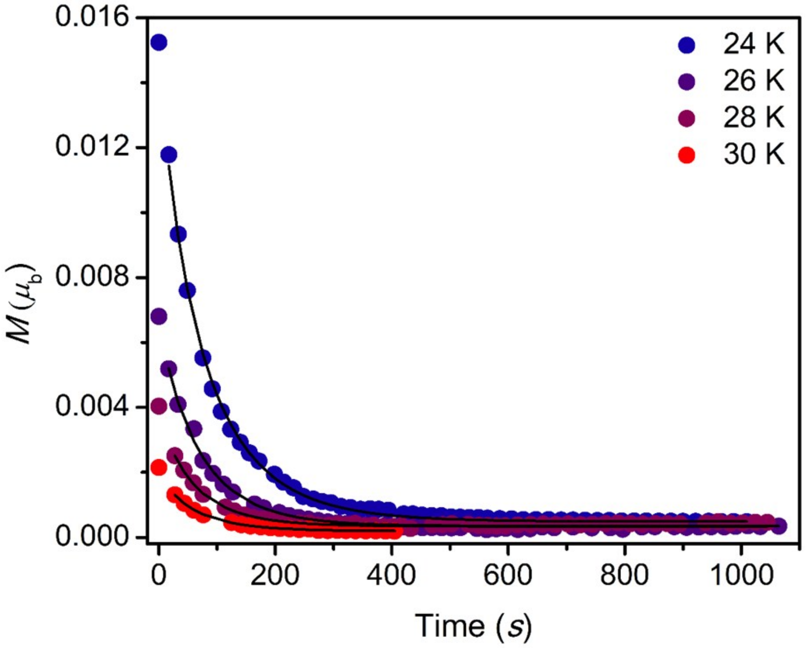

Figure S52. Dc magnetic relaxation data for **1** collected from 24 to 30 K in 2 K increments. Black lines represent the fits to the data using stretched exponential functions, which were used to extract τ.

Table S4. Parameters used to fit dc magnetic relaxation data for **2** and magnetic relaxation times extracted from these fits.

T (K)	M_0 (μ_b)	M_1 (μ_b)	n	τ (s)[a]
2	3.75127	0.22840*	0.671	2452.358
5	3.61807	0.21921*	0.676	2306.767
10	3.10026	0.19942*	0.728	1704.762
15	2.38810	0.11536*	0.725	1068.648
20	1.60054	0.04329*	0.742	797.784
25	1.07252	0.01302	0.760	607.850
30	0.77699	0.00275	0.771	451.321
35	0.48148	0.00071	0.824	374.604
40	0.32082	0.00051	0.866	299.806
45	0.23461	0.00028	0.886	232.751
50	0.16549	0.00041	0.906	185.239
52	0.13876	0.00122	0.929	167.607
54	0.11272	0.00067	0.930	154.968
56	0.09686	0.00052	0.948	141.881
58	0.07988	0.00033	0.940	129.358
60	0.05953	0.00017	0.939	116.581
62	0.04424	0.00020	0.951	102.367
64	0.02985	0.00011	0.958	87.195

*M_1 values obtained by treating M_1 as a free variable

[a] Values for τ are likely only accurate to three significant figures. The full value extracted from the fit is reported for reproducibility.

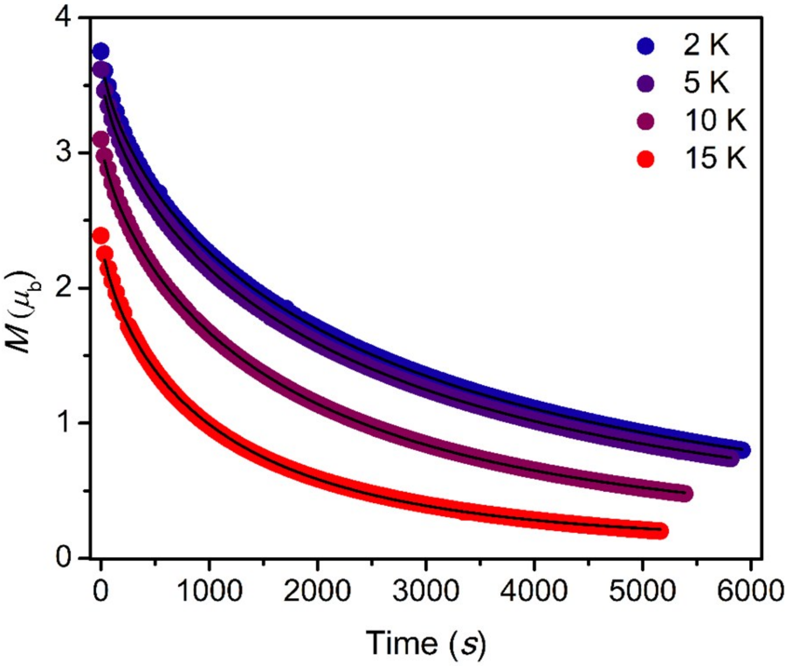

Figure S53. Dc magnetic relaxation data for **2** collected at 2, 5, 10, and 15 K. Black lines represent the fits to the data using stretched exponential functions, which were used to extract τ.

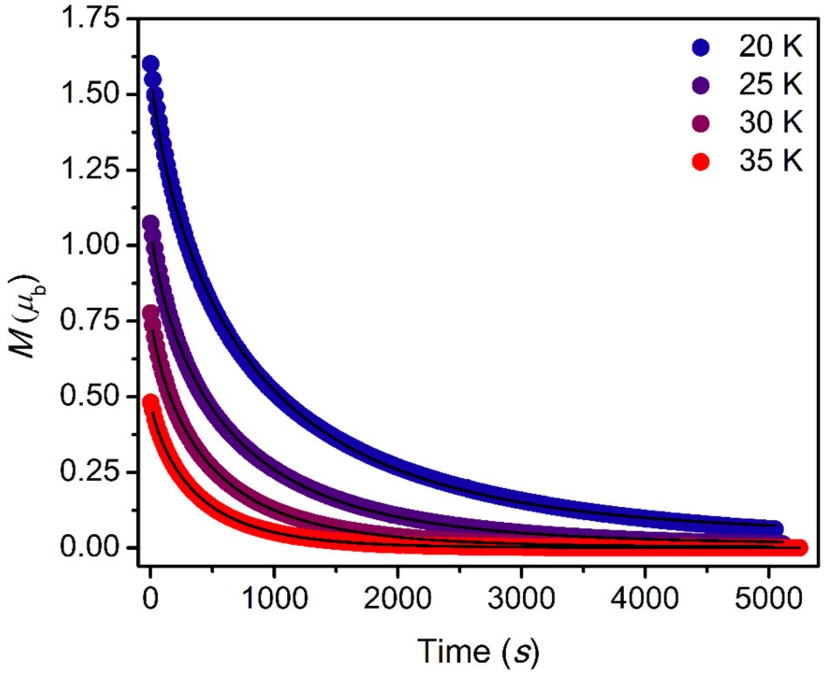

Figure S54. Dc magnetic relaxation data for **2** collected at 20, 25, 30, and 35 K. Black lines represent the fits to the data using stretched exponential functions, which were used to extract τ.

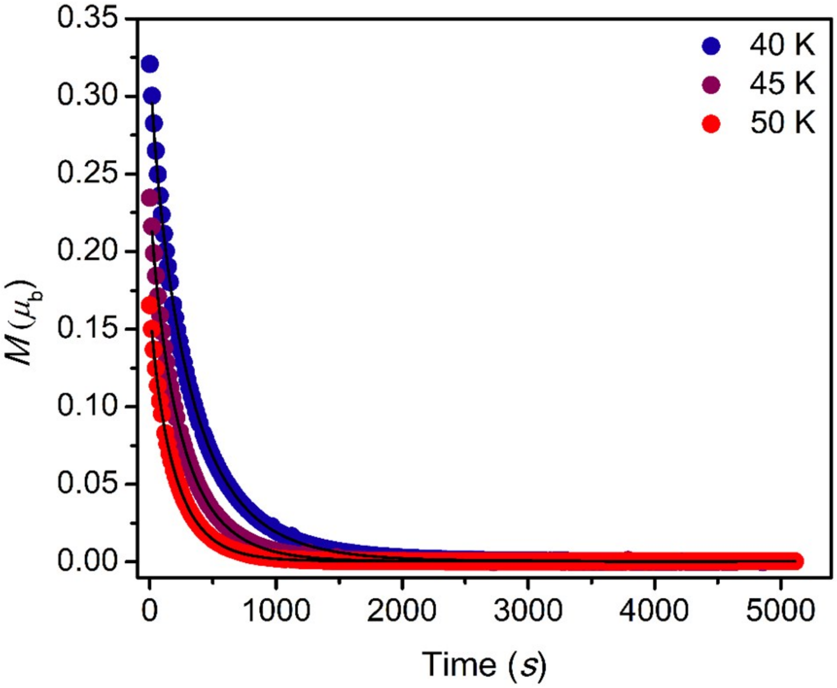

Figure S55. Dc magnetic relaxation data for **2** collected at 40, 45, and 50 K. Black lines represent the fits to the data using stretched exponential functions, which were used to extract τ.

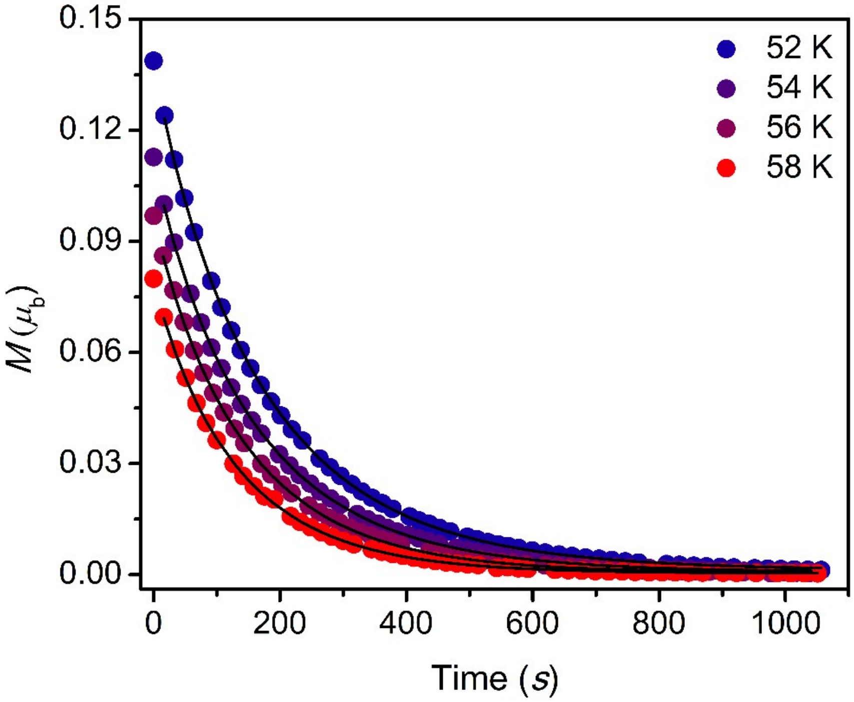

Figure S56. Dc magnetic relaxation data for **2** collected in 2 K intervals from 52 to 58 K. Black lines represent the fits to the data using stretched exponential functions, which were used to extract τ.

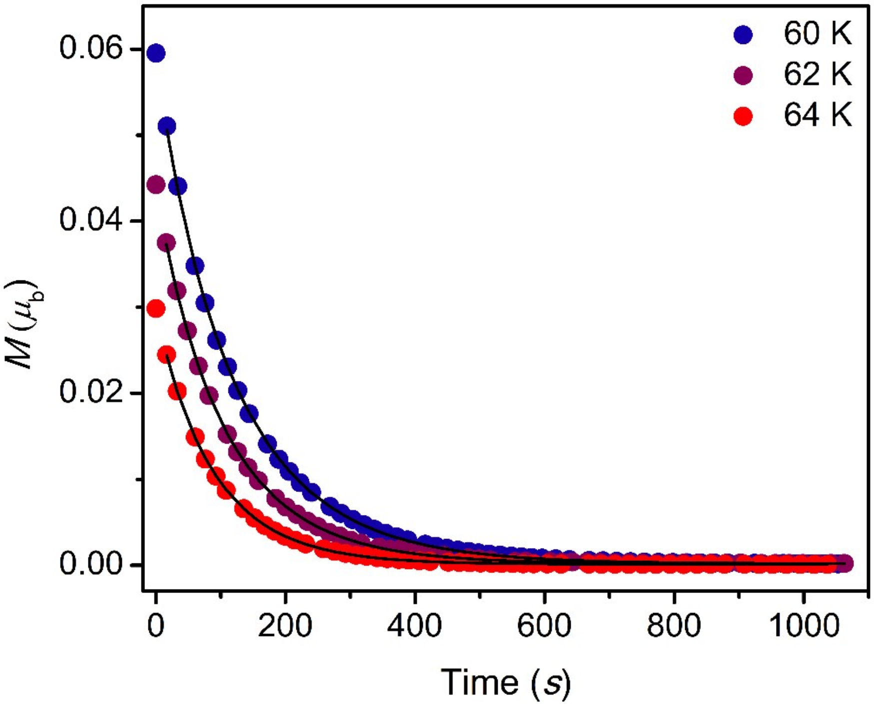

Figure S57. Dc magnetic relaxation data for **2** collected at 60, 62, and 64 K. Black lines represent the fits to the data using stretched exponential functions, which were used to extract τ.

Table S5. Parameters used to fit dc magnetic relaxation data for **3** and magnetic relaxation times extracted from these fits.

T (K)	M_0 (μ_b)	M_1 (μ_b)	n	τ (s)[a]
2	2.59342	0.14798*	0.664	447.490
5	2.34614	0.14711*	0.676	423.118
10	N/A	N/A	N/A	N/A
15	N/A	N/A	N/A	N/A
20	N/A	N/A	N/A	N/A
25	0.43968	0.00908	0.587	328.903
30	0.27154	0.00302	0.632	308.801
35	0.17141	0.00162	0.669	266.721
40	0.11374	0.00138	0.718	223.622
45	0.06901	0.00127	0.752	189.312
50	0.04321	0.00083	0.817	152.663
52	0.03637	0.00052	0.818	140.186
54	0.02747	0.00044	0.838	132.555
56	0.02122	0.00032	0.849	119.390
58	0.01664	0.00028	0.869	108.162
60	0.01138	0.00027	0.897	91.467
62	0.00683	0.00021	0.898	74.450

*M_1 values obtained by treating M_1 as a free variable

[a] Values for τ are likely only accurate to three significant figures. The full value extracted from the fit is reported for reproducibility.

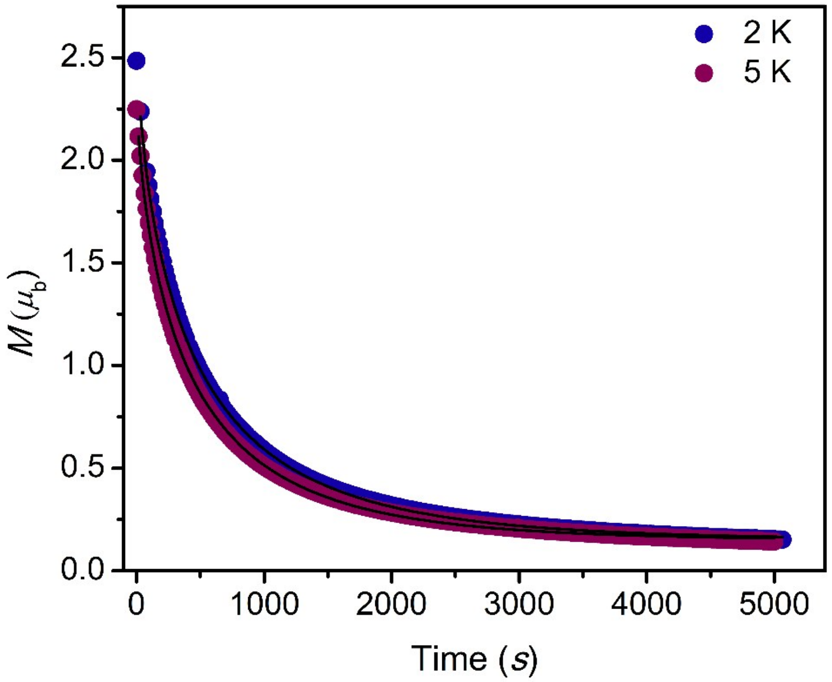

Figure S58. Dc magnetic relaxation data for **3** collected at 2 and 5 K. Black lines represent fits to the data using stretched exponential functions, which were used to extract τ.

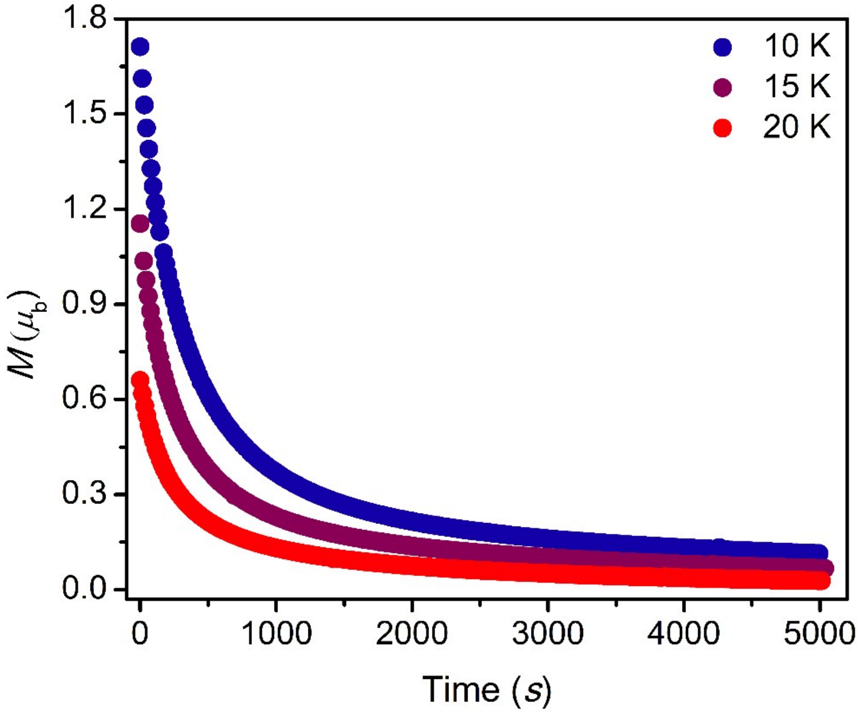

Figure S59. Dc magnetic relaxation data for **3** collected at 10, 15, and 20 K. These data could not be fit with a single stretched exponential function, indicating more complex relaxation dynamics.

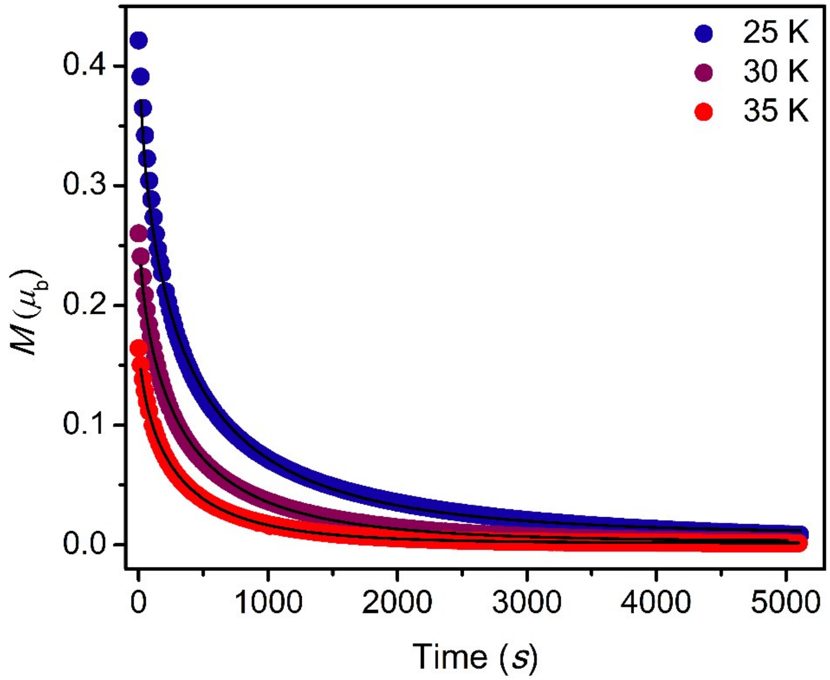

Figure S60. Dc magnetic relaxation data for **3** collected at 25, 30, and 35 K. Black lines represent the fits to the data using stretched exponential functions, which were used to extract *τ*.

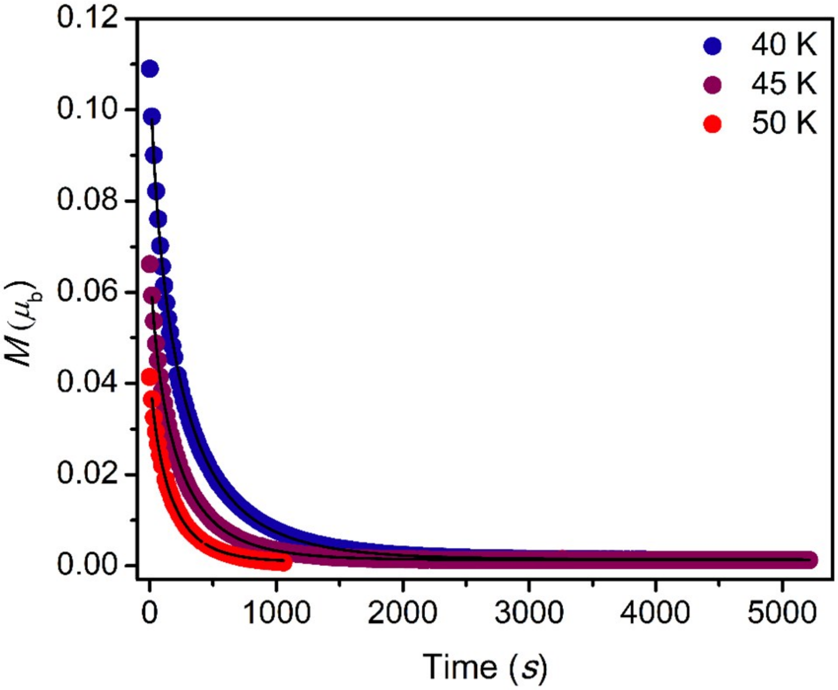

Figure S61. Dc magnetic relaxation data for **3** collected at 40, 45, and 50 K. Black lines represent the fits to the data using stretched exponential functions, which were used to extract *τ*.

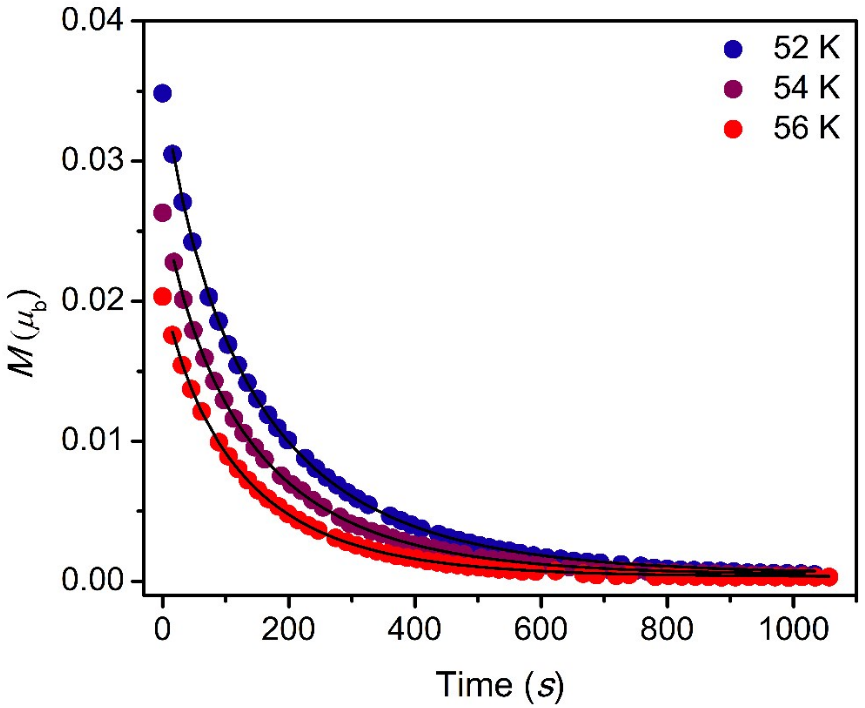

Figure S62. Dc magnetic relaxation data for **3** collected at 52, 54, and 56 K. Black lines represent the fits to the data using stretched exponential functions, which were used to extract τ.

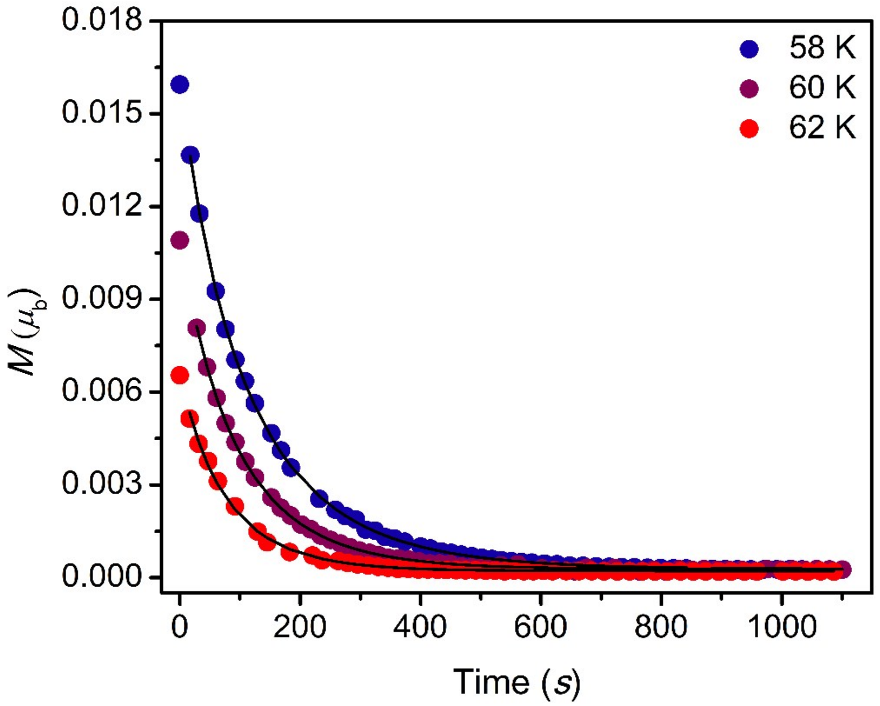

Figure S63. Dc magnetic relaxation data for **3** collected at 58, 60, and 62 K. Black lines represent the fits to the data using stretched exponential functions, which were used to extract τ.

Table S6. Parameters used to fit dc magnetic relaxation data for **4** and magnetic relaxation times extracted from these fits.

T (K)	M_0 (μ_b)	M_1 (μ_b)	n	τ (s)[a]
2	3.17947	0.24655*	0.762	1187.059
5	3.09335	0.18415*	0.696	1025.284
10	2.59245	0.15460*	0.708	878.518
15	1.83666	0.09682*	0.744	727.914
20	1.35344	0.03597	0.723	555.310
25	0.82875	0.00864	0.741	473.395
30	0.53401	0.00236	0.768	370.804
35	0.34532	0.00091	0.798	287.871
40	0.23441	0.00046	0.827	219.949
45	0.14824	0.00052	0.848	171.412
50	0.08026	0.00074	0.885	135.280
52	0.06197	0.00047	0.889	124.468
54	0.04687	0.00035	0.890	112.300
56	0.03473	0.00030	0.890	100.088
58	0.02284	0.00019	0.882	88.474
60	0.01388	0.00016	0.872	75.756
62	0.00792	0.00014	0.878	63.884

*M_1 values obtained by treating M_1 as a free variable

[a] Values for τ are likely only accurate to three significant figures. The full value extracted from the fit is reported for reproducibility.

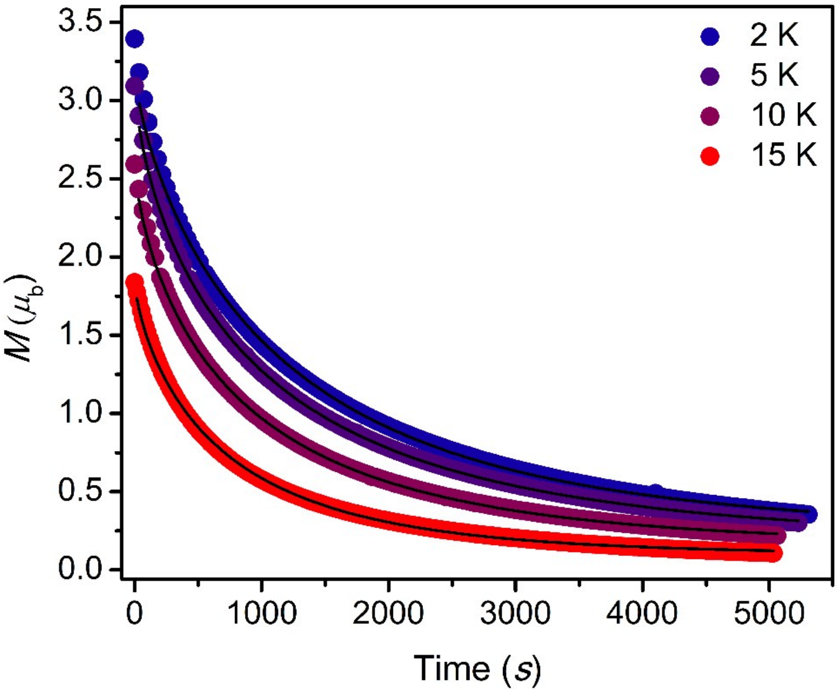

Figure S64. Dc magnetic relaxation data for **4** collected at 2, 5, 10, and 15 K. Black lines represent the fits to the data using stretched exponential functions, which were used to extract τ.

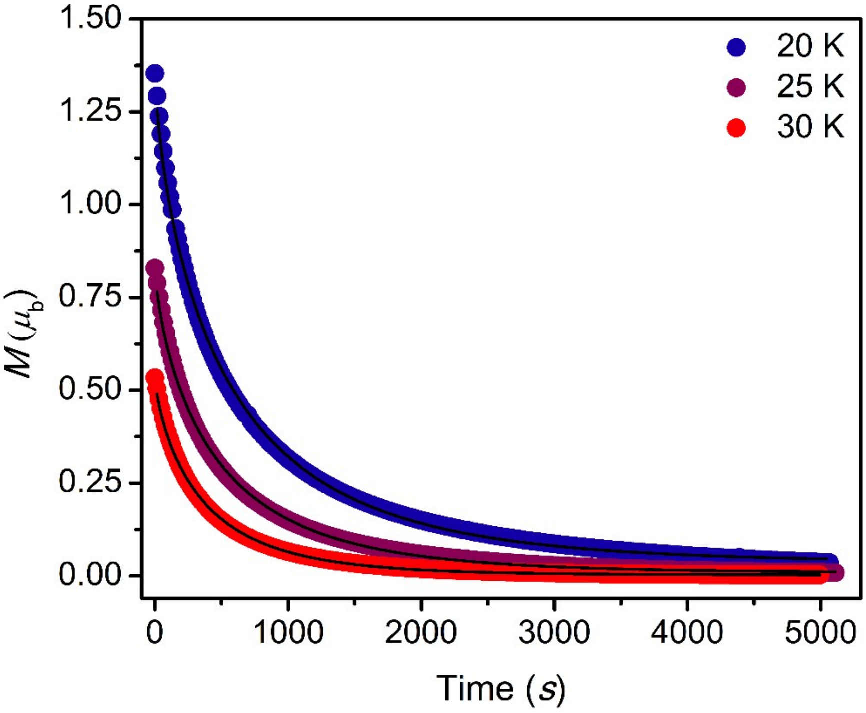

Figure S65. Dc magnetic relaxation data for **4** collected at 20, 25, and 30 K. Black lines represent the fits to the data using stretched exponential functions, which were used to extract τ.

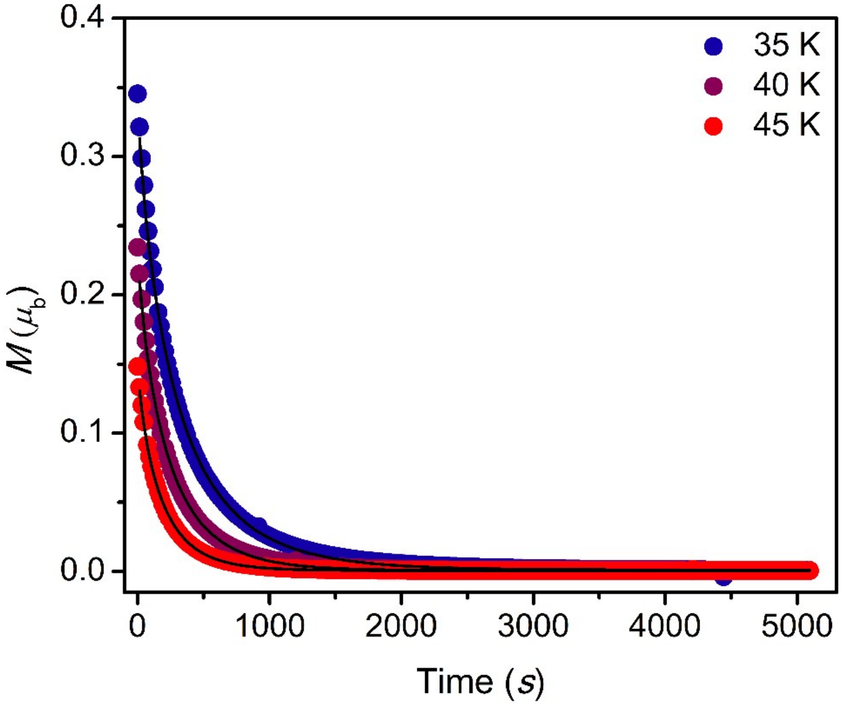

Figure S66. Dc magnetic relaxation data for **4** collected at 35, 40, and 45 K. Black lines represent the fits to the data using stretched exponential functions, which were used to extract τ.

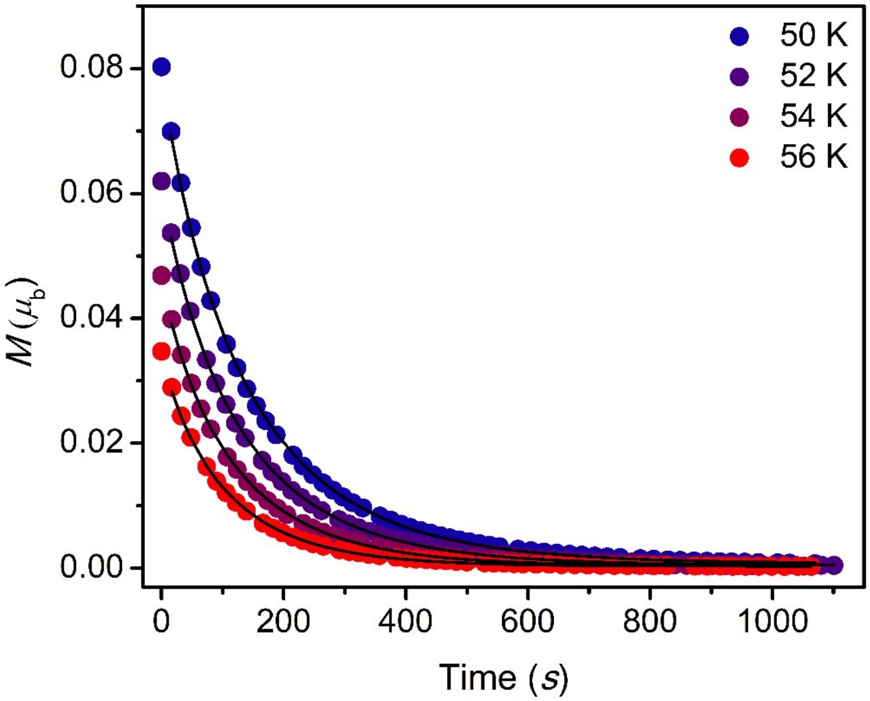

Figure S67. Dc magnetic relaxation data for **4** collected in 2 K intervals from 50 to 56 K. Black lines represent the fits to the data using stretched exponential functions, which were used to extract τ.

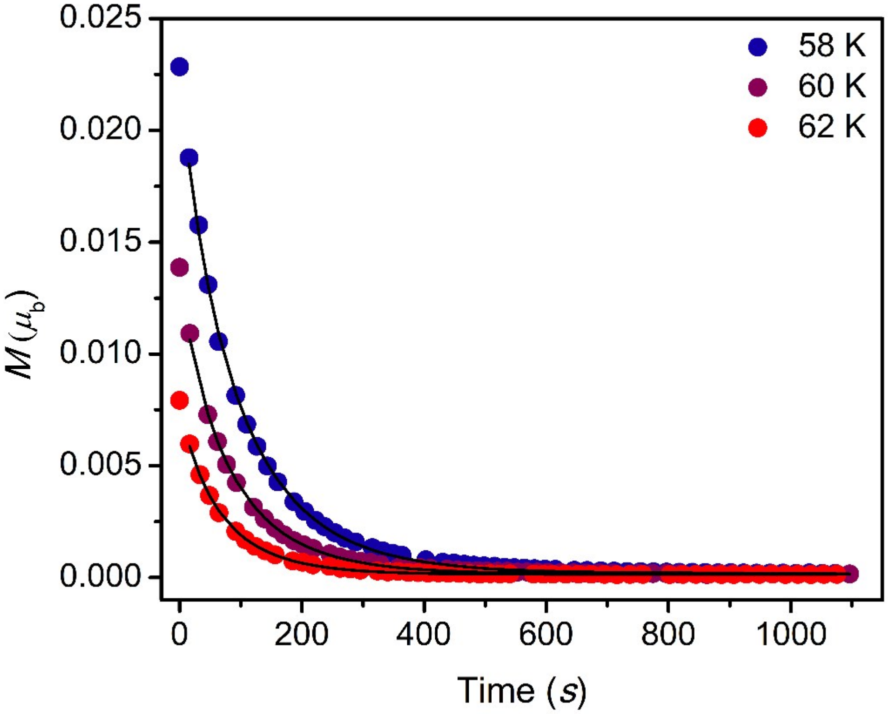

Figure S68. Dc magnetic relaxation data for **4** collected at 58, 60, and 62 K. Black lines represent the fits to the data using stretched exponential functions, which were used to extract τ.

Analysis of Magnetic Relaxation Dynamics. Magnetic relaxation times extracted from ac susceptibility measurements of **1-4** showed an exponential dependence on temperature, indicative of an Orbach relaxation mechanism. Data were fit to the equation:

$$\tau^{-1} = \tau_0^{-1} e^{-U_{eff}/k_b T}$$

where τ is the magnetic relaxation time, τ_0 is the attempt time, U_{eff} is the thermal barrier to magnetization reversal, $k_b = 0.695\ \text{cm}^{-1}\text{K}^{-1}$, and T is temperature.

The full range of magnetic relaxation times extracted from ac susceptibility and dc magnetic relaxation experiments showed a more complex temperature dependence, indicative of multiple magnetic relaxation pathways. Plots of the log of magnetic relaxation time versus $1/T$ showed an exponential dependence at intermediate temperatures and flattened at low T, suggesting the presence of Raman relaxation and/or quantum tunneling of the magnetization. Accordingly, the data for **1-4** were fit to the equation:

$$\tau^{-1} = \tau_0^{-1} e^{-U_{eff}/k_b T} + \tau_{tunnel}^{-1} + CT^n$$

where τ_{tunnel} is the relaxation time for quantum tunneling of the magnetization and C and n are free variables that describe Raman relaxation. To avoid over-parameterization, τ_0 and U_{eff} were fixed to the values extracted from fits to only the ac magnetic susceptibility measurements, while τ_{tunnel} was set equal to the 2 K magnetic relaxation time. All three relaxation processes were necessary to obtain fits that satisfactorily reproduced the data.

Table S7. Parameters used to fit the Arrhenius plots of **1-4**.

	1	**2**	**3**	**4**
U_{eff} (cm^{-1})	1285	1468	1380	1334
τ_0 (s)	3.39 x 10^{-12}	4.01 x 10^{-12}	7.79 x 10^{-12}	1.18 x 10^{-11}
τ_{tunnel} (s)	439	2452	447	1187
C	2.27 x 10^{-5}	1.57 x 10^{-6}	3.36 x 10^{-8}	8.04 x 10^{-7}
n	2.00	2.07	3.02	2.31

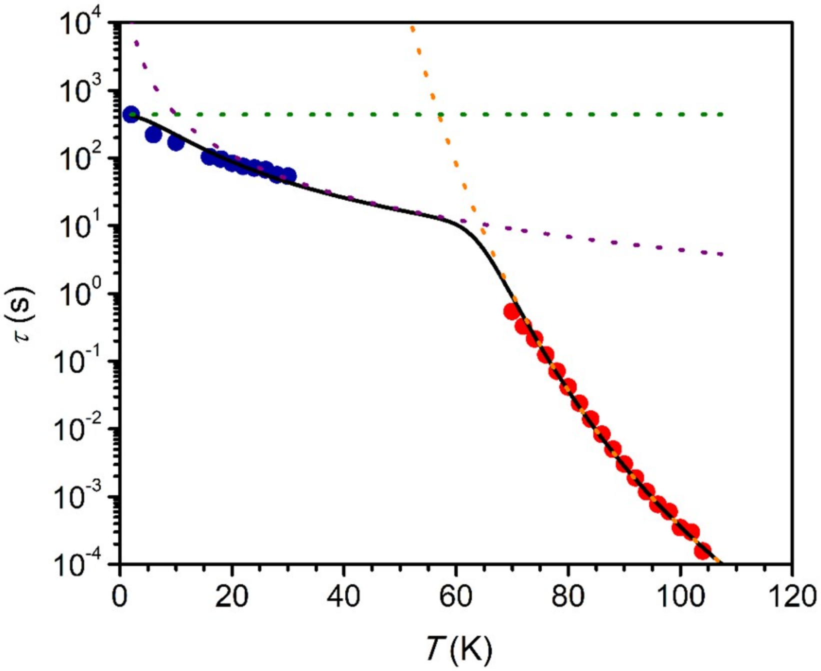

Figure S69. Plot of magnetic relaxation time versus temperature for **1** (dc relaxation, blue circles; ac susceptibility, red circles). Green, purple, and orange lines represent fits to quantum tunneling, Raman, and Orbach relaxation processes, respectively. Black line represents the total fit to the data.

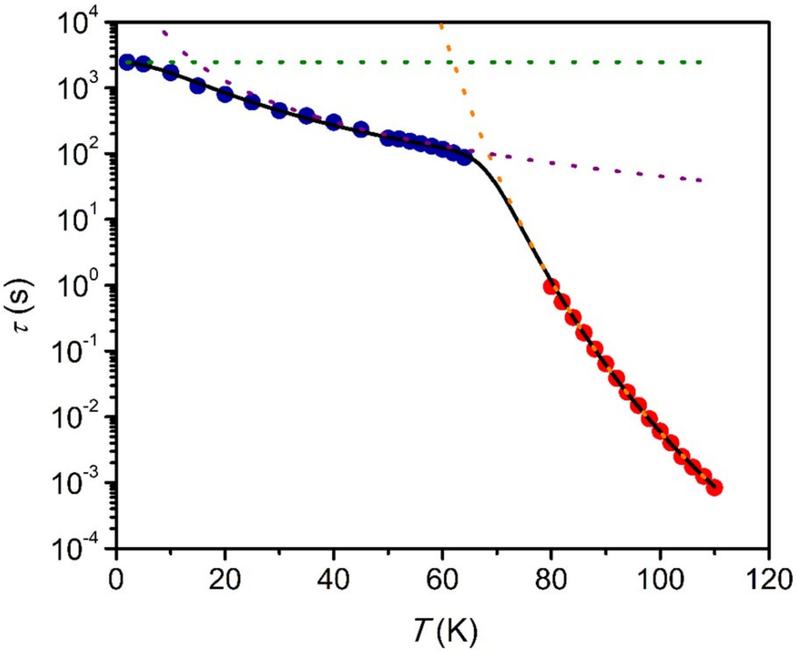

Figure S70. Plot of magnetic relaxation time versus temperature for **2** (dc relaxation, blue circles; ac susceptibility, red circles). Green, purple, and orange lines represent fits to quantum tunneling, Raman, and Orbach relaxation processes, respectively. Black line represents the total fit to the data.

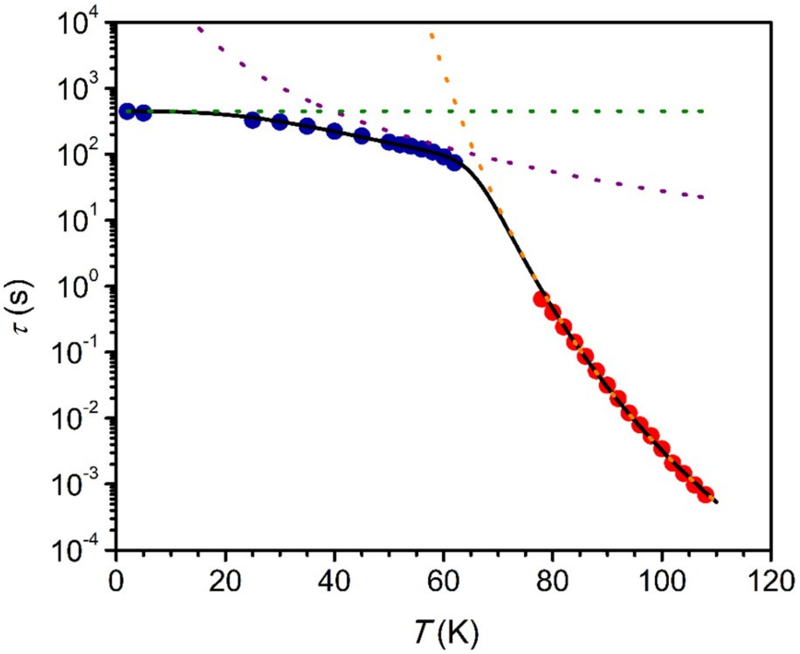

Figure S71. Plot of magnetic relaxation time versus temperature for **3** (dc relaxation, blue circles; ac susceptibility, red circles). Green, purple, and orange lines represent fits to quantum tunneling, Raman, and Orbach relaxation processes, respectively. Black line represents the total fit to the data.

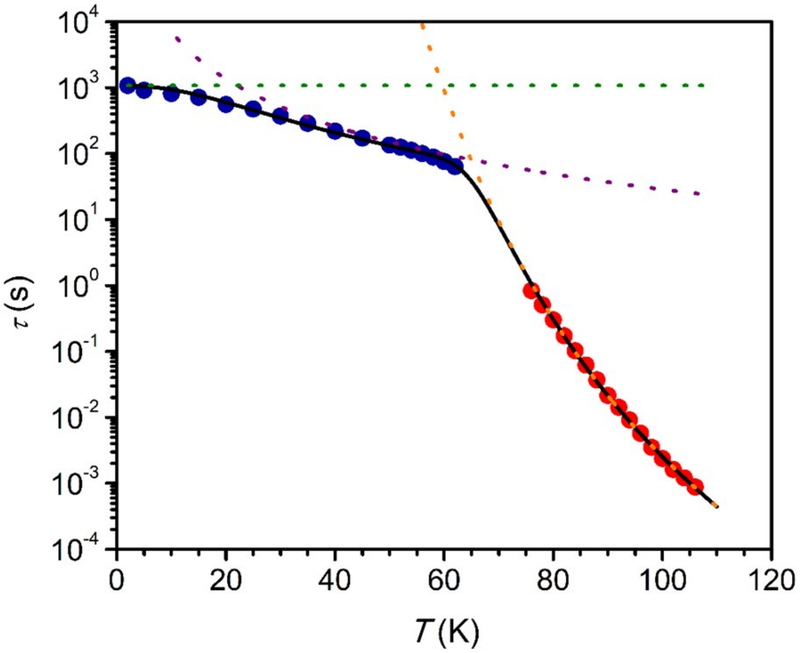

Figure S72. Plot of magnetic relaxation time versus temperature for **4** (dc relaxation, blue circles; ac susceptibility, red circles). Green, purple, and orange lines represent fits to quantum tunneling, Raman, and Orbach relaxation processes, respectively. Black line represents the total fit to the data.

Magnetic Dilution Measurements. Magnetically dilute sample of **1-4** were prepared by co-crystallization of the compound with the Y^{3+} congener $[Y(Cp^{iPr4R})_2][B(C_6F_5)_4]$ (R= H (**Y1**), Me (**Y2**), Et (**Y3**), *i*Pr (**Y4**)) in roughly a 9:1 Y:Dy molar ratio. The % Dy in this sample was determined by fitting the dc susceptibility curve of the dilution above 60 K to that measured for the undiluted sample. Using this method, the diluted samples **1-4@Y** were determined to contain, 10.9, 8.8 11.5, and 8.7% Dy, respectively. Dc susceptibility, dc magnetic relaxation, and magnetic hysteresis measurements were conducted as described in the manuscript or earlier in the Supplementary Information.

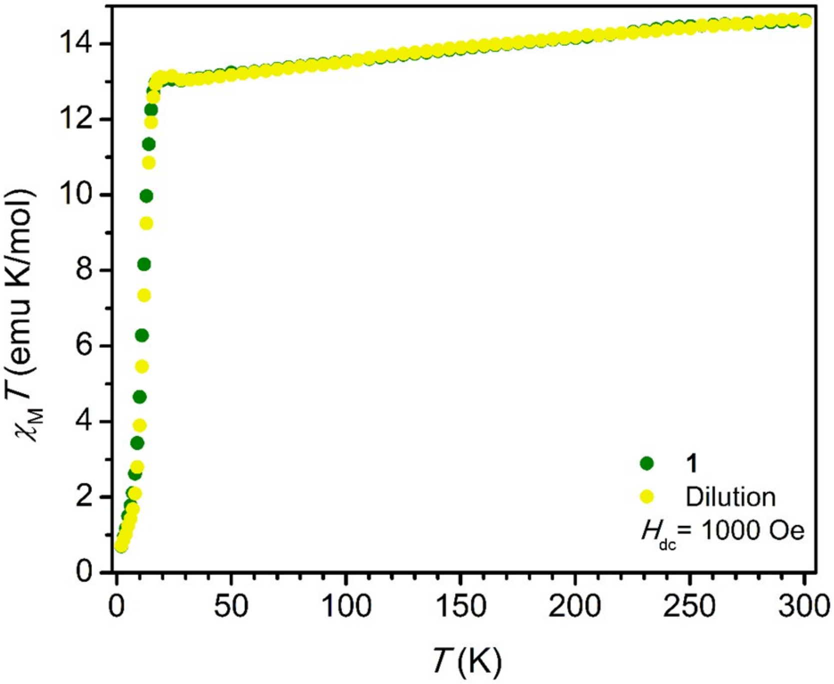

Figure S73. Zero-field cooled dc magnetic susceptibility measurements of **1** and the dilution **1@Y** under an applied field of 1000 Oe. Fitting the high temperature region (above 60 K) of these two plots yielded 10.9% Dy as the composition of the dilution.

Table S8. Parameters used to fit dc magnetic relaxation data for the dilution **1@Y** and magnetic relaxation times extracted from these fits.

T (K)	M_0 (μ_b)	M_1 (μ_b)	n	τ (s)[a]
2	3.26016	0.84486*	0.755	1782.653
22	0.08344	0.00103	0.864	89.616
24	0.04897	0.00066	0.867	75.471
26	0.02306	0.00062	0.886	67.707
28	0.01203	0.00051	0.827	62.363
30	0.00634	0.00040	0.934	58.116

*M_1 values obtained by treating M_1 as a free variable

[a] Values for τ are likely only accurate to three significant figures. The full value extracted from the fit is reported for reproducibility.

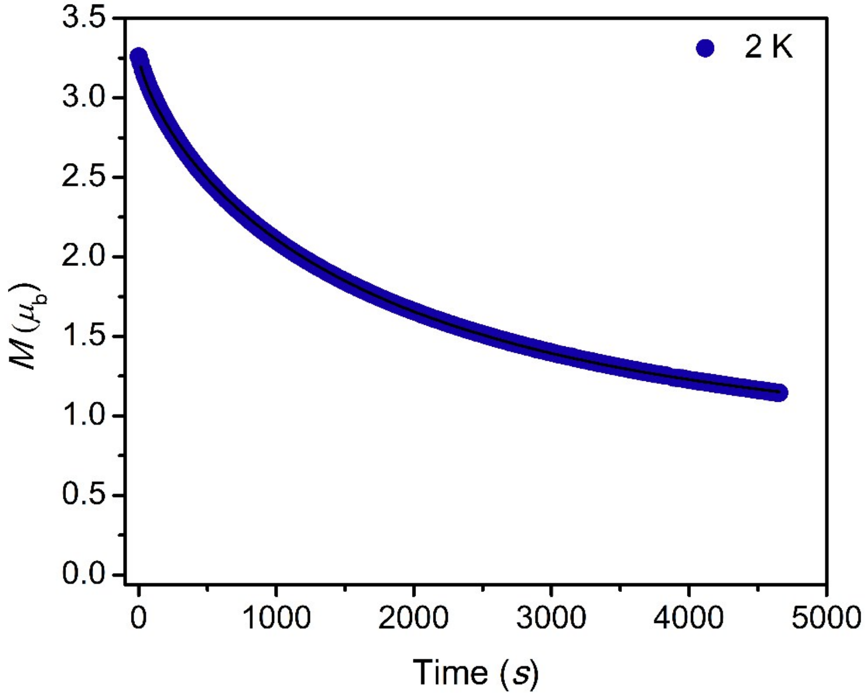

Figure S74. Dc magnetic relaxation data for the dilution **1@Y** collected at 2 K. Black lines represent the fits to the data using stretched exponential functions, which were used to extract τ.

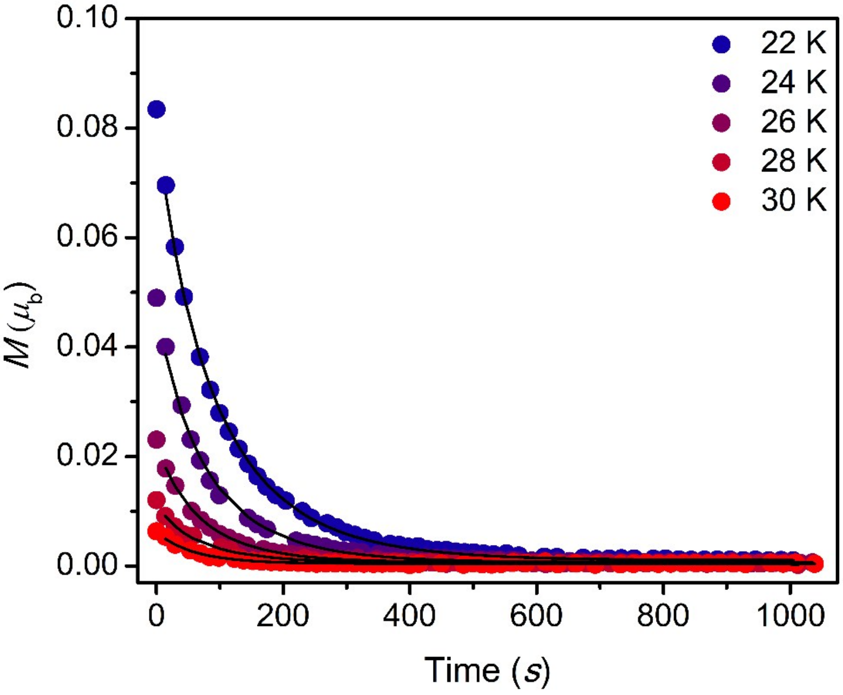

Figure S75. Dc magnetic relaxation data for the dilution **1@Y** collected at 22, 24, 26, 28 and 30 K. Black lines represent the fits to the data using stretched exponential functions, which were used to extract τ.

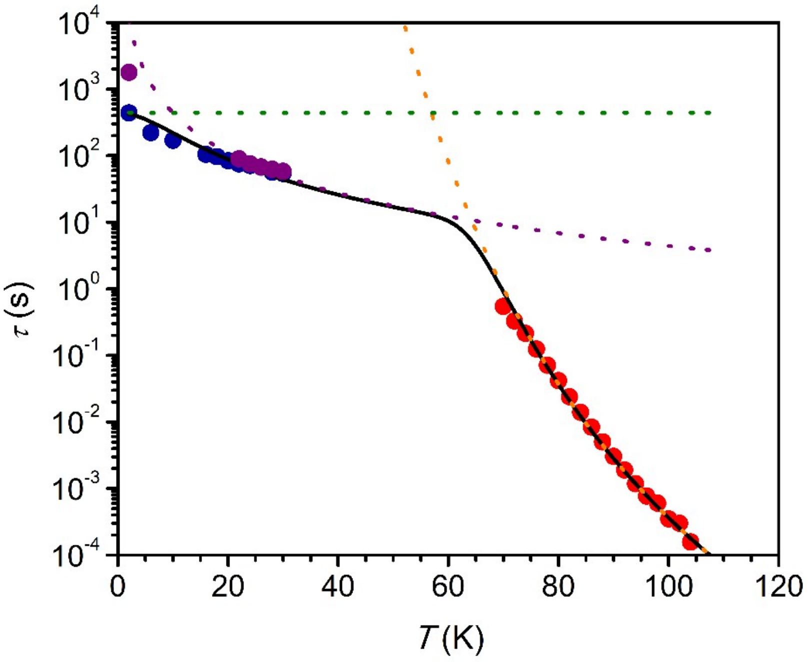

Figure S76. Plot of magnetic relaxation time versus temperature for **1** (dc relaxation, blue circles; ac susceptibility, red circles). Green, purple, and orange lines represent fits to quantum tunneling, Raman, and Orbach relaxation processes, respectively. Black line represents the total fit to the data. Purple circles represent relaxation times for the dilution **1@Y** extracted from dc relaxation measurements.

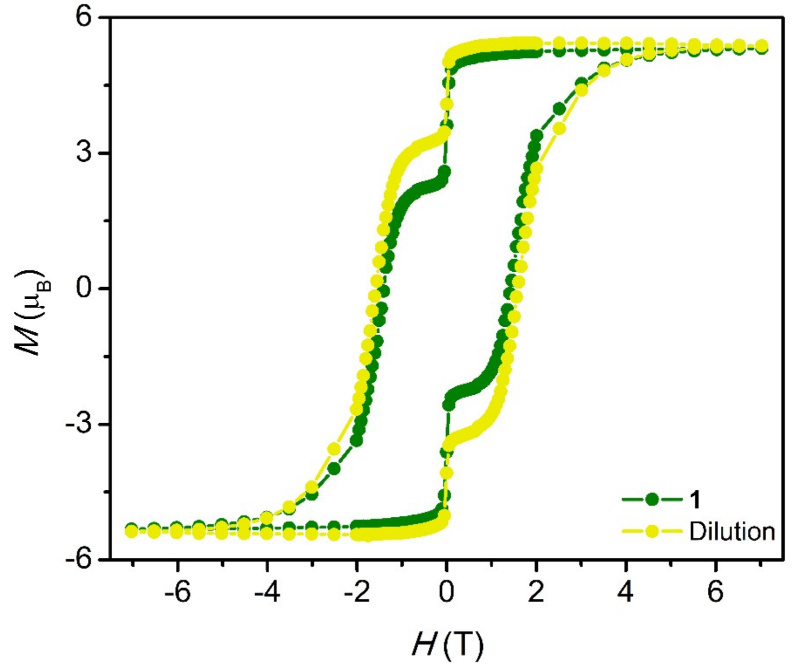

Figure S77. Magnetic hysteresis measurements of **1** and the dilution **1@Y** at 2 K at a sweep rate of 3.1(4) mT/s for $H < 2$ T and 13.2(2) mT/s $H > 2$ T.

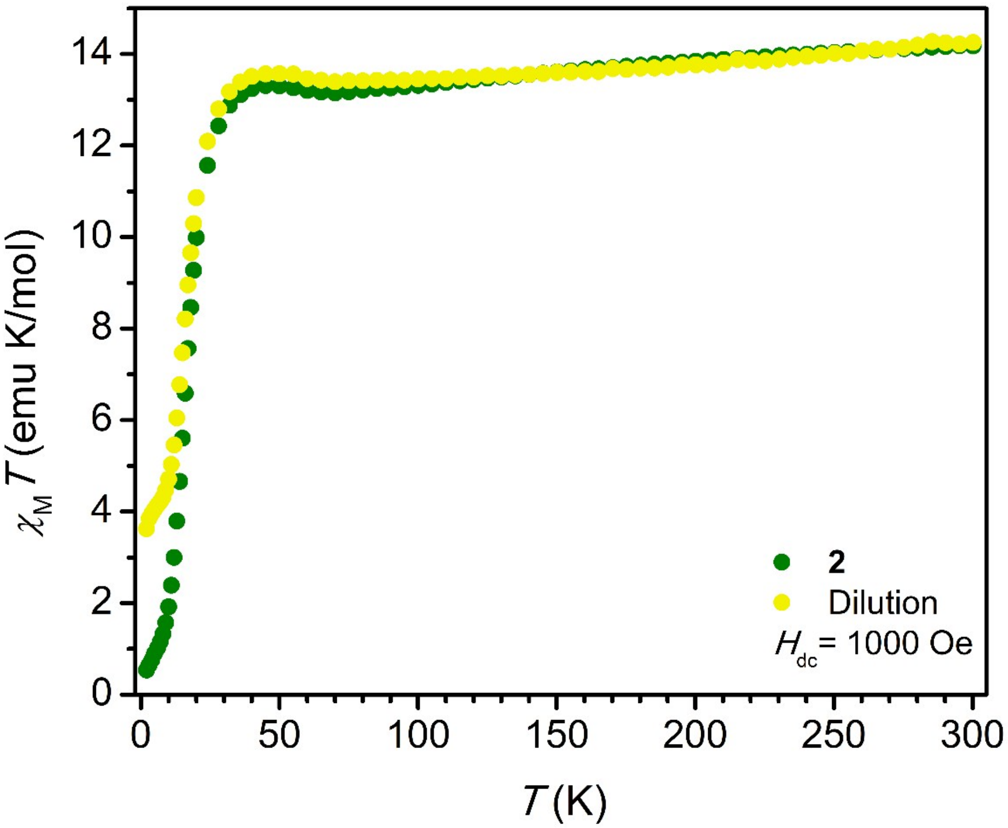

Figure S78. Zero-field cooled dc magnetic susceptibility measurements of **2** and the dilution **2@Y** under an applied field of 1000 Oe. Fitting the high temperature region (above 60 K) of these two plots yielded 8.8% Dy as the composition of the dilution.

Table S9. Parameters used to fit dc magnetic relaxation data for the dilution **2@Y** and magnetic relaxation times extracted from these fits.

T (K)	M_0 (μ_b)	M_1 (μ_b)	n	τ (s)[a]
2	3.16566	0.15983*	0.583	11200.173
56	0.07237	0.00134	0.943	146.308
58	0.05892	0.00112	0.958	126.621
60	0.04713	0.00030	0.906	115.470
62	0.03457	0.00044	0.953	105.074
64	0.02213	0.00037	1.000	93.667

*M_1 values obtained by treating M_1 as a free variable

[a] Values for τ are likely only accurate to three significant figures. The full value extracted from the fit is reported for reproducibility.

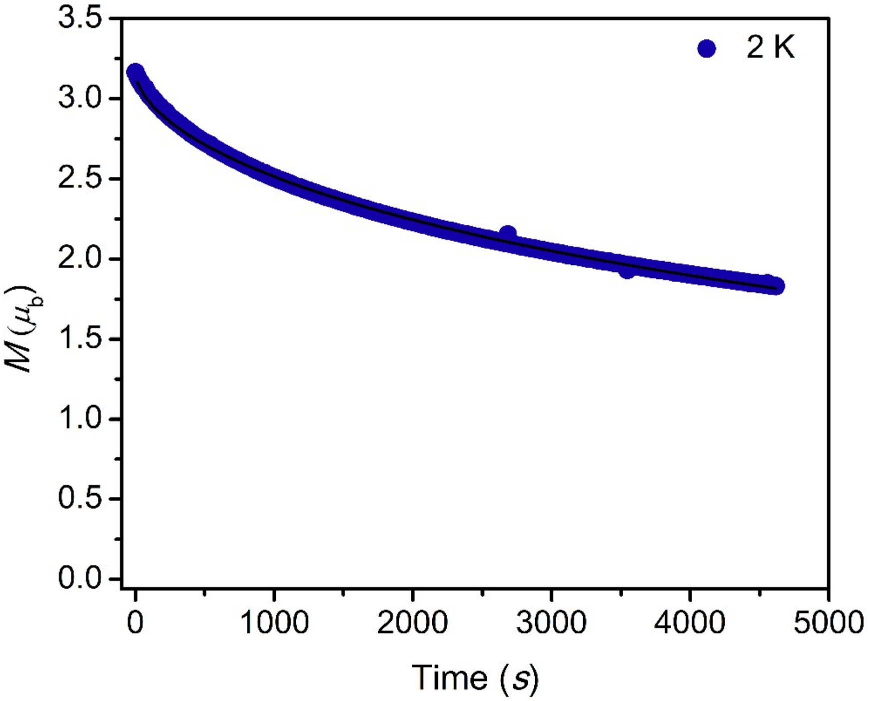

Figure S79. Dc magnetic relaxation data for the dilution **2@Y** collected at 2 K. Black lines represent the fits to the data using stretched exponential functions, which were used to extract τ.

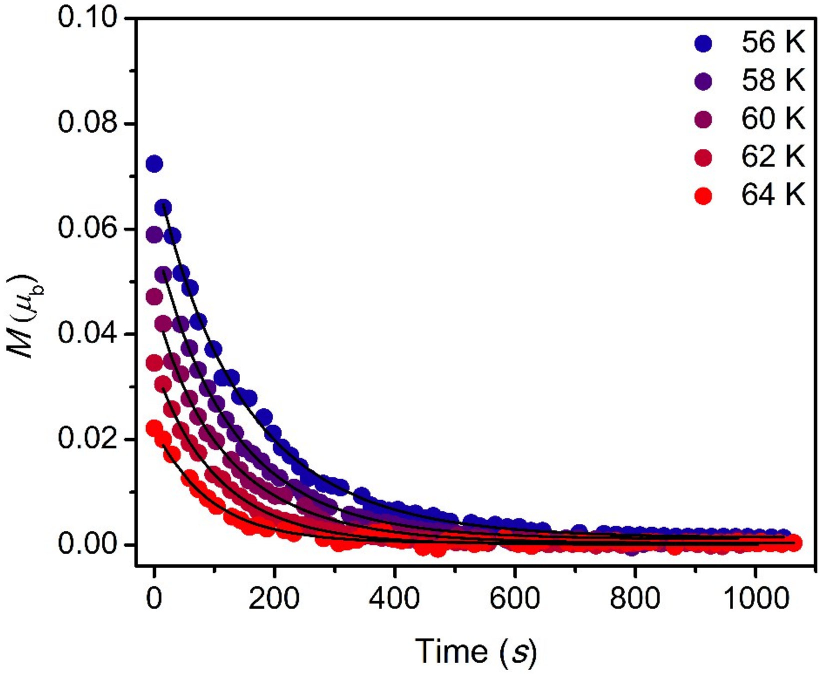

Figure S80. Dc magnetic relaxation data for the dilution **2@Y** collected at 56, 58, 60, 62 and 64 K. Black lines represent the fits to the data using stretched exponential functions, which were used to extract τ.

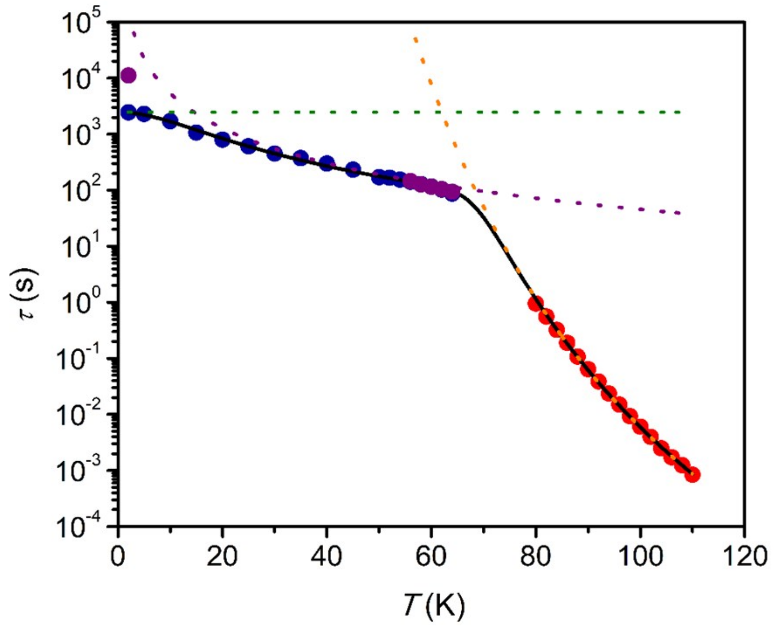

Figure S81. Plot of magnetic relaxation time versus temperature for **2** (dc relaxation, blue circles; ac susceptibility, red circles). Green, purple, and orange lines represent fits to quantum tunneling, Raman, and Orbach relaxation processes, respectively. Black line represents the total fit to the data. Purple circles represent relaxation times for the dilution **2@Y** extracted from dc relaxation measurements.

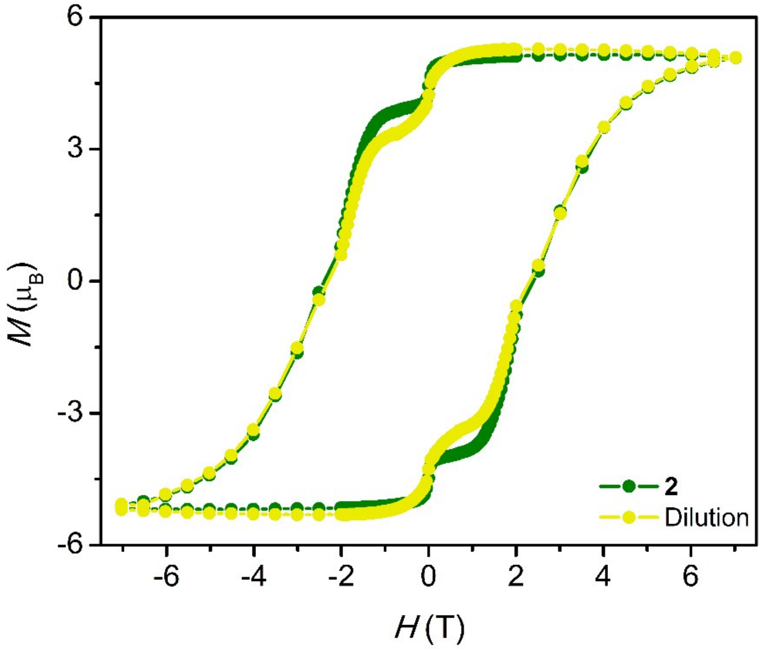

Figure S82. Magnetic hysteresis measurements of **2** and the dilution **2@Y** at 2 K at a sweep rate of 3.1(4) mT/s for $H < 2$ T and 13.2(2) mT/s $H > 2$ T.

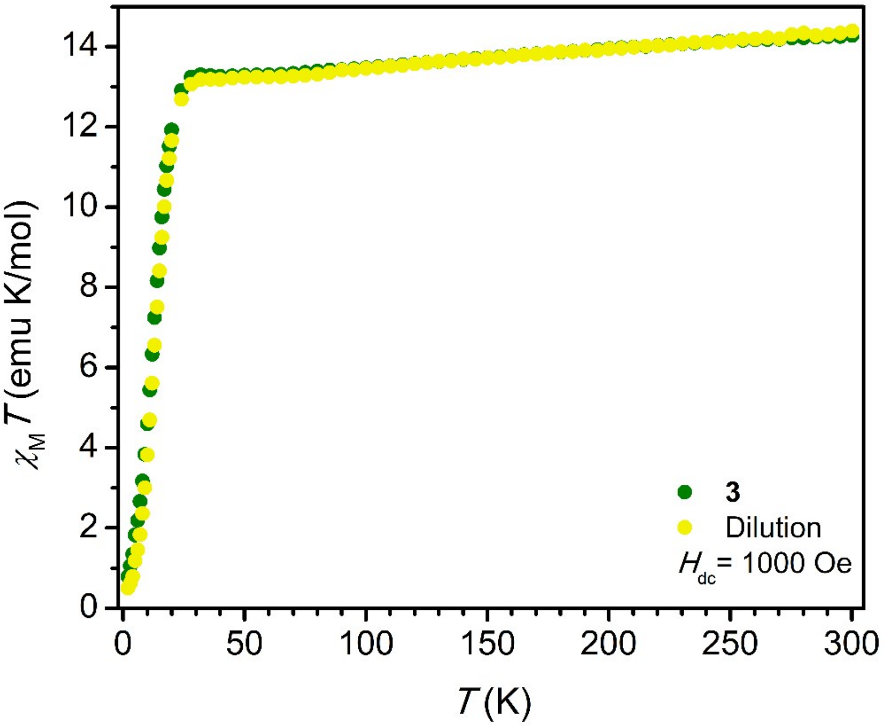

Figure S83. Zero-field cooled dc magnetic susceptibility measurements of **3** and the dilution **3@Y** under an applied field of 1000 Oe. Fitting the high temperature region (above 60 K) of these two plots yielded 11.5% Dy as the composition of the dilution.

Table S10. Parameters used to fit dc magnetic relaxation data for the dilution **3@Y** and magnetic relaxation times extracted from these fits.

T (K)	**M_0 (μ_b)**	**M_1 (μ_b)**	**n**	**τ (s)[a]**
2	3.213927	1.06550*	0.726	1125.215
56	0.02068	0.00038	0.926	135.265
58	0.01548	0.00027	0.928	117.742
60	0.00927	0.00028	1.000	107.402
62	0.00496	0.00021	0.910	75.897
64	0.00265	0.00020	0.998	62.907

*M_1 values obtained by treating M_1 as a free variable

[a] Values for τ are likely only accurate to three significant figures. The full value extracted from the fit is reported for reproducibility.

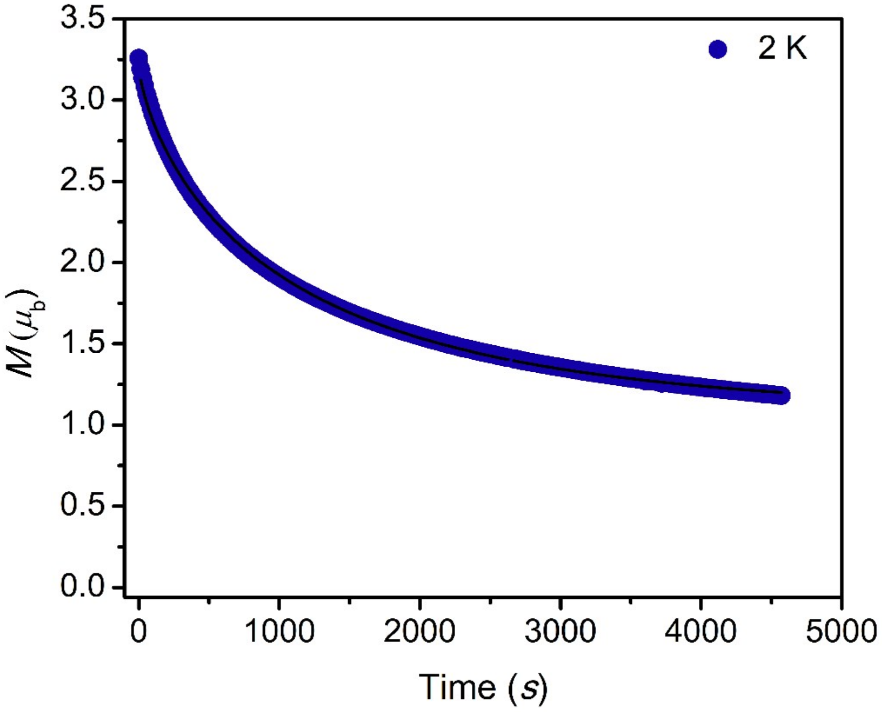

Figure S84. Dc magnetic relaxation data for the dilution **3@Y** collected at 2 K. Black lines represent the fits to the data using stretched exponential functions, which were used to extract τ.

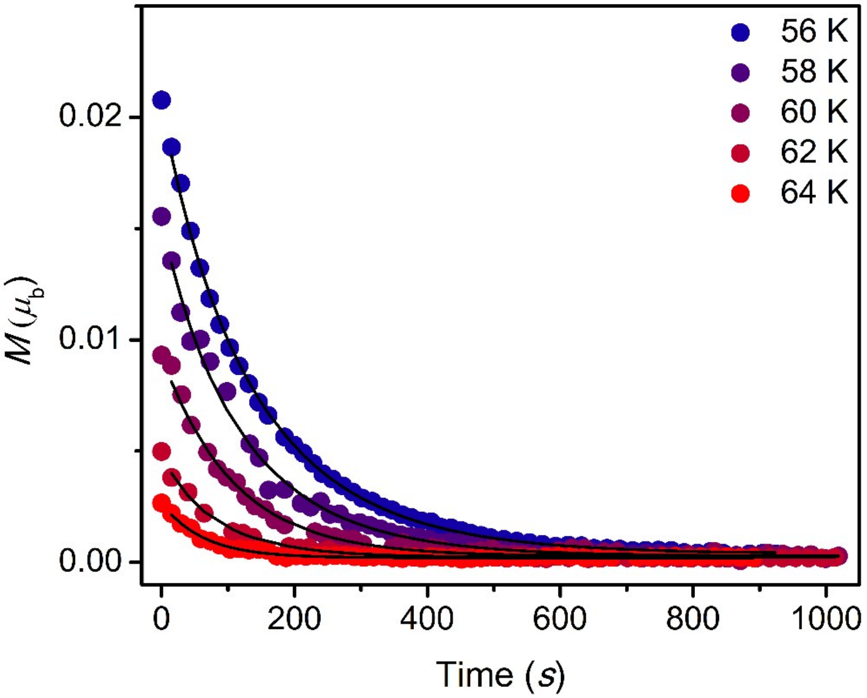

Figure S85. Dc magnetic relaxation data for the dilution **3@Y** collected at 56, 58, 60, 62 and 64 K. Black lines represent the fits to the data using stretched exponential functions, which were used to extract τ.

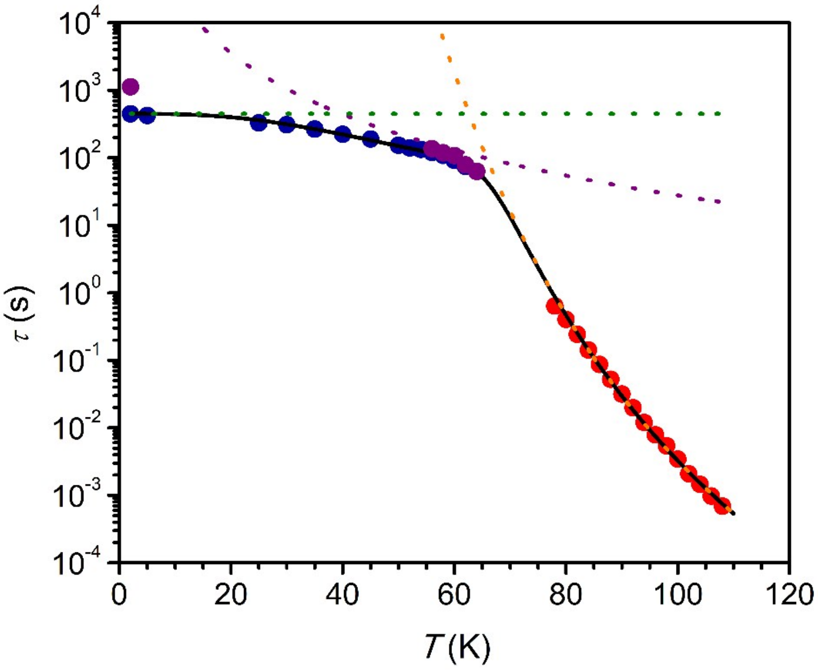

Figure S86. Plot of magnetic relaxation time versus temperature for **3** (dc relaxation, blue circles; ac susceptibility, red circles). Green, purple, and orange lines represent fits to quantum tunneling, Raman, and Orbach relaxation processes, respectively. Black line represents the total fit to the data. Purple circles represent relaxation times for the dilution **3@Y** extracted from dc relaxation measurements.

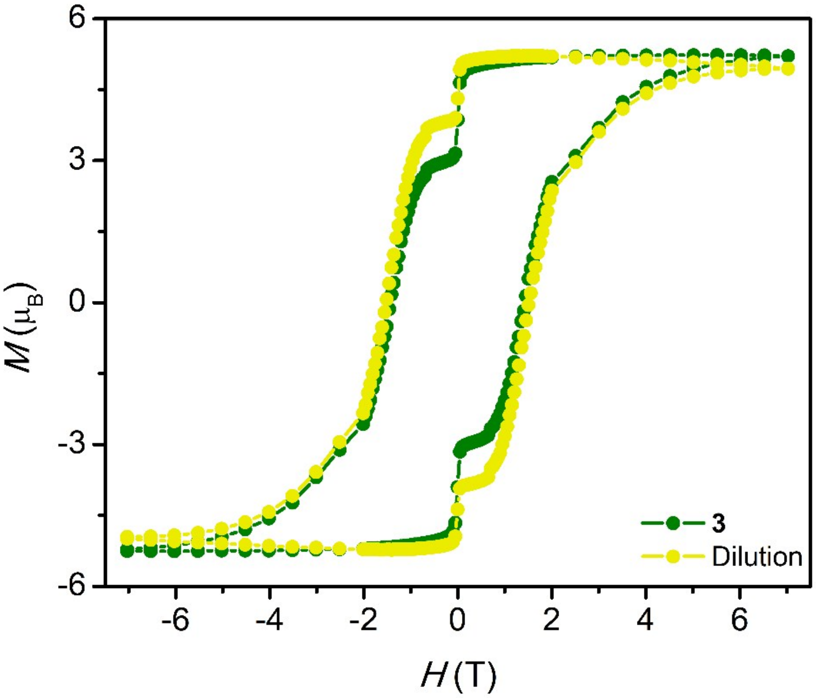

Figure S87. Magnetic hysteresis measurements of **3** and the dilution **3@Y** at 2 K at a sweep rate of 3.1(4) mT/s for *H* < 2 T and 13.2(2) mT/s *H* > 2 T.

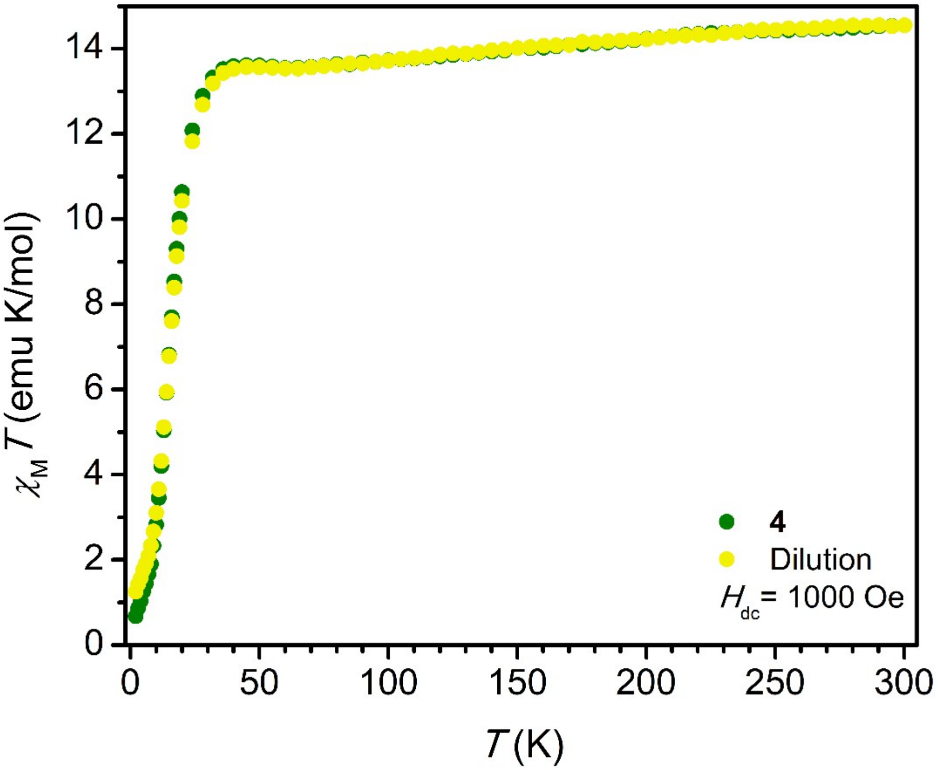

Figure S88. Zero-field cooled dc magnetic susceptibility measurements of **4** and the dilution **4@Y** under an applied field of 1000 Oe. Fitting the high temperature region (above 60 K) of these two plots yielded 8.7% Dy as the composition of the dilution.

Table S11. Parameters used to fit dc magnetic relaxation data for the dilution **4@Y** and magnetic relaxation times extracted from these fits.

T (K)	**M_0 (μ_b)**	**M_1 (μ_b)**	**n**	**τ (s)[a]**
2	3.70041	1.27894*	0.720	1956.098
54	0.04907	0.00084	0.913	112.065
56	0.03621	0.00053	0.894	100.429
58	0.02640	0.00056	0.921	89.353
60	0.01566	0.00050	0.879	72.127
62	0.00865	0.00041	0.737	60.019

*M_1 values obtained by treating M_1 as a free variable

[a] Values for τ are likely only accurate to three significant figures. The full value extracted from the fit is reported for reproducibility.

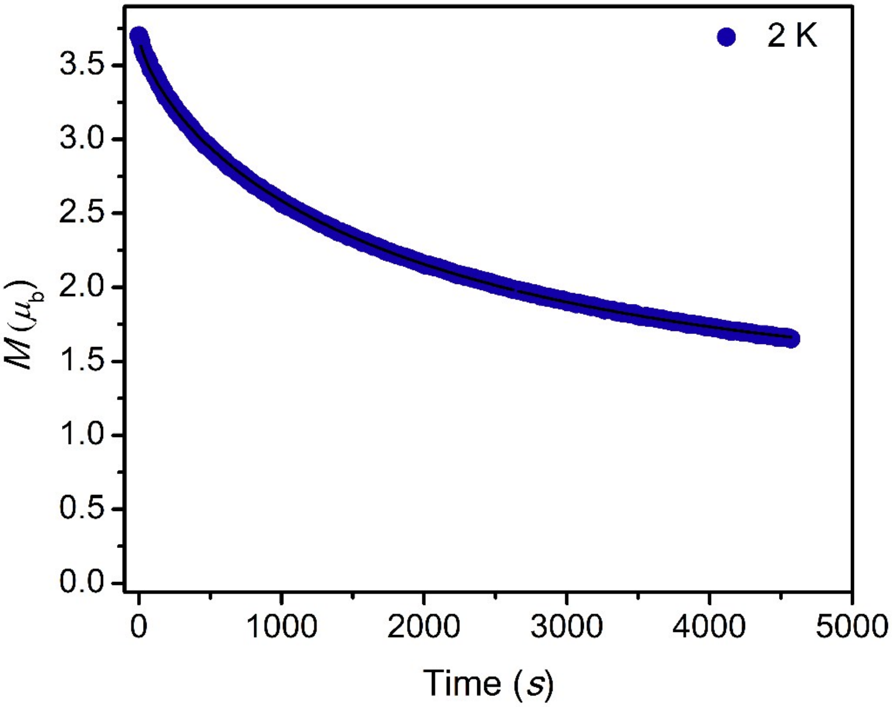

Figure S89. Dc magnetic relaxation data for the dilution **4@Y** collected at 2 K. Black lines represent the fits to the data using stretched exponential functions, which were used to extract τ.

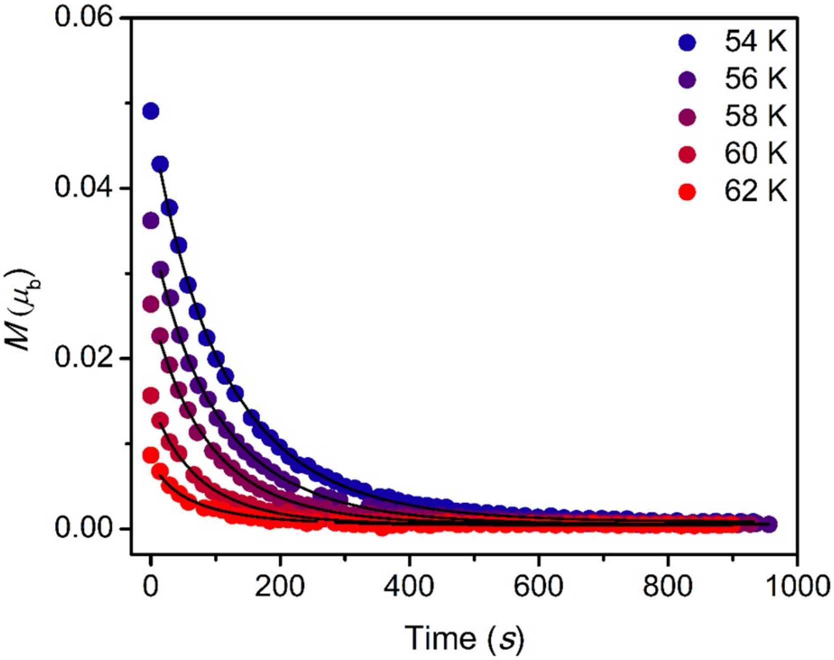

Figure S90. Dc magnetic relaxation data for the dilution **4@Y** collected at 54, 56, 58, 60 and 62 K. Black lines represent the fits to the data using stretched exponential functions, which were used to extract τ.

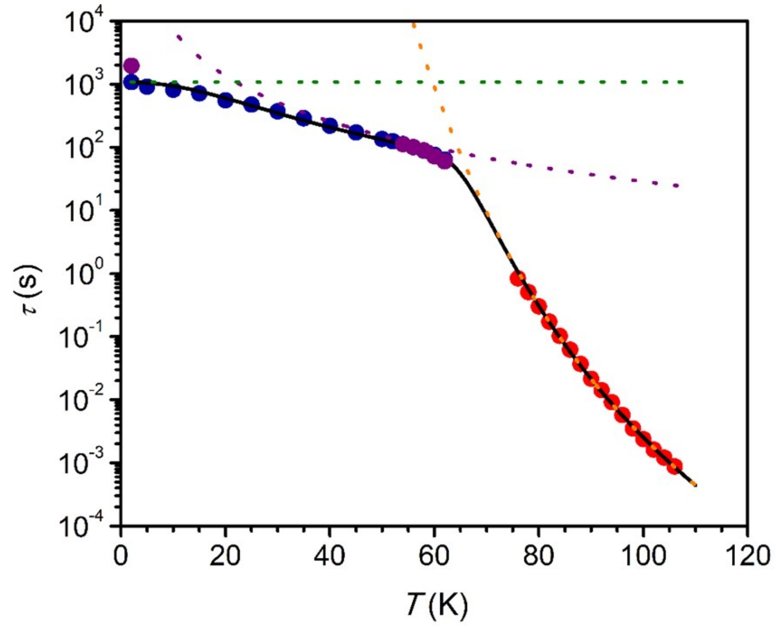

Figure S91. Plot of magnetic relaxation time versus temperature for **4** (dc relaxation, blue circles; ac susceptibility, red circles). Green, purple, and orange lines represent fits to quantum tunneling, Raman, and Orbach relaxation processes, respectively. Black line represents the total fit to the data. Purple circles represent relaxation times for the dilution **4@Y** extracted from dc relaxation measurements.

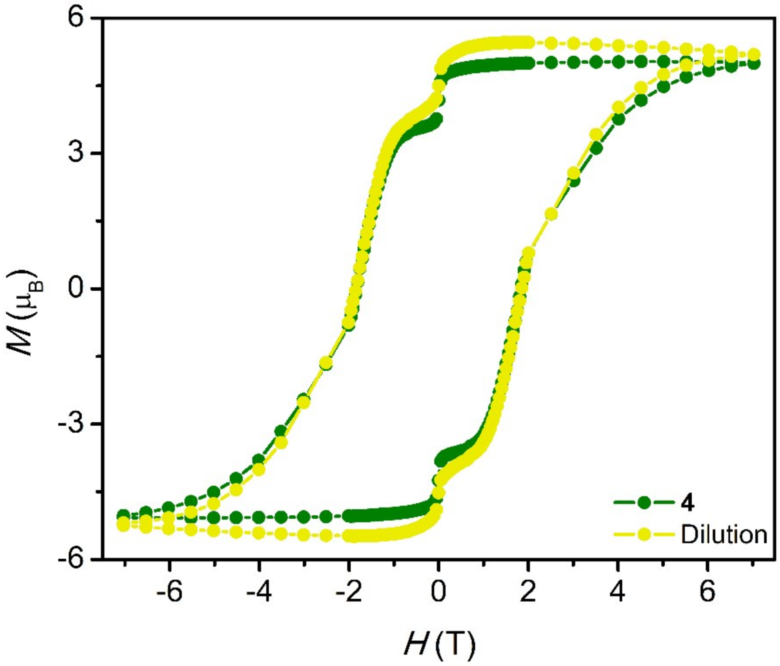

Figure S92. Magnetic hysteresis measurements of **4** and the dilution **4@Y** at 2 K at a sweep rate of 3.1(4) mT/s for $H < 2$ T and 13.2(2) mT/s $H > 2$ T.

References

(1) SAINT and APEX 2 Software for CCD Diffractometers, Bruker Analytical X-ray Systems Inc., Madison, WI, USA, 2014.
(2) Sheldrick, G. M. SADABS, Version 2.03; Bruker Analytical X-ray Systems, Inc: Madison, WI, 2000.
(3) APEX3, v. 2009; Bruker Analytical X-Ray Systems, Inc: Madison, WI, 2009.
(4) Sheldrick, G. M. SHELXT, University of Göttingen, Germany, 2015
(5) Sheldrick, G. M. SHELXL, University of Göttingen, Germany, 2015
(6) Dolomanov, O. V.; Bourhis, L. J.; Gildea, R. J.; Howard, J. A. K.; Puschmann, H. *J. Appl. Cryst*. **2009**, *42*, 339–341.